Heterogeneous Reactivity of Dinitrogen Pentoxide with Sodium Chloride and Nitrate Containing Solutions

By Thomas Derrah

A dissertation submitted in partial fulfillment of the requirements for the degree of

Doctor of Philosophy

(Chemistry)

At the

University of Wisconsin-Madison

2024

Date of final oral examination: August 23rd, 2024

Final Oral Committee

Timothy Bertram, Professor, Chemistry

Gilbert Nathanson, Professor, Chemistry

Susanna Widicus Weaver, Professor, Chemistry

John Berry, Professor, Chemistry

Abstract

Dinitrogen pentoxide (N_2O_5) is a nocturnal reservoir for NO_x ($NO_x \equiv NO$ and NO_2). In the troposphere, the dominant loss process for N_2O_5 is the heterogeneous reaction with aqueous aerosol. This sink for NO_x results in decreased ozone (O_3) and hydroxyl radical concentrations in the atmosphere, leading to longer chemical lifetimes for organic species such as methane. Reaction of N_2O_5 to aqueous aerosol forms nitric acid (HNO_3) through a hydrolysis pathway, but reaction with chloride-containing particles produces nitryl chloride ($ClNO_2$).

The mechanisms by which N_2O_5 reacts is currently under scrutiny. A previous mechanism involving dissociation to form a nitronium cation (NO_2^+) conflicts with recent molecular dynamics simulations which find N_2O_5 undergoes a charge fluctuation rather than fully dissociating. Mechanisms with this new species would need to be interrogated to determine if agree with experimentally derived factors, such as the effect of ions on N_2O_5 uptake.

In chapter 2, I provide a description of the instrument setup used to perform experiments on N_2O_5 reactivity. This includes the method for N_2O_5 synthesis, the design of a dual channel flow reactor, and chemical ionization mass spectrometer used for detection of N_2O_5 and $ClNO_2$. Additional experiments important for understanding what factors influence our experiments are included.

In chapter 3, I present my findings on the temperature dependence of the competition between the hydrolysis reaction and the reaction of N_2O_5 with aqueous Cl^-. We found a 5% increase in the product yield of $ClNO_2$ as temperature decreased. Through an Arrhenius analysis, we determined the activation energy difference between hydrolysis and chlorination was only -

3.0 ± 1.5 kJ/mol. We calculate a rate constant ratio, k_{Cl^-}/k_{D2O}, = 1150 ± 90 at 298 K. The high favorability for chlorination appears to be driven by entropic and dynamic factors.

In chapter 4, I investigate the nitrate effect of N_2O_5 using isotopically labeled $^{15}NO_3^-$. Along with NaCl in solutions, we measure the production of isotopically labeled $^{14,15}N_2O_5$, $^{15,15}N_2O_5$, and $Cl^{15}NO_2$, indicating a chemical exchange between N_2O_5 and $^{15}NO_3^-$ occurred. We determine the rate constant ratio, k_{Cl^-}/k_{NO3^-} = 3.6 – 6.2 for concentrations of $^{15}NO_3^-$ between 3.7 and 0.47 M. We attempt to bring together the known factors on the reactivity of N_2O_5 and examinate the various mechanisms for reaction to understand this complicated molecule.

Table of Contents

List of Figures

List of Tables

Acknowledgements

While a Ph.D. will only have my name on the document, there are many people who helped me along this journey and are responsible for me finishing this degree.

I would like to thank Tim Bertram and Gil Nathanson for their mentorship, teaching, and patience throughout my Ph.D. I learned many things from them, not just known facts about certain reactions, but mostly how to approach problems and understand results. The other members of the Bertram and Nathanson Research groups have been a tremendous part of my journey. Past members (Joe Gord, Steven Kregel, Xiao-Fei Gao, Xian Yuan Zhao, Gordon Novak, Michael Vermeuel, Christopher Jernigan, Rachel Bergin, Delaney Kilgour, Carson McFarland) and current ones (David Hood, Martina Rogers, Subi Thakali, Kevin Wokosin, Elizabeth Kray, Rebecca Fenselau, and Audrey Lyp) have all been of great help, providing a guidance on certain tasks, effective voices to bounce ideas off of, and entertaining banter as a break from work

I would especially like to thank Steven Kregel for all the guidance and teaching he provided over several years. When I started my Ph.D., I was still taking my graduate classes when the Covid pandemic started in March 2020 and we were not allowed into the chemistry building. Missing out on my first summer of laboratory research and not being around the rest of my group members for the early months could have been a hamper on my development as a researcher. But working on a project with Steve in the lab greatly helped me learn the ropes. Even though he had joined the research group after I had, Steve was an excellent mentor in helping me understand how things research was actually performed.

I'd like to acknowledge the members of the Center for Aerosol Research on Chemistry of the Environment (CAICE), led by Kimberly Prather. Being a member of CAICE for most of my

Ph.D. had a great impact on my research. Chris Lee and Jeanette Starpine did excellent jobs coordinating events for us. The members of the RT2a subgroup in CAICE, focused on interfacial reactions, were great people to share my results and talk with. Mark Johnson, David Limmer, Benny Gerber, Heather Allen, Andy Goetz, Natalia Karimova, Santino Stropoli, and Seokjin Moon all helped to make the group a great collaborative environment.

My partner, Michał, has been with me for every step of this journey and always helped keep me going through the degree, constantly encouraging me. Accomplishing this thesis would not have been the same without him. All of my family has provided a lot of support over the years. Bill, John, Val, Pete, and Gwen, and my parents, Alicia and William, have listened to me drone on about my work and always cheered me on. And just as important, my hounds: Clover, Stella, and Ivy. While I only could see them when I visited my family, they were still a great source of comfort.

Chapter 1. Introduction

1.1 NO_x Cycling and N_2O_5 Formation

Nitrogen oxide (NO) and nitrogen dioxide (NO_2) play a vital role in the oxidative capacity of the atmosphere. NO_X is defined as NO + NO_2, due to the cycling between the two species. These species are vital precursors for ozone (O_3) generation in the troposphere. In the stratosphere, ultraviolet (UV) light (<242 nm) photolyzes molecular oxygen (O_2) to form oxygen atoms (O), which can go on to form O_3[1–3]. This short wavelength UV light does not reach the troposphere due to absorption by O_3 and O_2 in the stratosphere.[3] Instead, the primary source of O_3 in the troposphere is from photolysis (<430 nm) of NO_2 to form O, and O reacting with O_2.[1,3,4] (R1.1 - 1.5)

$$NO + O_3 \rightarrow NO_2 + O_2 \quad \text{R1.1}$$

$$NO_2 + h\nu \rightarrow NO + O \quad \text{R1.2}$$

$$O + O_2 \rightarrow O_3 \quad \text{R1.3}$$

$$O_3 \rightarrow O_2 + O \quad \text{R1.4}$$

$$NO + HO_2 \rightarrow NO_2 + HO \quad \text{R1.5}$$

Global concentrations of O_3 are generally 30-50 ppb, but local variations in the NO_x and volatile organic compound concentrations have significant impacts on O_3 formation.[4] Lamsal et al. 2008 found the mean NO_2 concentrations across the United States.[5] Urban NO_2 concentrations display a diurnal profile, with the annual mean ranging from 10 to 20 ppb; rural areas had less NO_2 present, with the annual mean varying from 5 to 8 ppb. NO_x enters the atmosphere primarily from anthropogenic sources, such as fossil fuel and biomass burning, but some biogenic sources

also exist, including naturally-caused biomass burning and lightning strikes.[6] Delmas et al determined the global inventory of NO_x species to be 38 Tg N / yr, of which about 75% comes from anthropogenic biomass and fossil fuel burning.[6] Further oxidation of NO_x can form the nitrate radical, NO_3.

$$NO_2 + O_3 \rightarrow NO_3 + O_2 \qquad \text{R1.6}$$

$$NO_3 + h\nu \rightarrow NO_2 + O \qquad \text{R1.7}$$

$$NO_3 + h\nu \rightarrow NO + O_2 \qquad \text{R1.8}$$

The photolysis of NO_3 occurs between 420 and 640 nm. Thus during daytime, NO_3 is readily destroyed to reform NO_x.[7] At night, photolysis stops and NO_3 builds up. Daytime concentrations are about 0, while night time maximums can reach in the hundreds of pptv.[8,9] Vertical profiles show the highest NO_3 concentrations are found at less than 5 km above the earth's surface.[10] With the lack of photolysis loss at night, the increase of NO_2 and NO_3 results in greater production of dinitrogen pentoxide (N_2O_5).

$$NO_2 + NO_3 \rightarrow N_2O_5 \qquad \text{R1.9}$$

$$N_2O_5 + M \rightarrow NO_2 + NO_3 + M \qquad \text{R1.10}$$

$$N_2O_5 + h\nu \rightarrow NO_2 + NO_3 \qquad \text{R1.11}$$

N_2O_5 has two major gas-phase destruction processes, thermal decomposition and photolysis, (R1.10 and R1.11).[1] As N_2O_5 is a nocturnal reservoir for NO_X, the subsequent reactions it undergoes affect the amount of N_2O_5 present in the morning available to photolyze. The primary loss pathway for N_2O_5 is heterogeneous loss to aqueous aerosols.

$$N_2O_5 + aerosol\ (H_2O) \rightarrow 2\ HNO_3 \qquad \text{R1.12}$$

Global models show hydrolysis of N_2O_5 lowers the tropospheric NO_x by ~15%, further reducing O_3 and OH by 5%.[11–13] While this thesis work involves laboratory experiments of N_2O_5 reacting with bulk solution, the dominant loss pathway for N_2O_5 in the atmosphere is loss to aerosol.

1.2 N_2O_5 Interfacial Chemistry

The loss process of gaseous N_2O_5 to a liquid phase aqueous aerosol is a heterogeneous reaction. The kinetics of a heterogeneous reaction captures diffusion to the surface, adsorption of the gaseous species, entry through the surface into the bulk, and rate of reaction, which can occur in the bulk and the top monolayers of the interface.[14–16] Not every molecule of N_2O_5 that collides with the surface will be adsorbed, and some molecules will evaporate back into the gas phase before they undergo hydrolysis or another reaction. Overall, the probability that a single N_2O_5 molecule is irreversibly lost to reaction is called reactive uptake coefficient (γ).[16]

$$\gamma = \frac{number\ of\ molecules\ lost}{number\ of\ molecules\ collided} \quad \text{E1.1}$$

While this is a general definition for uptake, Davidovits et al. presents an equation based on a resistor model to calculate the uptake coefficient.[15]

$$\frac{1}{\gamma} = \frac{1}{\Gamma_{diff}} + \frac{1}{\alpha} + \frac{1}{\Gamma_{rxn}+\Gamma_{sat}} \quad \text{E1.2}$$

Where Γ_{diff} is the gas phase diffusion limitation, α is the mass accommodation, Γ_{rxn} is the effect on uptake from aqueous reactions, and Γ_{sat} is the resistance caused by aqueous saturation. Γ_{diff} is proportional to the diffusion constant of N_2O_5,[17] so in experiments measuring the uptake of N_2O_5, this diffusion resistance needs to be accounted for. My experiments described in the following chapters of this thesis further discuss the reactive uptake and the effect of this diffusion resistance. It is important to note E1.2 is simplified to remove reaction at the surface layer.[15]

Galib and Limmer found that a majority of N_2O_5 hydrolysis occurs in the bulk rather than the interface, but the interfacial reaction is still an important component.[18] After the molecule reaches the surface, α, the mass accommodation, is the probability of the colliding molecule entering the aerosol particle. For N_2O_5, $\alpha = 0.93 \pm 0.06$, indicating most of the molecules that reach the surface can enter the particle.[19]

The final term of that uptake coefficient combines the effects of aqueous reaction and saturation. As N_2O_5 is very reactive, the saturation term becomes negligible, leaving $\Gamma_{rxn.}$[15] The equation for Γ_{rxn} is:[15,20]

$$\Gamma_{rxn} = \frac{4HRT}{v}\sqrt{Di * ki} \qquad \text{E1.3}$$

Where H is the Henry's law constant (determined to be 3.0 ± 0.4 M/atm at 300 K[19]), R is the ideal gas constant, T is the temperature, v is the average molecular speed, Di is the diffusion constant, and ki is the first-order rate constant of the heterogeneous reaction. D_i and k_i have subscripts, i, to denote the different potential reactions that can occur and different diffusion constants for different aerosol phases, such as aqueous and organic phases. This equation simplifies the impact of reaction resistance, when the bulk phase reaction rates are fast and dominant relative to surface reactions. Interestingly, many of these terms are also temperature dependent, *v*, D_i, k_i, and H. Studies on N_2O_5 uptake have shown decreasing the temperature results in a higher γ,[21,22] while equation E1.3 has temperature as a variable that increases uptake. Rather than the equation being wrong, this emphasizes the multiple factors that go into determining the uptake coefficient.

The N_2O_5 reactive uptake coefficient has been measured numerous times in laboratory experiments and field measurements.[23–28] The uptake value of N_2O_5 on pure water is about

0.03.[29] Decreasing the temperature results in a higher uptake value.[21,29] Several studies have suggested parameterizations for the $\gamma(N_2O_5)$, some including multiple ions, organic species, or water content. Notably, two major species that affect the uptake coefficient are water and NO_3^-. Previous studies measuring the uptake of N_2O_5 onto aqueous aerosol have found an increase in the uptake coefficient at higher relative humidities, which result in higher water contents in the aerosol. Briefly, the nitrate effect is the measured decrease in the reactive uptake of N_2O_5 in the presence of high concentrations of NO_3^-.[26] This effect begins around 1 M NO_3^-, and the uptake decreases to ~0.006 at near saturated NO_3^- concentrations.[26] A deeper analysis of the nitrate effect is presented in Chapter 4 and is a central focus for that project.

Interestingly, the reactive uptake of N_2O_5 on NaCl containing aerosols does not change significantly; the measured uptake ranged from 0.014 to 0.036 on aerosols with Cl^- concentrations ranging from 1 M to near saturation.[23,24,28,30,31] The lack of an effect of the Cl^- concentration on the uptake coefficient indicates that there is a rate limiting step prior to chlorination. A deeper analysis on potential mechanisms of N_2O_5 and the effect of uptake is presented in Chapter 4.

Fields measurements of the uptake coefficient of N_2O_5 are often significantly lower than 0.03. Results of the modeled N_2O_5 uptake from the WINTER flight campaign in 2015 found a wide range in uptake coefficient (Figure 1.1).[27] While most uptake values ranged from 0.01 to 0.1, a significant amount were less than 0.01, with a few results lower than 0.001, 30 times smaller than γ of N_2O_5 on pure water. The presence of organic molecules, generally surface-active species, has been measured to decrease the reactive uptake coefficient of N_2O_5.

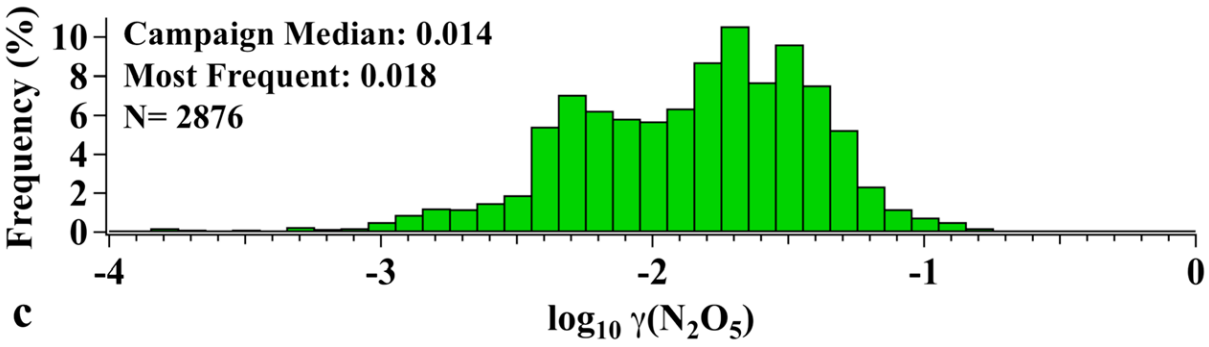

Figure 1-1 Histogram plot of modeled N_2O_5 uptake from measurements taken during the WINTER 2015 flight campaign, published in McDuffie et al 2018.[27]

1.3 Product Yield of $ClNO_2$

Due to the high abundance of Cl^- in marine aerosol, the reaction of N_2O_5 and Cl^- to form $ClNO_2$ has been studied extensively in both laboratory settings and measured in field campaigns.[24,32,33] The reaction to form $ClNO_2$ is:

$$N_2O_5 + Cl^- \rightarrow ClNO_2 + NO_3^- \qquad \text{R1.13}$$

Behnke et al. determined a solubility constant (H = 0.024 M/atm) and hydrolysis rate (270 s^{-1}) for $ClNO_2$, significantly less soluble and less reactive compared to N_2O_5.[24] With low solubility in aqueous aerosol, $ClNO_2$ has a significant loss process after evaporating to the gas phase. During daytime, $ClNO_2$ can photolyze to form a chlorine radical (Cl) and an NO_2 molecule.

$$ClNO_2 + h\nu \rightarrow Cl + NO_2 \qquad \text{R1.14}$$

Cl radicals can oxidize VOCs,[34,35] leading to O_3 formation.[34] Adding $ClNO_2$ production from R1.14 into models can result in higher predicted O_3 and OH concentrations, up to 10% and 20%, respectively.[33,34] Additionally, the chlorination reaction returns an NO_2 molecule back to the gas phase, instead of forming NO_3^- if N_2O_5 underwent hydrolysis.

Figure 1.2 shows the $ClNO_2$ production from various studies, including the project described in Chapter 3. The product yield is considered equivalent to the $ClNO_2$ branching

fraction, referring to the amount of $ClNO_2$ produced relative to 100% conversion of N_2O_5 into $ClNO_2$ in saturated NaCl solutions and aerosol.[36] The presence of 10% $ClNO_2$ product at millimolar concentrations, 5-10 mM, underscores the favorability for this reaction. The ratio of rate constants for the chlorination and hydrolysis reactions of N_2O_5 is k_{Cl^-}/k_{water} = 400-1000.[24–26,36]

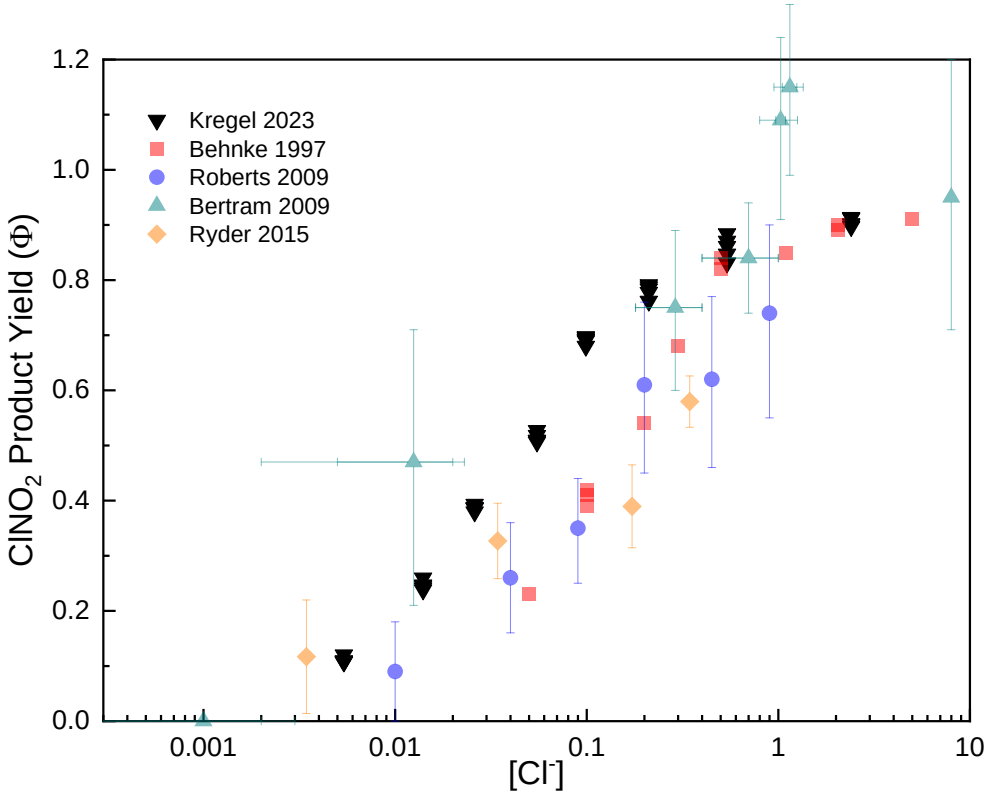

Figure 1-2 Plot of the $ClNO_2$ product yield as a function of the chloride concentration. Plot includes data from Chapter 3 and references.[24–26,36,37]

The higher rate constant for the chlorination reaction contrasts with the thermodynamic calculations for the Gibbs free energy ($\Delta G°$) of these reactions. Starting from the gas phase, the overall reactions are:

$$N_2O_5\ (g) + H_2O\ (l) \rightleftarrows 2NO_3^-\ (aq) + 2H^+\ (aq) \qquad \text{R1.15}$$

$$N_2O_5\ (g) + Cl^-\ (aq) \rightleftarrows ClNO_2\ (g) + NO_3^-\ (aq) \qquad R1.16$$

$\Delta G°$ for the chlorination reaction is -43 kJ/mol, while $\Delta G°$ for the hydrolysis pathway is -103 kJ/mol.[36,38] This difference in the $\Delta G°$ indicates the hydrolysis pathway is very thermodynamically favored, and nearly all molecules of N_2O_5 should undergo this reaction. However, Figure 1.2 and the rate constant ratio favoring chlorination by 400-1000 times indicate otherwise. Additionally, the activation energies do not account for this discrepancy. As detailed later in Chapter 3, the activation energy of the hydrolysis reaction is only 3 kJ/mol larger than the chlorination reaction.[36] This has led to using entropic and dynamic factors to explain the preference or chlorination.[39] Losing the solvation shell around Cl^- is entropically favored as opposed to forming a solvation shell around two NO_3^- products from hydrolysis.

While laboratory studies measure a high product yield for $ClNO_2$, some field measurements find a significantly lower production of $ClNO_2$ despite high Cl^- concentrations in the aerosol.[33,40] This decreased production was attributed to competition between Cl^- and organic species for reaction with N_2O_5. Ryder et al. measured a decrease in the $ClNO_2$ formed with phenol present in solution, particularly the interfacial region.[37] Sulfate and acetate have also been found to reduce the production of $ClNO_2$ from chloride solutions, though perchlorate had no effect.[41] The decreased $ClNO_2$ production is attributed to competition of the other solutes with Cl^- for the highly reactive N_2O_5, rather than enhanced loss of $ClNO_2$, similar to the effect of organics.[37,41]

1.4 Remaining Questions of N_2O_5

N_2O_5 has a relatively high uptake coefficient on pure aqueous aerosol and solution, and fast reaction rates with dissolved and surface-active species. Viewing this from a more generalized perspective, the reaction pathways of N_2O_5 are an example of competition between a

solute-solvent reaction, solvolysis, and solute-solute reactions. It is difficult to individually probe the reaction of N_2O_5 with Cl^- or another species without water present. Experiments with an alternative, non-reactive solvent could be considered, but the reaction mechanism could change. The solvation shell around N_2O_5 impacts hydrolysis, and additional solutes can influence the solvation shell.[19,36,42] Many published rate constants for N_2O_5 are more accurately rate constant ratios, usually comparing the reaction rate of a species with the chlorination or hydrolysis rate. While our experiments are not able to fully separate our analysis of a single reaction, we focused on filling in some of the gaps of knowledge present in the fundamental reactions of N_2O_5, particularly with water, Cl^-, and NO_3^-.

1.5 Overview of Chapters

The work presented in this thesis uses chemical ionization mass spectrometry, along with 0-dimensional and 1-dimensional box modeling, to investigate the fundamental reactions of N_2O_5 with water, Cl^-, and NO_3^-. These projects help develop a stronger knowledge base to understand the factors involved in the mechanisms of N_2O_5 reactions.

Chapter 2 provides a detailed description of the instrument setup used for the experiments. It contains a walkthrough of the methods to produce N_2O_5, the dual channel flow reactor designed for these experiments, and the chemical ionization mass spectrometer used for species detection. Additional experiments focused on understanding the physical and chemical nature of the experimental setup are presented.

Chapter 3 is a direct print of Kregel et al. 2023, published in the ACS Journal of Physical Chemistry A. It details experiments performed by Steven Kregel and me to interrogate the effect of temperature on the product yield of $ClNO_2$. We found a very minor effect of lower temperatures slightly increasing the $ClNO_2$ product yield. Professor David Limmer and Seokjin

Moon at the University of California-Berkeley were co-authors on this manuscript and provided molecular dynamics simulations of solvated N_2O_5 and Cl^- to aid in our analysis.

Chapter 4 details our experiments to understand the role of NO_3^- on the reactions of N_2O_5 with nitrate- and chloride-containing solutions. Using isotopically labelled $^{15}NO_3^-$, we detected the production of labeled species from solution, $^{14,15}N_2O_5$, $^{15,15}N_2O_5$, and $Cl^{15}NO_2$, which were created from reaction of N_2O_5 with nitrate. Professor Manabu Shiraiwa and Dr. Pascale Lakey are collaborators on this project, providing their kinetic model to assist in both analyzing our data and interrogating the physical conditions of our flow reactor system. Our intention is to publish the results of this project in the ACS Journal of Physical Chemistry A.

1.6 References

(1) Brown, S. S.; Stutz, J. Nighttime Radical Observations and Chemistry. *Chem. Soc. Rev.* **2012**, *41* (19), 6405. https://doi.org/10.1039/c2cs35181a.

(2) Rowland, F. S. Stratospheric Ozone Depletion. *Philos. Trans. R. Soc. B Biol. Sci.* **2006**, *361* (1469), 769–790. https://doi.org/10.1098/rstb.2005.1783.

(3) Barbara Finlayson-Pitts; James Pitts, Jr. *Chemistry of the Upper and Lower Atmosphere: Theory, Experiments, and Applications*; 2000.

(4) Finlayson-Pitts, B. J.; Pitts, J. N. Atmospheric Chemistry of Tropospheric Ozone Formation: Scientific and Regulatory Implications. *Air Waste* **1993**, *43* (8), 1091–1100. https://doi.org/10.1080/1073161X.1993.10467187.

(5) Lamsal, L. N.; Martin, R. V.; Van Donkelaar, A.; Steinbacher, M.; Celarier, E. A.; Bucsela, E.; Dunlea, E. J.; Pinto, J. P. Ground-level Nitrogen Dioxide Concentrations Inferred from the Satellite-borne Ozone Monitoring Instrument. *J. Geophys. Res. Atmospheres* **2008**, *113* (D16), 2007JD009235. https://doi.org/10.1029/2007JD009235.

(6) Delmas, R.; Serca, D.; Jambert, C. Global Inventory of NOx Sources.

(7) Stark, H.; Lerner, B. M.; Schmitt, R.; Jakoubek, R.; Williams, E. J.; Ryerson, T. B.; Sueper, D. T.; Parrish, D. D.; Fehsenfeld, F. C. Atmospheric in Situ Measurement of Nitrate Radical (NO_3) and Other Photolysis Rates Using Spectroradiometry and Filter Radiometry. *J. Geophys. Res. Atmospheres* **2007**, *112* (D10), 2006JD007578. https://doi.org/10.1029/2006JD007578.

(8) Yan, Y.; Wang, S.; Zhu, J.; Guo, Y.; Tang, G.; Liu, B.; An, X.; Wang, Y.; Zhou, B. Vertically Increased NO3 Radical in the Nocturnal Boundary Layer. *Sci. Total Environ.* **2021**, *763*, 142969. https://doi.org/10.1016/j.scitotenv.2020.142969.

(9) Platt, U.; Perner, D.; Schröder, J.; Kessler, C.; Toennissen, A. The Diurnal Variation of NO_3. *J. Geophys. Res. Oceans* **1981**, *86* (C12), 11965–11970. https://doi.org/10.1029/JC086iC12p11965.

(10) Allan, B. J.; Plane, J. M. C.; Coe, H.; Shillito, J. Observations of NO_3 Concentration Profiles in the Troposphere. *J. Geophys. Res. Atmospheres* **2002**, *107* (D21). https://doi.org/10.1029/2002JD002112.

(11) Holmes, C. D.; Bertram, T. H.; Confer, K. L.; Graham, K. A.; Ronan, A. C.; Wirks, C. K.; Shah, V. The Role of Clouds in the Tropospheric NOx Cycle: A New Modeling Approach for Cloud Chemistry and Its Global Implications. *Geophys. Res. Lett.* **2019**, *46* (9), 4980–4990. https://doi.org/10.1029/2019GL081990.

(12) Evans, M. J.; Jacob, D. J. Impact of New Laboratory Studies of N_2O_5 Hydrolysis on Global Model Budgets of Tropospheric Nitrogen Oxides, Ozone, and OH. *Geophys. Res. Lett.* **2005**, *32* (9), 2005GL022469. https://doi.org/10.1029/2005GL022469.

(13) MacIntyre, H. L.; Evans, M. J. Sensitivity of a Global Model to the Uptake of N2O5 by Tropospheric Aerosol. *Atmospheric Chem. Phys.* **2010**, *10* (15), 7409–7414. https://doi.org/10.5194/acp-10-7409-2010.

(14) Wilson, K. R.; Prophet, A. M. Chemical Kinetics in Microdroplets.

(15) Davidovits, P.; Kolb, C. E.; Williams, L. R.; Jayne, J. T.; Worsnop, D. R. Mass Accommodation and Chemical Reactions at Gas−Liquid Interfaces. *Chem. Rev.* **2006**, *106* (4), 1323–1354. https://doi.org/10.1021/cr040366k.

(16) Ammann, M.; Pöschl, U.; Rudich, Y. Effects of Reversible Adsorption and Langmuir–Hinshelwood Surface Reactions on Gas Uptake by Atmospheric Particles. *Phys Chem Chem Phys* **2003**, *5* (2), 351–356. https://doi.org/10.1039/B208708A.

(17) Poschl, U.; Rudich, Y.; Ammann, M. Kinetic Model Framework for Aerosol and Cloud Surface Chemistry and Gas-Particle Interactions – Part 1: General Equations, Parameters, and Terminology. *Atmos Chem Phys* **2007**.

(18) Galib, M.; Limmer, D. T. Reactive Uptake of N2O5 by Atmospheric Aerosol Is Dominated by Interfacial Processes. *Science* **2021**, *371* (6532), 921–925. https://doi.org/10.1126/science.abd7716.

(19) Cruzeiro, V. W. D.; Galib, M.; Limmer, D. T.; Götz, A. W. Uptake of N2O5 by Aqueous Aerosol Unveiled Using Chemically Accurate Many-Body Potentials. *Nat. Commun.* **2022**, *13* (1). https://doi.org/10.1038/s41467-022-28697-8.

(20) P. V. Danckwerts. Absorption by Simultaneous Diffusion and Chemical Reaction into Particles of Various Shapes and Falling Drops. *Trans Faraday Soc* **1951**.

(21) Griffiths, P. T.; Cox, R. A. Temperature Dependence of Heterogeneous Uptake of N2O5 by Ammonium Sulfate Aerosol. *Atmospheric Sci. Lett.* **2009**, *10* (3), 159–163. https://doi.org/10.1002/asl.225.

(22) Robinson, G. N.; Worsnop, D. R.; Jayne, J. T.; Kolb, C. E.; Davidovits, P. Heterogeneous Uptake of ClONO2 and N2O5 by Sulfuric Acid Solutions. *J. Geophys. Res.* **1997**, *102*, 3583–3601.

(23) George, C.; Ponche, J. L.; Mirabel, P.; Behnke, W.; Scheer, V.; Zetzsch, C. Study of the Uptake of N2O5 by Water and NaCl Solutions. *J. Phys. Chem.* **1994**, *98* (35), 8780–8784. https://doi.org/10.1021/j100086a031.

(24) Behnke, W.; George, C.; Scheer, V.; Zetzsch, C. Production and Decay of ClNO2 from the Reaction of Gaseous N2O5 with NaCl Solution: Bulk and Aerosol Experiments. *J. Geophys. Res. Atmospheres* **1997**, *102* (3), 3795–3804. https://doi.org/10.1029/96jd03057.

(25) Roberts, J. M.; Osthoff, H. D.; Brown, S. S.; Ravishankara, A. R.; Coffman, D.; Quinn, P.; Bates, T. Laboratory Studies of Products of N2O5 Uptake on Cl- Containing Substrates. *Geophys. Res. Lett.* **2009**, *36* (20), 1–5. https://doi.org/10.1029/2009GL040448.

(26) Bertram, T. H.; Thornton, J. A. Toward a General Parameterization of N2O5 Reactivity on Aqueous Particles: The Competing Effects of Particle Liquid Water, Nitrate and Chloride. *Atmos Chem Phys* **2009**.

(27) McDuffie, E. E.; Fibiger, D. L.; Dubé, W. P.; Lopez-Hilfiker, F.; Lee, B. H.; Thornton, J. A.; Shah, V.; Jaeglé, L.; Guo, H.; Weber, R. J.; Michael Reeves, J.; Weinheimer, A. J.; Schroder, J. C.; Campuzano-Jost, P.; Jimenez, J. L.; Dibb, J. E.; Veres, P.; Ebben, C.; Sparks, T. L.; Wooldridge, P. J.; Cohen, R. C.; Hornbrook, R. S.; Apel, E. C.; Campos, T.; Hall, S. R.; Ullmann, K.; Brown, S. S. Heterogeneous N2O5 Uptake During Winter: Aircraft Measurements During the 2015 WINTER Campaign and Critical Evaluation of Current Parameterizations. *J. Geophys. Res. Atmospheres* **2018**, *123* (8), 4345–4372. https://doi.org/10.1002/2018JD028336.

(28) Stewart, D. J.; Griffiths, P. T.; Cox, R. A. Reactive Uptake Coefficients for Heterogeneous Reaction of N2O5 with Submicron Aerosols of NaCl and Natural Sea Salt. *Atmospheric Chem. Phys.* **2004**, *4* (5), 1381–1388. https://doi.org/10.5194/acp-4-1381-2004.

(29) Van Doren, J. M.; Watson, L. R.; Davidovits, Paul.; Worsnop, D. R.; Zahniser, M. S.; Kolb, C. E. Temperature Dependence of the Uptake Coefficients of Nitric Acid, Hydrochloric Acid and Nitrogen Oxide (N2O5) by Water Droplets. *J. Phys. Chem.* **1990**, *94* (8), 3265–3269. https://doi.org/10.1021/j100371a009.

(30) Gaston, C. J.; Thornton, J. A. Reacto-Diffusive Length of N2O5 in Aqueous Sulfate- and Chloride-Containing Aerosol Particles. *J. Phys. Chem. A* **2016**, *120* (7), 1039–1045. https://doi.org/10.1021/acs.jpca.5b11914.

(31) McNeill, V. F.; Patterson, J.; Wolfe, G. M.; Thornton, J. A. The Effect of Varying Levels of Surfactant on the Reactive Uptake of N2O5 to Aqueous Aerosol. *Atmos Chem Phys* **2006**.

(32) Kercher, J. P.; Riedel, T. P.; Thornton, J. A. Chlorine Activation by N2O5: Simultaneous, in Situ Detection of ClNO2 and N2O5 by Chemical Ionization Mass Spectrometry. *Atmos Meas Tech* **2009**.

(33) McDuffie, E. E.; Fibiger, D. L.; Dubé, W. P.; Lopez Hilfiker, F.; Lee, B. H.; Jaeglé, L.; Guo, H.; Weber, R. J.; Reeves, J. M.; Weinheimer, A. J.; Schroder, J. C.; Campuzano-Jost, P.; Jimenez, J. L.; Dibb, J. E.; Veres, P.; Ebben, C.; Sparks, T. L.; Wooldridge, P. J.; Cohen, R. C.; Campos, T.; Hall, S. R.; Ullmann, K.; Roberts, J. M.; Thornton, J. A.; Brown, S. S. $ClNO_2$ Yields From Aircraft Measurements During the 2015 WINTER Campaign and Critical Evaluation of the Current Parameterization. *J. Geophys. Res. Atmospheres* **2018**, *123* (22). https://doi.org/10.1029/2018JD029358.

(34) Sarwar, G.; Simon, H.; Xing, J.; Mathur, R. Importance of Tropospheric $ClNO_2$ Chemistry across the Northern Hemisphere. *Geophys. Res. Lett.* **2014**, *41* (11), 4050–4058. https://doi.org/10.1002/2014GL059962.

(35) Fantechi, G.; Jensen, N. R.; Saastad, O.; Hjorth, J.; Peeters, J. Reactions of Cl Atoms with Selected VOCs: Kinetics, Products and Mechanisms. *J Atmos. Chem.* **1998**. *31,* 247-267.

(36) Kregel, S. J.; Derrah, T. F.; Moon, S.; Limmer, D. T.; Nathanson, G. M.; Bertram, T. H. Weak Temperature Dependence of the Relative Rates of Chlorination and Hydrolysis of N_2O_5 in NaCl–Water Solutions. *J. Phys. Chem. A* **2023**, *127* (7), 1675–1685. https://doi.org/10.1021/acs.jpca.2c06543.

(37) Ryder, O. S.; Campbell, N. R.; Shaloski, M.; Al-Mashat, H.; Nathanson, G. M.; Bertram, T. H. Role of Organics in Regulating ClNO2 Production at the Air-Sea Interface. *J. Phys. Chem. A* **2015**, *119* (31), 8519–8526. https://doi.org/10.1021/jp5129673.

(38) Haynes, W. M. *CRC Handbook of Chemistry and Physics*.

(39) Limmer, D. T.; Götz, A. W.; Bertram, T. H.; Nathanson, G. M. Molecular Insights into Chemical Reactions at Aqueous Aerosol Interfaces. *Annu. Rev. Phys. Chem.* **2024**, *75* (1), 111–135. https://doi.org/10.1146/annurev-physchem-083122-121620.

(40) Kim, M. J.; Farmer, D. K.; Bertram, T. H. A Controlling Role for the Air−sea Interface in the Chemical Processing of Reactive Nitrogen in the Coastal Marine Boundary Layer. *Proc. Natl. Acad. Sci.* **2014**, *111* (11), 3943–3948. https://doi.org/10.1073/pnas.1318694111.

(41) Staudt, S.; Gord, J. R.; Karimova, N. V.; McDuffie, E. E.; Brown, S. S.; Gerber, R. B.; Nathanson, G. M.; Bertram, T. H. Sulfate and Carboxylate Suppress the Formation of ClNO2 at Atmospheric Interfaces. *ACS Earth Space Chem.* **2019**, *3* (9), 1987–1997. https://doi.org/10.1021/acsearthspacechem.9b00177.

(42) Rossich Molina, E.; Gerber, R. B. Microscopic Mechanisms of N2O5 Hydrolysis on the Surface of Water Droplets. *J. Phys. Chem. A* **2020**, *124* (1), 224–228. https://doi.org/10.1021/acs.jpca.9b08900.

Chapter 2. Experimental Description of N_2O_5 Synthesis, Flow Reactor, and Chemical Ionization Mass Spectrometer

2.1 Overview

This chapter details the various components of my experimental setup and the intricacies and improvements we have uncovered. This includes our method for synthesizing dinitrogen pentoxide (N_2O_5), the flow reactor system where the reactions of interest take place, and the chemical ionization mass spectrometer (CIMS) instrument we use for species detection. Much of this experimental work has been done with the help of Steven Kregel, a former post-doctoral researcher in the Bertram and Nathanson research groups. Additional experiments are described, which provided a better understanding of the system, but were not directly attached to a major project in Chapter 3 and 4.

2.2 Synthesis of N_2O_5

The overall design of the N_2O_5 synthesis setup is based on Bertram et al. 2009.[1] Much of the equipment used to generate N_2O_5 for an experiment was set up prior to my work on the instrument setup. In the experimental setup, we use PFA and PTFE tubing and fittings to reduce reaction rate with N_2O_5 by the tubing material or H_2O deposited on the walls. Fahey et al. found that PFA tubing resulted in less N_2O_5 loss compared to pyrex or stainless steel.[2] Some experiments using N_2O_5 have relied on synthesizing then depositing N_2O_5 into a solid.[2–4] In my experiments, the N_2O_5 was synthesized in situ for use in a flow reactor. This avoids issues with collection and storage of N_2O_5; however, day-to-day variations, such as flow rate differences and the temperature of the laboratory can affect the concentration of N_2O_5 produced. As a result, we designed experiments to be run over a few hours or a single day. Additionally, we often focused on the products from solution rather than the loss of N_2O_5 to solutions. Further issues with the uptake of N_2O_5 are described in the next section concerning the flow reactor.

The synthesis of N_2O_5 comes from the gas phase reaction of nitrogen dioxide (NO_2) and the nitrate radical (NO_3). We have three cylinders we need for our process: N_2 (Ultra High Purity), Air (Ultra Zero), and NO_2 (~50 ppm NO_2 balanced in N_2). These tanks are ordered from AirGas, and the part numbers are NI UHP300 (N_2), AI UZ300 (Zero Air), and X02NI99C15W0074 (~50 ppm NO_2 in N_2). The N_2 tank is generally replaced every 4-6 months, and the Zero Air and NO_2 cylinders can last a year or more, depending on the amount used and experiments ran. We use Ultra High Purity N_2 and Ultra Zero Air because we want to avoid as much potential contamination in the N_2O_5 synthesis box as possible. The biggest contaminant in the system would be H_2O, as N_2O_5 (and NO_2 and NO_3) can react with H_2O to form nitric acid.[5] To this end, we flow the N_2 and Zero Air lines through potassium hydroxide (KOH) pellets, to remove any potential additional H_2O. The NO_2 does not flow over KOH pellets, as NO_2 adsorbs to KOH surfaces.[6] Instead, the NO_2 flow passes through nylon mesh, a technique used previously by members of the Nathanson group.[3] This nylon mesh reacts with HNO_3, trapping the molecule and forming a yellow-brown stain. In our setup, nylon mesh is both wrapped around a glass tube and placed inside the tube to ensure the NO_2 gas flow has as much contact with the mesh as possible. Early on during my initial experiments, we noted a relatively high nitric acid signal in the instrument and traced a significant amount of nitric acid signal from the first NO_2 tank used. Given the NO_2 source was an old tank, it is possible there was some water contamination; over time, more and more HNO_3 formed in the cylinder. The nylon mesh was added and the amount of HNO_3 from the tank dropped substantially, but the NO_2 concentration seemed unaffected. I do not have an estimated time for how frequently to change the mesh, but it should be changed when the color becomes significant. Additional tests to reduce HNO_3 from the cylinder included flowing NO_2 gas over 3Å molecular sieves. However, NO_2 appeared to adsorb to these sieves as

we detected no N_2O_5 in the instrument when the sieves were included, thus nullifying the purpose of using sieves to reduce HNO_3.

A schematic of the N_2O_5 synthesis setup is shown in Figure 2.1. Once the N_2 and Zero Air gases are flowed over KOH pellets, they are combined in a small reaction chamber with a mercury pen lamp (Jelight 95-2100-1). This lamp produces short wavelength UV light (185 and 254 nm) to produce ozone (O_3) from the O_2 present in the Zero Air flow. The reason we combine Zero Air and N_2 instead of using solely Zero Air or a pure O_2 cylinder is because we want a low O_3 environment in the reaction chamber with NO_2. High amounts of O_3 can lead to complications in the signals measured in the instrument, described in a later section. Over time, this pen lamp will lose efficiency, usually through clouding of the quartz on the lamp. If this lower efficiency becomes a significant issue, the lamp can be replaced. After producing O_3, the resulting gas flow is mixed with the NO_2 flow in a larger reaction vessel. The vessel has a 30 cm length and 2 cm inner radius, leading to a chamber volume of 380 cm^3. It is wrapped in black electrical tape to reduce potential photolysis of N_2O_5. The gas-phase reactions to form N_2O_5, in excess NO_2, are:[5]

$$O_2 + h\nu \rightarrow 2O \qquad \text{R2.1}$$

$$O + O_2 \rightarrow O_3 \qquad \text{R2.2}$$

$$NO_2 + O_3 \rightarrow NO_3 + O_2 \qquad \text{R2.3}$$

$$NO_3 + NO_2 \leftrightarrow N_2O_5 \qquad \text{R2.4}$$

The resulting flow of N_2O_5, with N_2, O_2, O_3, NO_2, NO_3, is directed towards flow reactor, described later in section 2.3.

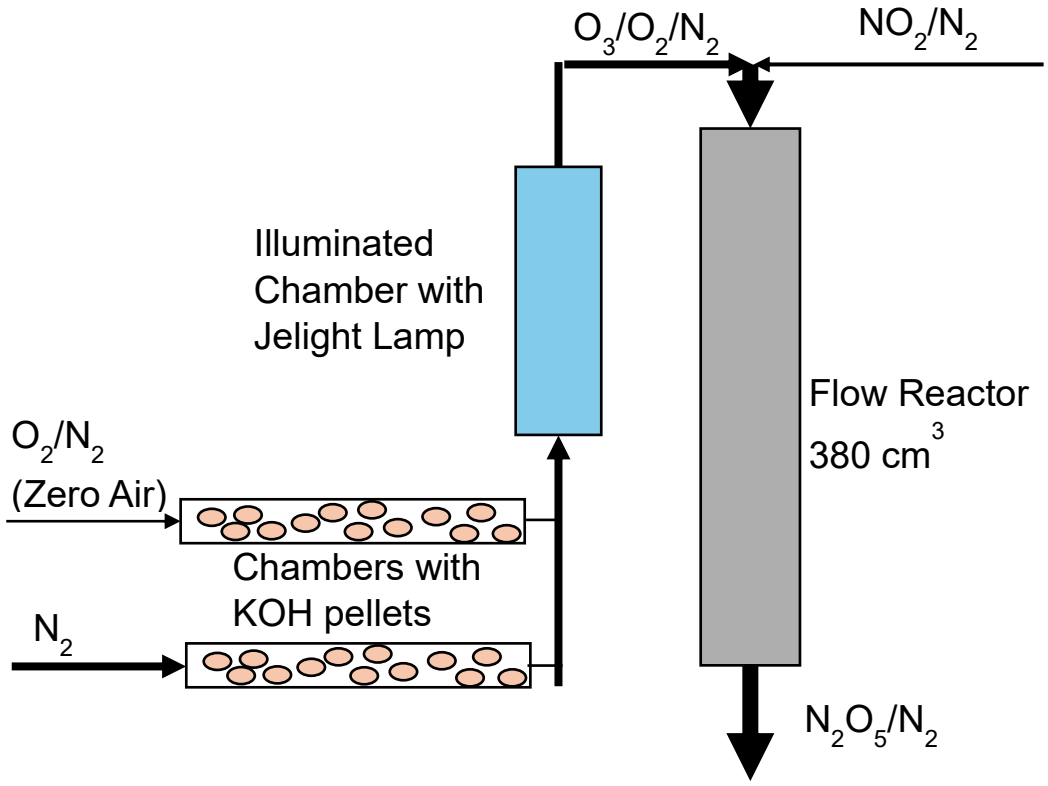

Figure 2-1 Cartoon schematic of the N_2O_5 synthesis setup

The flow rates from each cylinder can be altered, changing the concentrations of species in the flow reactor; more Zero Air would produce more O_3 and thus more N_2O_5 and other products, while more N_2 would shorten the reaction time in the vessel and dilute the concentrations of O_3 and NO_2. For most of my experiments, I used 8.4 sccm of 50 ppm NO_2 (the exact concentration of NO_2 is recorded on the certificate of analysis from Airgas), ~2 sccm of Zero Air, and 140 sccm of N_2. The NO_2 flow is maintained by a mass flow controller (MFC), which keeps the flow rate steady. However, the N_2 and Zero Air flows rely on a mass flow meter (MFM) to monitor the actual flow rate of these gases. Needle valves are used to increase or decrease these flows. Due to the necessary low flow rate of Zero Air, and the subsequent need for a low pressure from the cylinder regulator (the gauge reading just above 0 psi) to keep the flow

rate low, I experienced issues with ensuring a constant flow of Zero Air. Since we are in an O_3-limited environment, changes to the O_3 concentration can have significant impacts on the N_2O_5 concentration. To help maintain a constant Zero Air flow, we added a "bleed valve" near the Zero Air cylinder. This allows us to have a higher pressure in the regulator and maintain a steadier flow through the needle valve and MFM. However, the trade-off is that a significant amount of Zero Air is lost, and we deplete through the gas cylinder significantly faster. An alternative setup using a critical orifice in the Zero Air line has been suggested to allow for a higher pressure at the cylinder regulator and lower pressure at the needle valve and MFM.

To determine an ideal ratio of NO_2 and Zero Air, I ran an experiment to determine the magnitude of the signal of $I(N_2O_5)^-$ in the instrument at various NO_2 and Zero Air concentrations (Figure 2.2). The increase in Zero Air had a stronger effect on the N_2O_5 signal since we initially ran in an O_3-limited regime. As one might expect, the highest concentration of NO_2 and Zero Air (to form O_3) resulted in the highest signal of N_2O_5. However, other species appeared in the mass scan when we run in a high NO_2, high O_3 regime. Figure 2.3 shows the presence of $NO_3^-(D_2O)$, $NO_3^-(D_2O)_2$, $NO_3^-(D_2O)_3$, and $NO_3^-(DNO_3)$ and their signals relative to the I^- peak when the N_2O_5 box is run at a higher Zero Air. The N_2O_5 peak does not only stay as N_2O_5 in the ion-molecule reactor (IMR), but breaks apart, forming nitrate clusters. Additionally, if significant amounts of O_3 enter the IMR, they can react with I^- to form IO^- and O_2.[7] With the amount of DNO_3 present, the IO^- can steal a deuterium to form DOI and remove ion current away from $I(N_2O_5)^-$ pathways. This is a major reason for our decision to keep the Zero Air flow rate at ~2 sccm. We did not increase the NO_2 flow above 8.4 sccm because the MFC on that line has a maximum flow rate of 10 sccm, and we wanted to avoid being too close to the extreme end of the range.

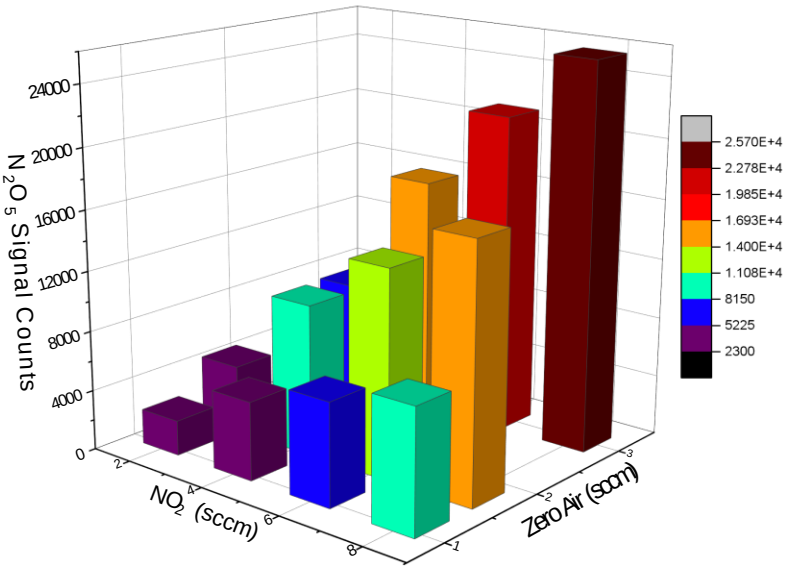

Figure 2-2 A 3-dimensional plot showing the change in N_2O_5 signal in the instrument as I varied NO_2 from 2 to 8 sccm (bottom left axis) and Zero Air from 1.1 to 3 sccm (right axis).

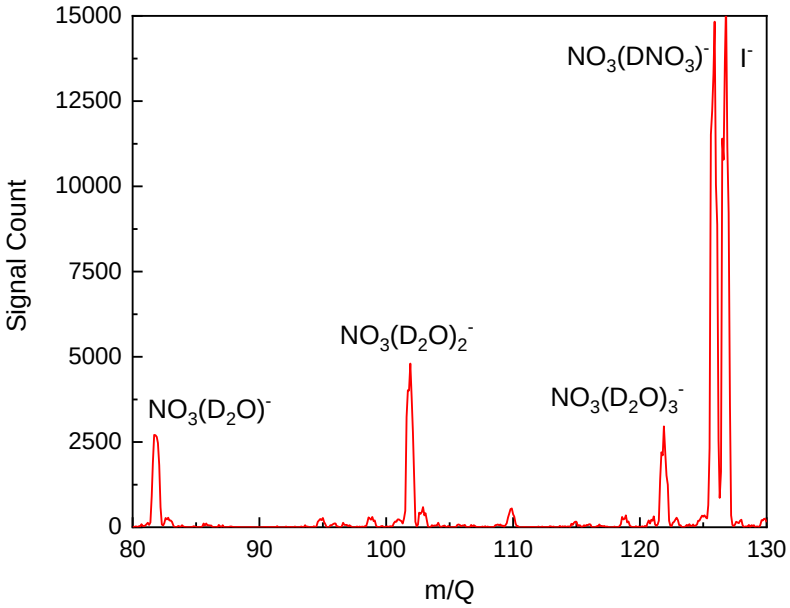

Figure 2-3 Mass scan of taken of N_2O_5 gas flow over D_2O solution, zoomed in on the 80 to 130 m/Q range to highlight the NO_3^--D_2O clusters and $NO_3^-(DNO_3)$ peaks.

We used a 0-dimensional box model set up in MATLAB to predict a concentration of N_2O_5 from the reactor box. This model was originally written by Tim Bertram for use in his Chem 629 class: Atmospheric Chemical Mechanisms, using kinetic rates from Jet Propulsion Lab's Chemical Kinetics publication.[8] I removed several side reactions to focus solely on NO_2, O_3, NO_3, and N_2O_5. The total time to run is dependent on the flow rate through the system (the reaction vessel volume divided by the sum of NO_2, N_2, and Zero Air flow rates). The pressure and temperature can be changed but in our experiments they would generally be constant. The reactive uptake probability, called "gamma" in the model, for N_2O_5 and NO_3, and the subsequent surface area, detail the loss of N_2O_5 in the system. Generally, I set the gammas = 0, which assumes there is no loss to the walls and provides an upper bound on the expected N_2O_5 concentration. It is difficult to estimate the actual gamma on the glass and PFA walls, though I would expect it to be low due to constant flow of dry gases keeping the humidity low. Additionally, the box model uptake is designed for well mixed aerosol rather than wall loss, so the uptake would involve further estimation. The model allows for inputting initial concentrations of species (in parts per billion).

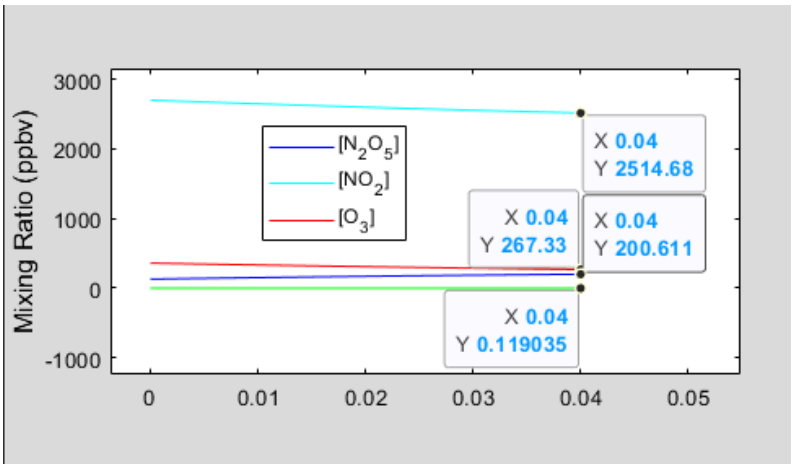

Figure 2-4 MATLAB plot of the modeled concentrations of N_2O_5, NO_2, O_3, and NO_3.

I generally assume NO, N_2O_5, NO_3, and HNO_3 = 0, starting with only NO_2 and O_3. The NO_2 concentration is determined from the flow rate from the NO_2 cylinder, diluted from the additional N_2 and Zero Air. The O_3 concentration needs to be measured from the N_2O_5 box. The concentration of O_3 was measured with a 2B Technologies Personal Ozone Monitor from the box with the NO_2 flow closed off. With the concentrations known, they can be inputted into the MATLAB model, and the resulting plot provides the calculated final concentrations for N_2O_5, NO_2, NO_3, and O_3 (Figure 2.4). The figure shows the high NO_2 regime the synthesis occurs in.

An additional setup we attempted to add to improve N_2O_5 and reduce HNO_3 concentrations was a diphosphorus pentoxide (P_2O_5) trap. P_2O_5 reacts with HNO_3 to form N_2O_5, and has been used in experiments to increase the N_2O_5 concentration and reduce HNO_3.[3] For our setup, N_2O_5 flow was pushed through a mixture of powdered P_2O_5 and glass beads. However, we were not able to detect any N_2O_5 in the resulting gas flow. It is possible the high surface area of the powder resulted in nearly all the N_2O_5 adsorbing to the particles, or perhaps there was some contamination of the P_2O_5 resulting in N_2O_5 loss. We removed the P_2O_5 trap and returned the synthesis setup to its previous arrangement.

2.3 Flow Reactor Schematic

The flow reactor and solution holders we used were designed to measure N_2O_5 reactions with aqueous solutions and resulting products. Previous research in our group used a different flow reactor designed by Allan Bertram's research group at University of British Colombia.[9] This reactor was able to measure the uptake of a reactive gas, such as N_2O_5 onto glycerol and ethylene glycol.[10] However, to conduct these experiments, the reactor cell needed to be held at a low pressure, ~8 Torr. We attempted to use this reactor cell with aqueous solution, but the vapor pressure of H_2O at 298 K = 24 Torr, meaning the solution would fully evaporate over the course

of an experiment. Cooling the solution lowers the H_2O vapor pressure, but there would still be significant evaporation. This becomes a further issue when introducing salts to the aqueous solution, as the changing concentration throughout an experiment would skew the results. As an alternative option for experiments, Steven Kregel designed a new dual channel flow reactor system.

The boat reactor system consists of Teflon boats set in an aluminum block (Figure 2.5). The dimensions for the Teflon boats are shown in Figure 2.6. The total volume of the central region which holds the 31.36 cm^3 (2.159 cm x 1.271 cm x 11.429 cm). As most of our experiments used 20 mL of solution, with 11.36 cm^3 of headspace above the solution, resulting in a gas residence time of 0.59 s when flowing 2 LPM of N_2 carrier through the boats or 0.41 s when flowing 3 LPM of N_2 carrier.

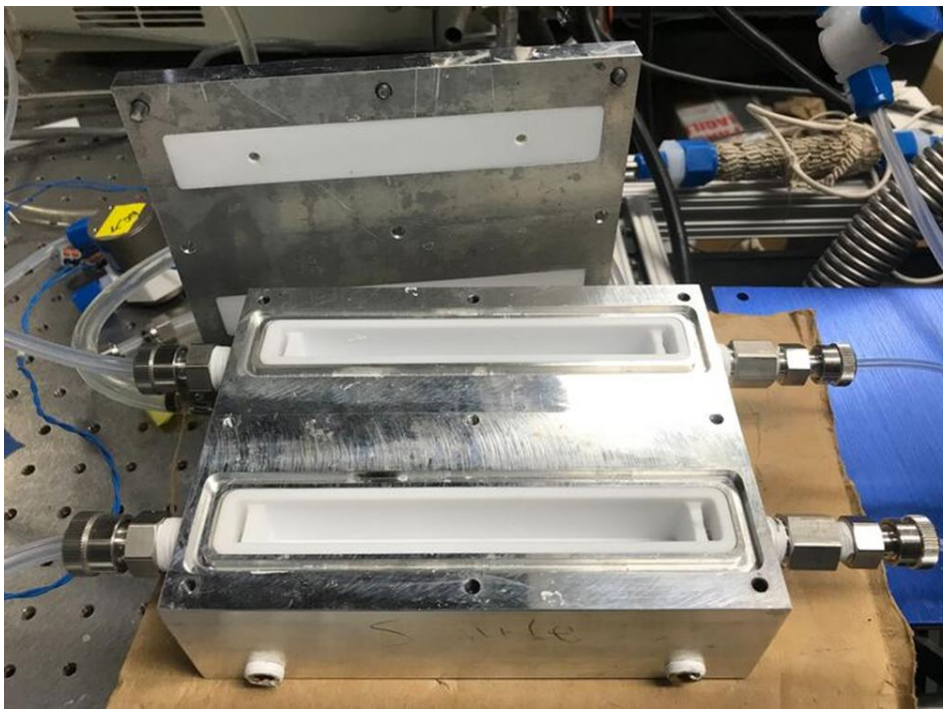

Figure 2-5 A picture of the dual channel flow reactor system. Teflon boats which contain solutions to measure are set in an aluminum block. PFA tubing flows N_2O_5 in and out of the boat headspace.

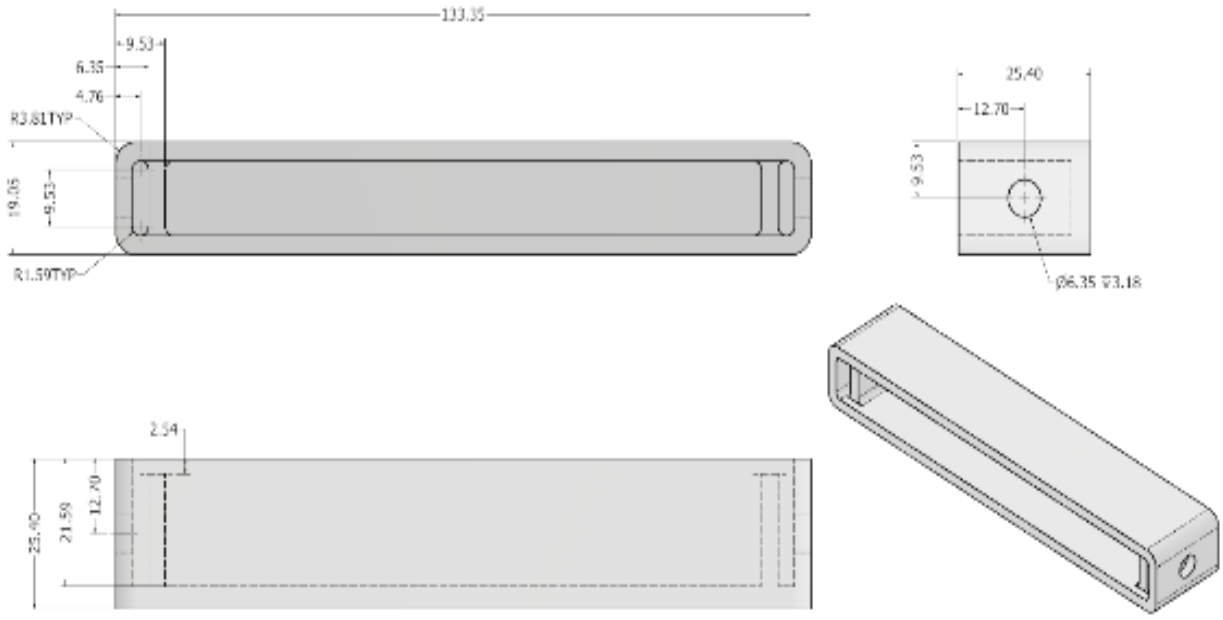

Figure 2-6 Schematic of the Teflon boat design, with dimensions in mm. This figure was taken from the supporting information in Kregel et al 2023 and is also shown in Chapter 3

Due to the size of the headspace and running experiments at atmospheric pressure, not all N_2O_5 molecules will react with the solution. We determined this by comparing the residence time over the solution in the boat to the expected time for a molecule to diffuse from the top of the headspace to the solution surface. A quick equation to calculate this is:

$$x^2 = 2Dt \qquad \text{E2.1}$$

where x is the distance, D is the diffusion constant (0.1 $cm^2\ s^{-1}$ for N_2O_5 in N_2 at room pressure), and t is the time. Using the height of the headspace as the diffusing distance (0.78 cm), we calculate a time to diffuse = 3.1 s, nearly an order of magnitude slower than our residence time.

This indicates many N_2O_5 molecules are not able to diffuse to the solution surface during the expected residence time.

The temperature of the flow reactor is controlled by refrigerated/heated bath circulator (Fisher Scientific Isotemp 3016), containing a water-ethylene glycol mixture. Controlling the temperature is important to maintain a constant humidity in the IMR, as our experiments rely on the evaporation of D_2O from solution to add water vapor in the IMR. In our experiments for the temperature dependence of $ClNO_2$ production (detailed in Chapter 3), we measured the signal counts of I^-, $I(D_2O)^-$, and $I(D_2O)_2^-$. The signal ratios are a marker for the relative humidity in the IMR, and $I(D_2O)^-$ and $I(D_2O)_2^-$ are necessary species to detect N_2O_5 and $ClNO_2$ as $I(N_2O_5)^-$ and $I(ClNO_2)^-$, discussed more in a later section. As the only source of D_2O is from the solutions in the reactor boats, the evaporation of D_2O (which changes with temperature) will affect the sensitivity of signals in the instrument. Maintaining a constant temperature is important for constant sensitivity in the IMR as an experiment progresses.

The gas flows for the reactor and the instrument are controlled through LabVIEW. Previous iterations of this file were designed by prior group members, but the most recent version was created by Steven Kregel. He added the switching valve functionality to the program, allowing for experiments with automated switching of the N_2O_5 flow between two solutions in the flow reactor. The switching values are solenoid valves, powered by a Data Acquisition device running the LabVIEW code. To determine how long the instrument is sampling each boat, the LabVIEW code has sections for “Equilibrium time” and “Sample time”. “Equilibrium time” refers to an initial period just after the valve switches to the other boat, and “Sample time” is the continued measurement over the same boat. The purpose of the equilibrium time is to allow for any variations in the signals of species to reach a steady state. The total time

of data collection over each boat for a single pass depends on the number of data points you measure for “equilibrium time” and “sample time”, as well as the number of species you are recording. The instrument will scan each specified mass you input to the LabVIEW, and output the data for all species at the same time point. This repeats until the system switches.

2.3.1 Calculation for Inability to Measure Uptake

N_2O_5 is a tricky molecule to measure the reactive uptake coefficient. The relative high uptake value, 0.03, means we need to account for gas phase diffusion limitations. Alina Dao provided a simple equation to determine the correction factor in an experimental system to be able to determine the actual uptake coefficient in an experiment.[10]

$$\frac{1}{\gamma_{obs}} = \frac{1}{\gamma_{true}} + \frac{1}{\beta} \qquad \text{E2.2}$$

Where,

$$\beta = \frac{4*D}{v*z} \qquad \text{E2.3}$$

γ_{obs} is the observed uptake coefficient of your species, γ_{true} is the actual uptake coefficient, D is the gas phase diffusion of your reaction species, v is the gas speed, and z is a distance above the surface, generally you should use the height of the headspace of your vessel. Calculating β for N_2O_5 at atmospheric pressure (D = 0.1 cm^2/s, v = ~24000 cm/s, z = 0.8 for headspace height), β = 2.1 $x10^{-5}$. Assuming γ_{true} = 0.03, then γ_{obs} would have to be 2.1 $x10^{-5}$. So not only would this be a very tiny uptake value to measure (21 out of 1 million molecules are irreversibly lost to reaction with solution), but the gas phase diffusion is a significantly larger effect than the actual uptake at the surface. To be able to measure the uptake of N_2O_5, we would have needed to find a way to increase the diffusion coefficient (a lower operating pressure) or

run an experiment with a smaller expected uptake. We decided to focus our experiments on the products from N_2O_5 reacting with solution rather than the amount of N_2O_5 lost.

2.4 Iodomethane for CIMS use

Our mass spectrometer relies on chemical ionization to detect our primary species of interest, N_2O_5 and $ClNO_2$. Chemical ionization provides certain factors that make it useful for our experiments. It is a "soft" form of ionization with little fragmentation and a variety of different adduct species are available to detect certain species, such as benzene cations to measure isoprene and other organics and sulfur hexafluoride anions to detect HNO_3 and sulfur dioxide.[11,12] For our purposes, the ion adduct we use is iodide, I^-, which comes from iodomethane, or methyl iodide (CH_3I).

CH_3I is a volatile halocarbon species used in chemical ionization. When exposed to an ionization source, such as Po-210 in our experimental system, it undergoes radiolysis to form I^-. This adduct is commonly used to detect N_2O_5 in lab experiments and field measurements[13,14]. Interestingly, I^- can be used to detect N_2O_5 in two different forms, as the bound $I(N_2O_5)^-$ species or as a NO_3^- in R2.5[14]

$$I^- + N_2O_5 \rightarrow INO_2 + NO_3^- \qquad \text{R2.5}$$

However, our system is set up with weak declustering, which means we detect the $I(N_2O_5)^-$ species in the instrument, as our voltage settings are not strong enough to break apart the adduct. More information on the voltages is presented in section 2.5. While I^- is the primary reagent ion in the system, we do not use it to directly detect N_2O_5. Instead, we detect N_2O_5 with water clusters of I^-, $I^-(H_2O)_n$ or $I^-(D_2O)_n$, with the following reactions.

$$I^- + D_2O \rightarrow I(D_2O)^- \qquad \text{R2.6}$$

$I^- + 2D_2O \rightarrow I(D_2O)_2^-$ R2.7

$I(D_2O)^- + N_2O_5 \rightarrow I(N_2O_5)^- + D_2O$ R2.8

$I(D_2O)_2^- + N_2O_5 \rightarrow I(N_2O_5)^- + 2D_2O$ R2.9

As discussed earlier, the relative humidity in the IMR can have significant impacts on the sensitivity of the $I(N_2O_5)^-$ signal. Liu et al. found a maximum sensitivity of N_2O_5 signal in a CIMS at ~40% relative humidity, with the sensitivity decreasing at both extremes of high humidity and very low humidity.[15] A constant I^-, $I(D_2O)$, and $I(D_2O)_2^-$ cluster ratio avoids the hassle of accounting for different sensitivities. Since these reactions involve multiple gas phase collisions of species, the pressure in the IMR has a strong effect on the amount of $I(N_2O_5)^-$ formed.

To add I^- into the IMR, our experimental system uses a permeation tube filled with CH_3I and a steady N_2 flow set by a mass-flow controller to bring CH_3I into the Po-210 ionization source, an alpha particle emitter. The amount of CH_3I permeation through the tube is affected by temperature, so daily fluctuations in the laboratory temperature would affect the evaporation of CH_3I; however, I have not noticed any significant variation in the amount of I^- detected in the instrument. While performing a calibration on the permeation tube to determine the rate of permeation would be useful information, CH_3I is a hazardous chemical, so I wanted to avoid exposure of CH_3I as much as possible. As a result, I have not calibrated the permeation tube. Despite this, the amount of CH_3I appeared quite constant overtime, only decreasing significantly when the permeation tube itself appeared empty and dry. The decay of the Po-210 ionization source has a more significant impact on the signal over a several months, with a half-life of 138 days, meaning it needs replacement at least once a year.

CH_3I can degrade over time, especially when exposed to light in the laboratory. The instrumental setup previously has heating tape wrapped around the glass container holding the CH_3I, which acted as a light barrier. Without protection from light, the degradation becomes visible over time (turns somewhat brown/red, likely due to the purple color of I_2 being formed).

2.5 Instrument Details and Maintenance

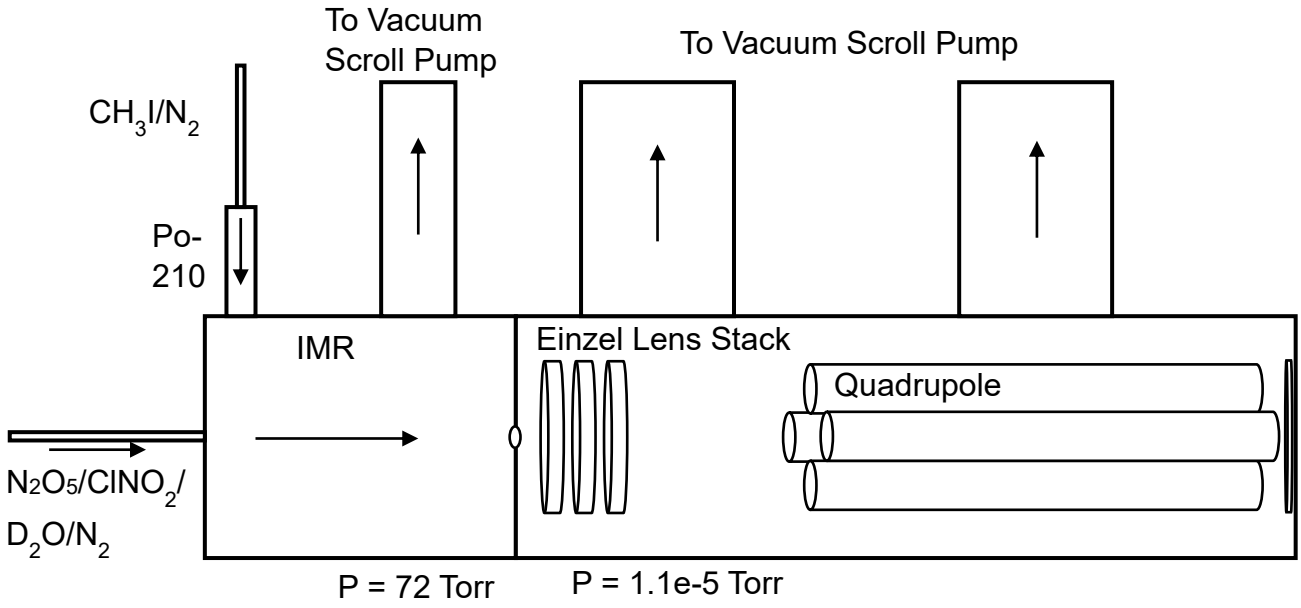

Figure 2-7. Cartoon schematic of Chemical Ionization Mass Spectrometer (CIMS) used for experiments. Pressures for the ion-molecule reactor (IMR) and main quadrupole chamber are given at approximate values used during experiments.

Figure 2.7 is a cartoon schematic of the various components in the mass spectrometer instrument used for experiments. The gases from the dual channel flow reactor, containing N_2O_5, $ClNO_2$, and D_2O, are mixed with the I^- gas flow from the ionizer. The usual operating pressures I run my experiments at are with the IMR at 72 Torr and the Quad chamber at 1.1e-5 Torr. While a higher pressure in the IMR should improve our signal, this would also increase the pressure in the Quad chamber. The maximum safe operating pressure in the Quad chamber is 3×10^{-5} Torr,

per the safety information from Extrel. Running above this pressure can cause damage to the instrument, so we ensure the pressure in the Quad region remains safely below this maximum.

The pressure ratio (IMR/Quad = 6500000) is a good marker to note if there are issues in the vacuum system. If the pressure ratio is higher than expected, where the Quad chamber pressure is lower than expected with IMR = 72 Torr, that may suggest there is a partial blockage of the aperture separating the regions. If the Quad chamber pressure is higher than expected, that would suggest a leak allowing additional gas flow in or the turbo fans and scroll pumps are not operating properly. Common places to check for leaks would be at flanges where two pieces of the instrument are held together. When the system is not in active use for an experiment and there are no flows going through the input or the Po-210 source, then the resting pressures are generally 30-50 mTorr in the IMR region and ~4-5 $x10^{-7}$ Torr for the Quad region.

Over time, we have seen the resting pressures for the IMR and Quad region reach a higher value, even seeing over 200 mTorr in the IMR region despite no flow inputs. The cause of this is usually from the tip seals on the scroll pumps wearing out. This instrument has an SH-110 pump pulling a vacuum on the IMR region and a TS300 scroll pump pulling a vacuum on the Quad region. The tip seals are important for the scroll pumps to properly function, and over time, they wear down and lower the effectiveness of the pumps. To replace the tip seals, a tip seal replacement kit can be purchased online. The actual replacement can be done on a lab bench or the machine shop in the basement can perform it. A manual in the laboratory explains the tip seal replacement process. The process involves opening the scroll pump up to remove the old tip seals, cleaning the orbiting plates of dust and material stuck to the metal, and putting new tip seals in.

2.5.1 Controlling Signal and Troubleshooting

This section focuses on ways to alter the magnitude of the signal detected in the instrument as well as potential causes of measuring low or non-existent signal in the system. As discussed previously, the amount of D_2O vapor and pressure in the IMR has strong impacts on the detected signals for N_2O_5 and $ClNO_2$. Changing these values, such as by warming or cooling the dual channel flow reactor to evaporate different amounts D_2O, would impact the magnitude of your signal. The other way to change the signal is to make changes to the values on the electronics box above the instrument. This box has seven active outputs, which control the voltage gradient across the IMR, the Einzel lens stack, and the backing plate for the quadrupole. With seven voltages, though, it is quite difficult to optimize the signal and it is very easy to go a few volts too far and completely kill the signal. To change the shape of the peaks, there is a knob behind the front panel of one of the quadrupole control boxes which controls the resolution. This knob is sensitive so a small change will have a significant impact on the quad signal. The current setting on the system allows for unit mass resolution, so we can distinguish peaks one m/Q apart. This was necessary to ensure we could distinguish our isotopically labelled species in Chapter 4.

If the signal is lower than expected but still noticeable, then the issue is likely in the process of transporting ions to the Quad chamber. As a reference, I see around 120,000 – 160,000 counts of I^- when I am flowing 3 LPM of N_2 through the CH_3I source and carrier N_2 is flowing through the boat system. If the ion count is lower than this, there are a few things to check. Ensure the pressure in the IMR is at the expected operating pressure (I ran ~72 Torr in IMR). Make sure there is sufficient flow of N_2 through the CH_3I source and that the valve is open to allow the flow into the IMR.

Sometimes, the signal is a flat line, with occasional spikes for a single point, which is likely caused by random noise. The simplest cause of a flat signal line is the researcher forgetting a certain step in turning on the instrument. I find I often forget to turn on the electronics box above the instrument. Other causes could be no gas from the IMR is getting into the quad chamber. The check for this would be to see if the pressures are at their expected levels. Running at a low IMR pressure will result in fewer ions, though you likely would still see ions present. If the pressures are not as expected, such as a low Quad pressure relative to the IMR pressure, then there may be a blockage in the aperture connecting the two regions. You would need to shut the instrument and turbos down, open up the IMR region, and blow compressed air to remove any blockage.

The other major cause for a flatline signal seemed to be the one of the Quad power controller boxes not registering the proper signal to run the instrument. Usually, this is denoted by one or both of the red LED lights lit up. Our lab has binders with information on Extrel system, and they contain some information on troubleshooting. However, not all of their solutions are easy to correlate to our system. I will include a couple of examples of troubleshooting I encountered specific to our system.

The primary reason for the red failure LED light and flatline signal is effectively the box not being able to tell the Quad what to do. One cause is that the Quad chamber pressure relay has been tripped. The pressure gauge on the Quad chamber has a relay test which communicates with the instrument. This is set at a maximum pressure of 2×10^{-5} Torr; if the pressure in the chamber goes above this limit, the relay is tripped and stops the instrument from running. If the instrument were ran at too high a pressure in the Quad region, the amount of ions present could allow for an arc between the poles and potentially damage the instrument. To reset the relay, you go to the

menu of the pressure gauge: *Menu / Setup IG / Relay 1 Test* and set to On. There should be an audible click and the LED light going off if this was the cause of the flatline signal.

Another cause can be that the box is not receiving a signal to control the Quad. This can happen if the whole system has been unpowered for some time, such as from moving the instrument or maintenance on a scroll pump. This seems to be solved by running the Labview file and starting a scan, which provides a signal to the box. If this does fix the error, another potential problem is the cable connecting the DAQ running the Labview and the box. The connection is two wires braided together, connected to "Mass Command" on the box. The connection on the Quad box end seems a little loose, so wiggling these wires can bring back the connection and fix the error.

2.6 Preparation and Cleanliness of Solutions

As the reaction between gaseous N_2O_5 and an aqueous solution is heterogeneous, the nature of the surface has significant impacts on the rates and pathways for reaction. N_2O_5 uptake is reduced by organic films[16,17], and some surfactants can draw up or reduce anions at the surface[18,19]. For our experiments, ensuring a clean chemical environment free from as much potential contamination as possible was essential.

To maintain the cleanliness of our glassware and Teflon solution boats, these items were cleaned through a process involving sulfuric acid (H_2SO_4). The glassware and boats were placed in a bath containing 95-98% H_2SO_4 and allowed to sit for 10-20 minutes. The low pH (pka = -2.8) should react with and dissolve most organic species. After sitting in H_2SO_4, the glassware and Teflon boats are rinsed several times in milli-Q water, to remove excess H_2SO_4 from the containers. The milli-Q is replaced at least once during the rinse process to ensure as much H_2SO_4 is removed. Additionally, we use glass volumetric pipettes in experiments to add solutions

to the Teflon boats. These pipettes are too large to fully submerge in the H_2SO_4 bath, so instead our cleaning procedure involves pulling H_2SO_4 up the pipette, letting sit in the glass for several seconds then emptying. This process is repeated two more times. The pipettes are then rinsed in milli-Q water in a similar fashion, pulling the water up the pipette several times. After rinsing, all glassware and Teflon containers are let to dry overnight. In situations where an item is needed that same day, I flow dry N_2 over and inside the item.

In addition to the containers, the solvent and solutes for the solutions are a potential source for contamination of surfactants. To verify the presence, or lack thereof, of surfactants in solutions, we measured the surface tension of samples with D_2O and NaCl. The change in surface tension upon dissolution of NaCl is known, and the presence of surfactants have been shown to reduce surface tension in water. I measured the surface tension of sample solutions and compared the results with literature to find potential variances in the surface tension suggesting the presence of a surfactant contaminant.

We used a tensiometer with a Wilhelmy plate attachment to measure the surface tension of solutions. The first salt we used in our experiments was NaCl (random crystals, optical grade, 99.9% trace metals basis from Sigma Aldrich). We chose this salt under the assumption that larger crystals and optical grade quality would involve less processing and have a higher volume to surface area ratio compared to ground salt, thus having less potential surfactant contamination. However, our initial surface tension tests found a surface tension increment of -0.1 mN/m, which should not be negative for ionic salts. The literature value for the surface tension increment of NaCl is 1.73 ± 0.17 mN/m.[20] This strongly suggested the presence of a surfactant in the optical grade salt, and so we decided to order granular NaCl from EMD Milipore. A solution using the granular NaCl had a surface tension increment of ~1.6 mN/m, much closer to the literature value,

which gave us the confidence to use this salt for experiments with N_2O_5. It is interesting to note that the granular NaCl salt did not appear to have any surfactant contamination, while the optical grade random crystal NaCl did appear to have some contamination. Certificates of analysis for these salts generally note the composition of trace metals in the salt, but there is no mention of potential organic contaminants. Contacting companies to inquire about the processing procedure for these salts did not yield any information about potential sources of the surface-active contamination found in the optical grade salt. Our assumption is that some species used in machines involved in processing the salt may have contaminated our crystals, but we have no evidence to verify this nor know what exact molecule or molecules may be present.

2.7 Exploratory Experiments

There are several experiments we conducted to better understand the flow reactor; finding potential factors that could impact our results or identifying ways to optimize the signals we measured.

One experiment was to understand the effect of the flow rate through the boats on our signal counts. Changing the flow rate results in dilution of the N_2O_5 concentration over solution, shorter residence time of the gas over solution, and less relative humidity in the IMR. Figure 2.8 shows the $ClNO_2$ signal decreasing at faster flow rates; however, the decrease is not linear or directly proportional to the flow rate. One may expect that tripling the flow rate would mean reducing the amount of N_2O_5 reacting by a factor of three would likewise reduce the amount of $ClNO_2$ by an equivalent amount. However, we only see a factor of two decrease in the $ClNO_2$

signal. I would argue this is due to a better sensitivity for forming $I(ClNO_2)^-$ at lower relative humidities.

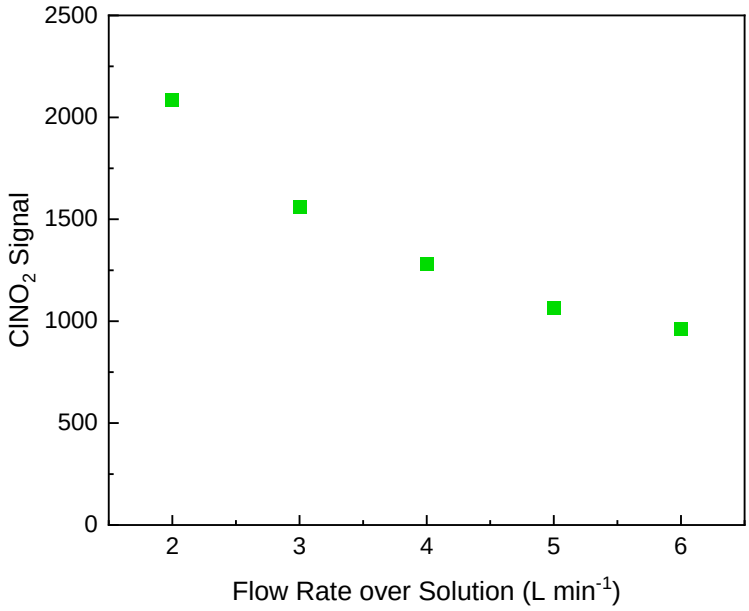

Figure 2-8. Plot of the $ClNO_2$ signal from N_2O_5 flowing over saturated NaCl in D_2O at different flow rates of carrier N_2.

Wall loss to the PFA tubing in our experimental setup can be a significant loss pathway of N_2O_5 and source of HNO_3. Before the boats, the tubes have dry N_2 flowing, so N_2O_5 loss is minimal. However, after the boats when the gas flow has some D_2O vapor, the walls can become slightly wet and allow for significant N_2O_5 hydrolysis. An idea I tested to improve the transmission of was to use a different diameter PFA tube connecting the boats and the instrument. My assumption was that, despite a larger surface to volume ratio with a smaller diameter tube, the shorter residence time in the tube would result in less overall N_2O_5 loss on the walls. Using the MATLAB model described earlier in section 2.2, I predicted the amount of N_2O_5 loss with the different tube sizes. It is important to note that this model is not designed to measure wall loss, as the surface area to volume ratio is meant to emulate dispersed aerosol in the box model. A more accurate model for this test would involve gas phase diffusion near the

wall to account for the location of the wall loss, as in not interspersed. In addition, a narrower tube with a shorter residence time would likely have less water buildup on the walls, thus lowering the uptake coefficient for N_2O_5, which I did not calculate for each scenario. To quickly determine if a different PFA tube size would be more effective, I relied on the initial box model. Table 2.1 shows the different surface area to volume ratios for different tube diameters, ranging from 1/8 to 1/2-inch outer diameter. Using the same uptake coefficient for each size, the model results indicate a narrower tube would result in less N_2O_5 loss.

Table 2.1 Comparison of the surface area to volume ratio, residence time of gas, and modeled N_2O_5 loss for different PFA tube diameters.

Tube Size	Surface Area/Vol Ratio (cm^2/cm^3)	Residence Time for 10 cm tube length (s)	Modeled N_2O_5 Loss (%)
1/8”	24.3	0.0077	27
1/4”	12.1	0.031	45
3/8”	6.90	0.095	65
1/2”	4.35	0.24	81

2.8 References

(1) Bertram, T. H.; Thornton, J. A.; Riedel, T. P. An Experimental Technique for the Direct Measurement of N2O 5 Reactivity on Ambient Particles. *Atmospheric Meas. Tech.* **2009**, *2* (1), 231–242. https://doi.org/10.5194/amt-2-231-2009.

(2) D. W. Fahey, C. S. Eubank, G. Hubler, and F. C. Fehsenfeld. A Calibrated Source of N2O5. *Atmos. Environ.* **1985**, *19* (11), 1883–1890.

(3) Sobyra, T. B.; Pliszka, H.; Bertram, T. H.; Nathanson, G. M. Production of Br2 from N2O5 and Br- in Salty and Surfactant-Coated Water Microjets. *J. Phys. Chem. A* **2019**, *123* (41), 8942–8953. https://doi.org/10.1021/acs.jpca.9b04225.

(4) McNeill, V. F.; Patterson, J.; Wolfe, G. M.; Thornton, J. A. The Effect of Varying Levels of Surfactant on the Reactive Uptake of N2O5 to Aqueous Aerosol. *Atmos Chem Phys* **2006**.

(5) Brown, S. S.; Stutz, J. Nighttime Radical Observations and Chemistry. *Chem. Soc. Rev.* **2012**, *41* (19), 6405. https://doi.org/10.1039/c2cs35181a.

(6) Lee, M. R.; Allen, E. R.; Wolan, J. T.; Hoflund, G. B. NO $_2$ and NO Adsorption Properties of KOH-Treated γ-Alumina. *Ind. Eng. Chem. Res.* **1998**, *37* (8), 3375–3381. https://doi.org/10.1021/ie9801047.

(7) Zhang, W.; Zhang, H. Secondary Ion Chemistry Mediated by Ozone and Acidic Organic Molecules in Iodide-Adduct Chemical Ionization Mass Spectrometry. *Anal. Chem.* **2021**, *93* (24), 8595–8602. https://doi.org/10.1021/acs.analchem.1c01486.

(8) Sander, S. P.; Friedl, R. R.; Ravishankara, A. R. Chemical Kinetics and Photochemical Data for Use in Atmospheric Studies Evaluation Number 15.

(9) Knopf, D. A.; Cosman, L. M.; Mousavi, P.; Mokamati, S.; Bertram, A. K. A Novel Flow Reactor for Studying Reactions on Liquid Surfaces Coated by Organic Monolayers: Methods, Validation, and Initial Results. *J. Phys. Chem. A* **2007**, *111* (43), 11021–11032. https://doi.org/10.1021/jp075724c.

(10) Dao, A. K. Probing N2O5 Reactive Uptake in Organic Solvents Using a Flow Reactor and Chemical Ionization Mass Spectrometry.

(11) Iyer, S.; Lopez-Hilfiker, F.; Lee, B. H.; Thornton, J. A.; Kurtén, T. Modeling the Detection of Organic and Inorganic Compounds Using Iodide-Based Chemical Ionization. *J. Phys. Chem. A* **2016**, *120* (4), 576–587. https://doi.org/10.1021/acs.jpca.5b09837.

(12) Huey, L. G. Measurement of Trace Atmospheric Species by Chemical Ionization Mass Spectrometry: Speciation of Reactive Nitrogen and Future Directions. *Mass Spectrom. Rev.* **2007**, *26* (2), 166–184. https://doi.org/10.1002/mas.20118.

(13) Lee, B. H.; Lopez-Hilfiker, F. D.; Mohr, C.; Kurtén, T.; Worsnop, D. R.; Thornton, J. A. An Iodide-Adduct High-Resolution Time-of-Flight Chemical-Ionization Mass Spectrometer: Application to Atmospheric Inorganic and Organic Compounds. *Environ. Sci. Technol.* **2014**, *48* (11), 6309–6317. https://doi.org/10.1021/es500362a.

(14) Lopez-Hilfiker, F. D.; Iyer, S.; Mohr, C.; Lee, B. H.; D'Ambro, E. L.; Kurtén, T.; Thornton, J. A. Constraining the Sensitivity of Iodide Adduct Chemical Ionization Mass Spectrometry to Multifunctional Organic Molecules Using the Collision Limit and Thermodynamic Stability of Iodide Ion Adducts. October 23, 2015. https://doi.org/10.5194/amtd-8-10875-2015.

(15) Liu, Y.; Jia, Y.; Chu, B.; Li, S.; Cao, Q.; Liu, J.; Ma, W.; Li, Y.; Wang, L.; Nie, W.; Ma, Q.; He, H. An Alternative Calibration Method for Measuring N $_2$ O $_5$ with an Iodide-Chemical Ionization Mass Spectrometer and Influencing Factors. *Anal. Chem.* **2024**, *96* (10), 4048–4056. https://doi.org/10.1021/acs.analchem.3c04089.

(16) McDuffie, E. E.; Fibiger, D. L.; Dubé, W. P.; Lopez-Hilfiker, F.; Lee, B. H.; Thornton, J. A.; Shah, V.; Jaeglé, L.; Guo, H.; Weber, R. J.; Michael Reeves, J.; Weinheimer, A. J.; Schroder,

J. C.; Campuzano-Jost, P.; Jimenez, J. L.; Dibb, J. E.; Veres, P.; Ebben, C.; Sparks, T. L.; Wooldridge, P. J.; Cohen, R. C.; Hornbrook, R. S.; Apel, E. C.; Campos, T.; Hall, S. R.; Ullmann, K.; Brown, S. S. Heterogeneous N2O5 Uptake During Winter: Aircraft Measurements During the 2015 WINTER Campaign and Critical Evaluation of Current Parameterizations. *J. Geophys. Res. Atmospheres* **2018**, *123* (8), 4345–4372. https://doi.org/10.1002/2018JD028336.

(17) Ryder, O. S.; Campbell, N. R.; Morris, H.; Forestieri, S.; Ruppel, M. J.; Cappa, C.; Tivanski, A.; Prather, K.; Bertram, T. H. Role of Organic Coatings in Regulating N2O5 Reactive Uptake to Sea Spray Aerosol. *J. Phys. Chem. A* **2015**, *119* (48), 11683–11692. https://doi.org/10.1021/acs.jpca.5b08892.

(18) Zhao, X.; Nathanson, G. M.; Andersson, G. G. Competing Segregation of Br- and Cl- to a Surface Coated with a Cationic Surfactant: Direct Measurements of Ion and Solvent Depth Profiles. *J. Phys. Chem. A* **2020**, *124* (52), 11102–11110. https://doi.org/10.1021/acs.jpca.0c08859.

(19) Gord, J. R.; Zhao, X.; Liu, E.; Bertram, T. H.; Nathanson, G. M. Control of Interfacial Cl2 and N2O5 Reactivity by a Zwitterionic Phospholipid in Comparison with Ionic and Uncharged Surfactants. *J. Phys. Chem. A* **2018**, *122* (32), 6593–6604. https://doi.org/10.1021/acs.jpca.8b04590.

(20) Pegram, L. M.; Record, M. T. Hofmeister Salt Effects on Surface Tension Arise from Partitioning of Anions and Cations between Bulk Water and the Air−Water Interface. *J. Phys. Chem. B* **2007**, *111* (19), 5411–5417. https://doi.org/10.1021/jp070245z.

Chapter 3. Weak Temperature Dependence of the Relative Rates of Chlorination and Hydrolysis of N_2O_5 in NaCl-Water Solutions

Steven J. Kregel,[1] Thomas F. Derrah,[1] Seokjin Moon,[2] David T. Limmer,[2,3,4,5*]

Gilbert M. Nathanson,[1*] and Timothy H. Bertram[1*]

[1] Department of Chemistry, University of Wisconsin-Madison, Madison, WI, 53706, USA

[2] Department of Chemistry, University of California, Berkeley, CA, 94720, USA

[3] Kavli Energy NanoScience Institute, University of California, Berkeley, CA, 94720, USA

[4] Chemical Sciences Division, Lawrence Berkeley National Laboratory, Berkeley, CA, 94720, USA

[5] Material Sciences Division, Lawrence Berkeley National Laboratory, Berkeley, CA, 94720, USA

3.1 Abstract

We have measured the temperature dependence of the $ClNO_2$ product yield in competition with hydrolysis following N_2O_5 uptake to aqueous NaCl solutions. For NaCl-D_2O solutions spanning 0.0054 M to 0.21 M, the $ClNO_2$ product yield decreases on average by only 4 ± 3 % from 5 to 25 ˚C. Less reproducible measurements at 0.54 M and 2.4 M NaCl also fall within this range. The ratio of the rate constants for chlorination and hydrolysis of N_2O_5 in D_2O is determined on average to be 1150 ± 90 at 25 °C up to 0.21 M NaCl, favoring chlorination. This ratio is observed to decrease significantly at the two highest concentrations. An Arrhenius analysis reveals that the activation energy for hydrolysis is just 3.0 ± 1.7 kJ/mol larger than for chlorination up to 0.21 M, indicating that Cl^- and D_2O attack on N_2O_5 have similar energetic barriers despite the differences in charge and complexity of these reactants. In combination with the measured pre-exponential ratio favoring chlorination of $300\ ^{+400}_{-200}$, we conclude that the

strong preference of N_2O_5 to undergo chlorination over hydrolysis is driven by dynamic and entropic, rather than enthalpic, factors. Molecular dynamics simulations elucidate the distinct solvation between strongly hydrated Cl^- and the hydrophobically solvated N_2O_5. Combining this molecular picture with the Arrhenius analysis implicates the role of water in mediating interactions between such distinctly solvated species and suggests a role for diffusion limitations on the chlorination reaction.

3.2 Introduction

Dinitrogen pentoxide (N_2O_5) is a nocturnal reservoir of NO_x ($NO_x \equiv NO + NO_2$) in the atmosphere. Reactions of N_2O_5 with aqueous aerosol particles comprise a major sink for NO_x, with consequent effects on tropospheric ozone production.[1,2] The heterogeneous uptake of N_2O_5 to aerosol particles can result in hydrolysis to produce NO_3^- and H^+ (R3.1) and chlorination to produce nitryl chloride ($ClNO_2$) in the presence of Cl^- (R3.2):

$$N_2O_5(g) + H_2O \rightarrow 2NO_3^- + 2H^+ \quad \text{R3.1}$$

$$N_2O_5(g) + Cl^- \rightarrow ClNO_2(g) + NO_3^- \quad \text{R3.2}$$

Due to its limited solubility, $ClNO_2$ rapidly evaporates from aerosol particles, where it photolyzes to produce Cl radicals and regenerate NO_2.[3] In urban environments, Cl radicals can efficiently oxidize volatile organic compounds, leading to tropospheric ozone production.[3,4] On a global scale, the efficient removal of NO_x from the reactive uptake of N_2O_5 reduces the atmospheric abundance of O_3 and OH, which in turn extends the lifetime of CH_4.[5] The production of H^+ and NO_3^- from the hydrolysis of N_2O_5 results in acidification and nitrification of aerosols, which has been shown on the regional scale to contribute to particulate matter air quality exceedance events.[6,7]

Previous laboratory experiments have focused on investigating the production of $ClNO_2$ as a function of solution-phase chloride and added ions and surfactants.[8–13] Behnke *et al.* measured the production of $ClNO_2$ over bulk solutions and found that at high chloride concentrations (i.e., $[Cl^-] > 2M$) $ClNO_2$ was the only product observed.[8] Bertram and Thornton developed a parametrization for the total reactive uptake of N_2O_5 as a function of water, nitrate, and chloride concentrations in aqueous aerosols, and found that small concentrations of chloride reversed the inhibition of N_2O_5 reactive uptake induced by high dissolved nitrate concentrations.[9] Their findings confirmed the results of Behnke *et. al.* that $ClNO_2$ is the primary reaction product in the presence of high $[Cl^-]$, and implied that $ClNO_2$ is much less reactive in aerosols than N_2O_5. Roberts *et. al.* investigated the production of $ClNO_2$ at lower concentrations of chloride and determined the ratio of rate constants for the chlorination (k_{Cl^-}) and hydrolysis (k_w) reactions.[11] Due to their large observed rate constant ratio, 450 ± 100, they postulated that the activation energy for hydrolysis is significantly larger than for chlorination, implying that chlorination would be favored at lower temperatures. Further justification comes from a lack of experimental evidence for a systematic dependence of the reactive uptake of N_2O_5 on chloride concentration to within the uncertainty of measurements (which are centered around reaction probabilities between 0.01 and 0.04).[8,14–19] This observation is consistent with the assumption that the rates of N_2O_5 reactions are limited by the dissociation of N_2O_5 into NO_2^+ and NO_3^-, followed by subsequent reaction of NO_2^+ with water or solute anions.[20] Roberts *et. al.* rationalized their proposed temperature dependance on the $ClNO_2$ yield via this mechanism by invoking a barrierless reaction between the oppositely charged NO_2^+ and Cl^- reactants versus a more significant barrier for the ion-neutral reaction of NO_2^+ with H_2O.[11]

However, recent theoretical[21–26] and laboratory[9,16] studies have called into question the existence of isolated aqueous NO_2^+ ions. Bianco and Hynes first proposed concerted hydrolysis involving nucleophilic $OH^{\delta-}$ attack from H_2O on molecular $NO_2^{\delta+}NO_3^{\delta-}$ that has incipient ion-pair character.[21] This suggestion was elaborated by McNamara and Hillier through quantum chemistry calculations of $N_2O_5(H_2O)_n$ that corroborated the intact nature of N_2O_5, both for hydrolysis (n = 0-6) and for Cl^- attack (n = 0-1).[22,27] Using *ab initio* molecular dynamics, Rossich Molina and Gerber further discovered that N_2O_5 may undergo hydrolysis on the surface of an $(H_2O)_{20}$ cluster by either nucleophilic (70%) or electrophilic (30%) attack of $H^{\delta+}OH^{\delta-}$ on $NO_2^{\delta+}NO_3^{\delta-}$.[23] Most recently, Galib and Limmer[24] and separately Cruzeiro, Galib, Limmer, and Götz[25] employed molecular simulations and reaction-diffusion models to explore hydrolysis in the vicinity of an extended liquid-vapor interface. These studies reveal that N_2O_5 undergoes hydrolysis within the top 20 Å of solution, with up to 20% of hydrolysis occurring at the interface itself. The lifetime of $NO_2^{\delta+}$ from dissociating $NO_2^{\delta+}NO_3^{\delta-}$ is found to be on the picosecond timescale as it is attacked by $H^{\delta+}OH^{\delta-}$. Karimova and Gerber have also shown that $NO_2^{\delta+}NO_3^{\delta-}$ in a $(H_2O)_{12}$ complex can undergo S_N2 attack by Cl^- as NO_3^- concertedly departs, a mechanism that is distinct from S_N1 attack on solvent-separated NO_2^+.[10,28]

For this study, we interpret our data within the paradigm of an intact reactive N_2O_5 molecule exhibiting significant ion-pair character, as indicated by the theoretical predictions described above. We may still expect a significant temperature dependence for the competition between R1 and R2 because chlorination requires only bond breaking within N_2O_5 and involves an anion approaching a charge-fluctuating molecule. In contrast, hydrolysis involves concerted bond breaking in both H_2O and N_2O_5 reactants as density fluctuations bring them together. The much higher rate constant for chlorination over hydrolysis (measured here and in refs[8,9,11,12,15])

may arise from a larger energetic barrier for this dual bond breaking pathway between overall neutral reactants.

This study addresses the nature of R3.1 and R3.2 by directly measuring the competition between hydrolysis and chlorination over temperatures from 5 to 25 °C at chloride concentrations from 0.0054 to 2.4 M NaCl. This temperature span was chosen to reflect the conditions present in the lower troposphere where the majority of N_2O_5 heterogeneous uptake occurs, and the concentration range was chosen to provide $ClNO_2$ product yields ranging from a few percent to nearly complete conversion to $ClNO_2$, as shown in previous studies.[8,11–13] The key quantity that we measure is the $ClNO_2$ product yield, or branching between R1 and R2, equal to the fraction of reacting N_2O_5 that produce $ClNO_2$. To our surprise, we measure only a small temperature dependence, suggesting that a single set of temperature independent $ClNO_2$ product yields may suffice in atmospheric modeling of hydrolysis and chlorination. An Arrhenius analysis enables us to further explore the fundamental competition between solute-solute and solute-solvent reactions, in this case involving solute Cl^- and solvent water attack on N_2O_5. This analysis reveals that the activation energy for hydrolysis is only 3.0 ± 1.7 kJ/mol higher than for chlorination. This small activation energy (equal to 1.2 *RT* at 25 °C) implies that the larger rate constant for chlorination over hydrolysis is not driven enthalpically, but rather through a combination of entropic and dynamic effects. With molecular simulations, we can quantify changes in solvent water coordination as the ionic and neutral reactants find each other in solution and use these calculations with diffusion-limited kinetic theory to gain insight into the chlorination rate.

3.3 Experimental Procedure

The product yields of $ClNO_2$ following reactive uptake of N_2O_5 to NaCl solutions with concentrations of 0.0054, 0.014, 0.026, 0.055, 0.099, 0.21, 0.54, and 2.4 M were measured at 5, 10, 15, 20, and 25 °C using an approach based on Roberts *et. al.*[11] and Staudt *et. al.*[13] In our experiments, N_2O_5 was alternately flowed over one of two aqueous solutions at the same temperature but with differing chloride concentrations. The reference solution was saturated with NaCl (~6.1 M) while the chloride concentration of the sample solution was systematically varied. $ClNO_2$ formed from the reactive uptake of N_2O_5 to the chloride solutions was detected using chemical ionization mass spectrometry (CIMS) with a quadrupole mass analyzer and an ion source utilizing iodide anion cluster chemistry.[29] We note that this experiment is unable to measure the absolute uptake of N_2O_5 into solution due to gas-phase diffusion limitations at atmospheric pressure; only product yields (and thus relative reaction rates for R3.1 and R3.2) can be determined. In the following sections we describe our experimental setup, the preparation of NaCl solutions, and our method for determining the $ClNO_2$ product yield.

3.3.1 Experimental Setup and Method

A schematic of the flow reactor and gas flow path is shown in Figure 1. The reactor consists of a milled aluminum block with PTFE solution holder inserts. The aluminum block contains coolant channels which enable thermal control via a recirculating chiller. The solution holders are each milled out of single pieces of PTFE and include a PTFE lid, embedded in the aluminum lid of the reactor. In combination with PFA tubing, these pieces ensure that the entire flow path is minimally reactive towards N_2O_5.

The solution holders each measure 130 mm × 19 mm × 25 mm and can hold a maximum solution volume of 27.5 mL. A 6.5 mm hole at either end of the solution holder enables the passage of gas through the headspace above the solution. For the 20 mL solutions used in this

study, the total headspace volume above each solution was ~11 mL and the solution surface area was 14.5 cm^2.

As shown in Figure 3-1, dry N_2 is continually flowed over each solution at a rate of 1 liter

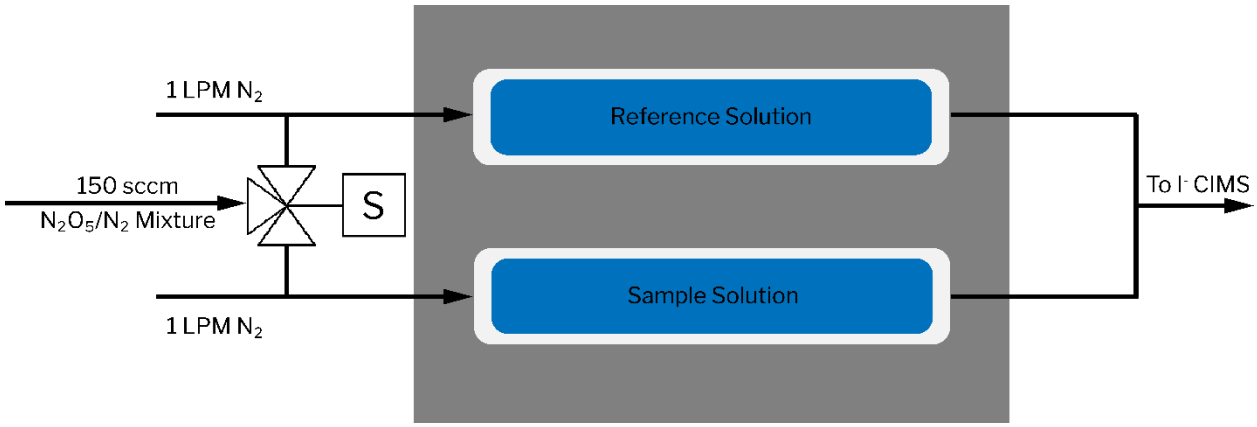

Figure 3-1 The flow path used in these experiments. The solenoid switching valve is computer controlled and all tubing is constructed of entirely inert materials.

per minute, while a computer-controlled solenoid valve controls the flow of the $N_2O_5/NO_2/O_3/N_2$ mixture into the system. This PTFE valve directs a 150 standard cubic centimeter per minute (sccm) stream of N_2O_5 in N_2 into the carrier flow passing over either the sample or reference solution. Depending on the exact parameters of the N_2O_5 generation system, the concentration of N_2O_5 ranged from 100-150 ppb, but remained constant over the course of a single experiment. After passing over the solutions, the two carrier flows were recombined and sampled together by a chemical ionization mass spectrometer. We found it necessary to continuously maintain the carrier flow over each solution to prevent condensation on the dry walls of the solution holders, especially at lower temperatures.

The chemical ionization quadrupole mass spectrometer was operated in negative ion mode and utilized iodide cluster chemistry for the selective detection of $ClNO_2$ and N_2O_5 as the iodide adducts $I(ClNO_2)^-$ (*m/Q* of 207.87 Th) and $I(N_2O_5)^-$ (*m/Q* of 234.89 Th).[29] These iodide adducts require the formation of $I(H_2O)_n^-$ clusters to form $I(ClNO_2)^-$ and $I(N_2O_5)^-$ via gas-phase

ligand exchange reactions. We chose to use a weak electric field in the source region of the mass spectrometer to maximize the sensitivity to the iodide adduct analytes. However, this choice resulted in the efficient transmission of the $I(HNO_3 \cdot H_2O)^-$ (*m/Q* of 207.91 Th) cluster ion, which was not resolvable from $I(^{35}ClNO_2)^-$ (*m/Q* of 207.87 Th) by the quadrupole mass filter. To overcome this overlap, we used D_2O in place of H_2O for the reference and sample solutions, which moved the $I(HNO_3 \cdot H_2O)^-$ peak to $I(DNO_3 \cdot D_2O)^-$ (*m/Q* of 210.92 Th). Tests described later indicate that the product yield increases slightly when substituting D_2O for H_2O. We note that our signals are too weak to confidently monitor the $I(^{37}ClNO_2)^-$ isotope at low chloride concentrations.

It is well known that the sensitivity of iodide CIMS to various molecules can depend strongly on the absolute humidity within the ion molecule reactor.[30] In our experiments the absolute humidity in the ion-molecule reaction region (IMR) is determined by D_2O evaporation from the sample and reference solutions. The symmetric nature of our experimental setup ensured that the absolute humidity in the IMR was independent of the flow path of N_2O_5 and remained constant over the course of an experiment. We tested this assumption by filling both the sample and reference solution holders with a saturated NaCl solution and monitoring the $I(N_2O_5)^-$ and $I(ClNO_2)^-$ yields. In this configuration we observed a difference of less than 2% for $ClNO_2$, indicating that the sensitivity of the iodide CIMS was independent of the path taken by the N_2O_5.

3.3.2 Equipment Cleaning and Solution Preparation

To minimize the effects of any surfactant contaminants on our product yield measurements, all glassware and the PTFE solution holders were cleaned by immersion in concentrated H_2SO_4 for at least 30 minutes to dissolve residual surfactants and rinsed twice with

ultrapure water to remove residual sulfate, which has also been shown to affect the $ClNO_2$ yield.[13] Importantly, the addition of NaCl raised the surface tension of each solution, as expected in the absence of surfactants. Surface tension measurements of the 0.21, 0.54, and 2.4 M NaCl solutions yielded an average surface tension increment of 2.0 mN/m per molal in D_2O, similar to the 1.7 ± 0.2 mM/m per molal literature values in H_2O.[31] Following the sulfuric acid cleaning procedure, we prepared solutions of NaCl (EMD Millipore Corp. ACS Reagent Grade) in D_2O (Sigma Aldrich, 99% D-atom) with concentrations of 0.0054, 0.014, 0.026, 0.055, 0.099, 0.21, 0.54, 2.4, and 6.1 M (saturated reference) in 25 mL volumetric flasks.

3.3.3 N_2O_5 Synthesis

N_2O_5 was generated in situ following the procedure described in Bertram et al.[32] Ultrapure zero air and ultrahigh purity nitrogen, each dried by passing the gas streams through potassium hydroxide traps, were mixed prior to illumination by a low-pressure mercury pen lamp (Jelight 95-2100-1), generating a stable concentration of ozone (O_3). The $N_2/O_2/O_3$ flow was then mixed with NO_2 delivered from a cylinder containing 50 ppm NO_2 in a balance of N_2. The gas mixture was subsequently mixed in a dark glass reaction cell for approximately 100 s. The resulting O_3, NO_2, NO_3, and N_2O_5 concentrations in the 150 sccm flow were estimated to be 360, 2700, 0.1, and 130 ppb, respectively, based on measurements of changes in the O_3 concentration as in Bertram et al.[32]

3.3.4 Data Acquisition

In a typical experiment, each solution holder was filled with either a sample or reference solution and loaded into the reactor block. The reactor was then cooled to 5 °C with a recirculating chiller, and the temperature of the solutions was assumed to be equilibrated with the reactor block when the signals from the $I(D_2O)^-$ and $I(D_2O)_2^-$ cluster ions had stabilized. N_2O_5

was then passed over the NaCl solutions, with the flow alternating between the sample and reference solutions approximately every two minutes. To determine the $ClNO_2$ production from the sample and reference solutions, the N_2O_5 flow was alternated at least 5 times for each temperature point. The temperature of the chiller was then increased and the signal intensities of the $I(D_2O)^-$ and $I(D_2O)_2^-$ cluster ions were monitored for temperature equilibration. Three experiments were performed for each NaCl sample concentration at temperatures of 5, 10, 15, 20, and 25 °C. Due to the larger range in $ClNO_2$ product yields determined for the first three experiments with the 2.4 M NaCl sample solution, a fourth experiment was performed only for this concentration.

3.3.5 Determination of Product Yield

The $ClNO_2$ product yield (Φ) is defined as the amount of $ClNO_2$ produced relative to the total amount of N_2O_5 lost by all reactions:

$$ClNO_2 \text{ Product Yield } (\Phi) = \frac{\Delta[ClNO_2]}{\Delta[N_2O_5]} = \frac{[ClNO_2]_{final}}{|[N_2O_5]_{initial} - [N_2O_5]_{final}|} \quad \text{E3.1}$$

where $\Delta[ClNO_2]$ and $\Delta[N_2O_5]$ are the differences in the gas phase concentrations of $ClNO_2$ and N_2O_5 before (initial) and after (final) exposure to the NaCl solution. Equation 3.1 assumes that there is no $ClNO_2$ in the incident gas stream. As in previous studies, we also assume that the $ClNO_2$ product yield from the saturated NaCl reference solution is 1 (i.e. all reacting N_2O_5 are converted into $ClNO_2$).[13,33] This means that

$$\Phi \equiv 1 = \frac{\beta\, S_{ClNO_2}(\text{Reference})}{\Delta[N_2O_5](\text{Reference})} \quad \text{E3.2}$$

and thus

$$\Delta[N_2O_5](\text{Reference}) = \beta\, S_{ClNO_2}(\text{Reference}) \quad \text{E3.3}$$

where S_{ClNO_2} is the $ClNO_2$ signal from the reference solution as measured by the mass spectrometer and β is the instrumental sensitivity factor. In the same way, $\Delta[ClNO_2] = \beta\, S_{\mathrm{ClNO_2}}(\mathrm{Sample})$. In our experiment, we assume that β is the same for the reference and sample conditions as the absolute humidity is the same. At atmospheric pressure, gas-phase diffusive transport of N_2O_5 to the liquid controls the loss rate of N_2O_5 to the solution and we are not sensitive to changes in the reactive uptake coefficient at the surface. As a result, we can assume that $\Delta[N_2O_5]$ over both the sample and reference solutions are identical. These assumptions lead to the equality

$$\Delta[\mathrm{N_2O_5}](\mathrm{Reference}) = \Delta[\mathrm{N_2O_5}](\mathrm{Sample}) \qquad \text{E3.4}$$

and the product yield expression

$$\Phi = \frac{\Delta[\mathrm{ClNO_2}](\mathrm{Sample})}{\Delta[\mathrm{N_2O_5}](\mathrm{Sample})} = \frac{\Delta[\mathrm{ClNO_2}](\mathrm{Sample})}{\Delta[\mathrm{N_2O_5}](\mathrm{Reference})} = \frac{\mathrm{S_{ClNO_2}(Sample)}}{\mathrm{S_{ClNO_2}(Reference)}} \qquad \text{E3.5}$$

This final expression states that the $ClNO_2$ product yield can simply be computed from the ratio of the $ClNO_2$ signals detected by the mass spectrometer from the sample and reference gas streams. This method reduces the dependence of the retrieved $ClNO_2$ product yield on N_2O_5 loss in the transfer tubing that connects the reactor with the CIMS, which can be a significant fraction of the total N_2O_5 loss. Additionally, while the production rate of N_2O_5 on a given day was very stable, day-to-day variations of up to 50% were observed due to subtle changes in the gas flow rates used to generate the 150 sccm N_2O_5 stream. These day-to-day variations in incipient N_2O_5 concentrations resulted in variable $ClNO_2$ production from our aqueous solutions. We accounted for these variations by treating the saturated reference solution as an internal standard, thus removing the impact of gas phase N_2O_5 concentrations on our measurements. Also, embedded in

our analysis are the assumptions that $ClNO_2$ is produced only over the solutions and that $ClNO_2$ does not undergo hydrolysis on the tubing walls.[13,34]

Data from a typical experiment is shown in Figure 3.2. As expected, the $ClNO_2$ yield is very responsive to the solution phase chloride concentration, with the reference solution producing more $ClNO_2$ than the 0.0054 M sample solution. An analysis of this data at different temperatures and NaCl concentrations is presented below.

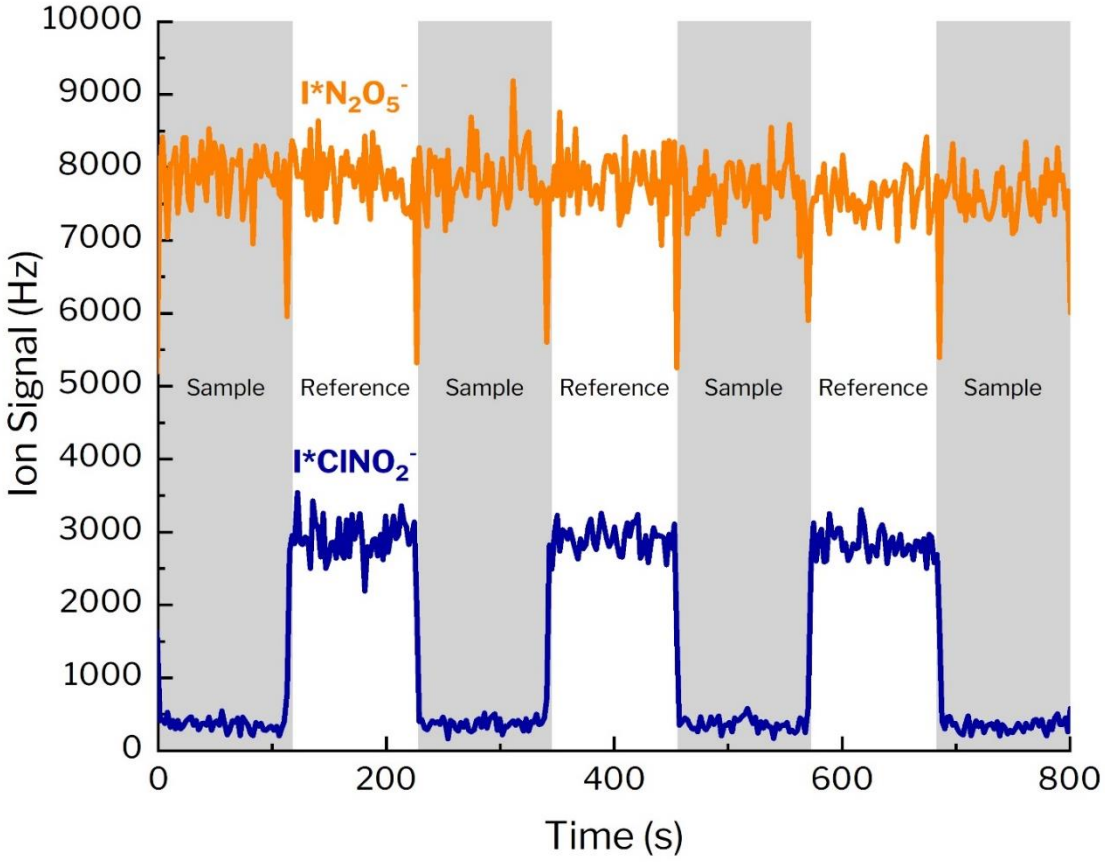

Figure 3-2 Representative experimental data showing the CIMS $ClNO_2$ signal (S_{ClNO2}, detected as $I(ClNO_2)^-$, blue line) and the CIMS N_2O_5 signal (detected as $I(N_2O_5)^-$, orange line) when sampling from the flow reactor in the reference (non-shaded regions) and sample (shaded regions) solutions for sample $[Cl^-]$ = 0.0054 M at 15 °C. The sharp dips in the N_2O_5 signal are due to the switching time of the solenoid valve and last no more than 1 s. Note the long-term stability of the N_2O_5 signal, which indicates both stable production of N_2O_5 during an experiment and equal loss between the sample and reference paths.

3.4 Results and Discussion

In this section we describe the results of our investigation, including the temperature dependent measurements of the $ClNO_2$ product yield and the effects of our use of D_2O solvent. We also carried out an Arrhenius analysis to determine the difference in activation energies between hydrolysis and chlorination and the ratio of pre-exponential factors for the two reactions.

3.4.1 Measurement of $ClNO_2$ Product Yield.

Figure 3.3 shows the $ClNO_2$ product yield (Φ) calculated from eq E3.5 as a function of temperature from 5 to 25 °C for NaCl solutions between 0.0054 and 2.4 M. The product yield increases significantly with increasing Cl^- concentration, as expected from previous studies,[8,9,12,13,35] while the dependence on temperature is much less apparent. Table 1 lists the values of Φ at 5 and 25 °C, and data for all temperatures is included in Table S1 in the Supporting Information (SI). These results indicate that chloride concentration has a much larger impact on Φ than does temperature over the temperature and chloride concentrations used in this study.

As quantified below, Figure 3.3 shows that the $ClNO_2$ product yields decrease slightly with increasing temperature at lower Cl^- concentrations (≤ 0.21 M), while the 0.54 and 2.4 M solutions deviate from this behavior. Noticeably, the spread in the measured $ClNO_2$ product yield for these two higher concentration solutions increases significantly with increasing temperature. While collecting the data in Figure 3, it was necessary to replace the 50 ppm NO_2/N_2 cylinder and following this replacement it was noted the new measured concentration of DNO_3 was approximately 40% of the DNO_3 present with the original NO_2/N_2 cylinder, while the N_2O_5 concentration was unchanged. Interestingly, the measured $ClNO_2$ product yields for the 0.54 and 2.4 M solutions prior to the cylinder change (circles and squares in Figure 3.3) and those

following the change (upward and downward triangles) exhibit different behaviors at higher temperatures. Due to the intricate interdependencies of the chemistries present within the ion-molecule reactor,[36] we hypothesize that the decrease in DNO_3 afforded by the replacement NO_2/N_2 tank, in combination with the increased absolute humidity at higher temperatures, resulted in a small differential sensitivity of the iodide CIMS to $ClNO_2$ for these solutions. This differential sensitivity resulted in large variations of the data obtained during different

experiments, and for this reason we have removed the data from the 0.54 and 2.4 M solutions from our analysis.

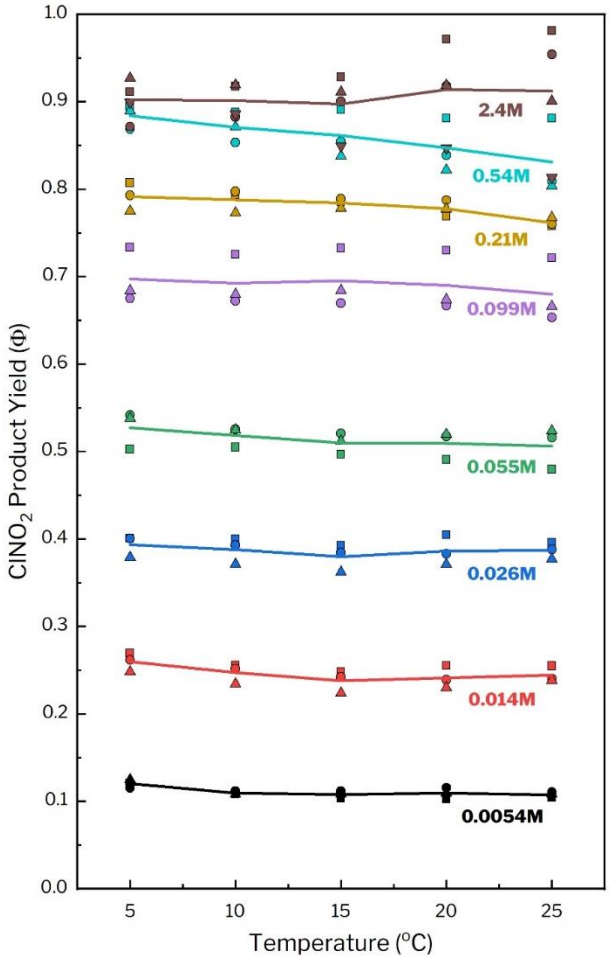

Figure 3-3 The product yield of $ClNO_2$ was measured for NaCl solutions in D_2O between 0.0054 M and 2.4 M and from 5 to 25 °C in 5-degree intervals. The different symbols represent the product yield calculated from each individual data acquisition run. Solid lines connect the means of the individual product yields for each NaCl concentration at each temperature point.

3.4.2 Analysis of Competitive Hydrolysis and Chlorination.

Beyond the importance of $ClNO_2$ formation in the atmosphere, the hydrolysis and chlorination reactions R3.1 and R3.2 represent a fundamentally interesting class of competitive reactions, in that one of the reacting molecules is solvent water and the other is a solute chloride

ion. We first consider whether hydrolysis and chlorination are under kinetic or thermodynamic control, based on experimental trends and the thermochemistry of each reaction:[37]

$$N_2O_5(g) + H_2O(l) \rightarrow 2NO_3^-(aq) + 2H^+(aq)$$

$$\Delta H° = -142\,\frac{kJ}{mol} \quad \Delta S° = -134\,\frac{J}{mol\,K} \quad \Delta G° = -103\,\frac{kJ}{mol} \quad K_{eq}(25\,°C) = 1\times10^{18}$$

$$N_2O_5(g) + Cl^-(aq) \rightarrow ClNO_2(g) + NO_3^-(aq)$$

$$\Delta H° = -40\,\frac{kJ}{mol} \quad \Delta S° = +10\,\frac{J}{mol\,K} \quad \Delta G° = -43\,\frac{kJ}{mol} \quad K_{eq}(25\,°C) = 3\times10^{7}$$

The ratio of equilibrium constants $K_{eq}(Cl^-)/K_{eq}(H_2O)$ is 3×10^{-11} at 25 °C, in contrast to the observed nearly complete conversion of N_2O_5 into $ClNO_2$ at only 2 M NaCl.[8] The listed enthalpies and entropies also predict a significant temperature dependence, such that $K_{eq}(Cl^-)/K_{eq}(H_2O)$ increases by 17-fold upon cooling from 25 to 5 °C. Our $ClNO_2$ product yields (shown in Figure 3) reveal a much weaker temperature dependence: as seen in the fourth column of Table 1, these yields increase on average by 4 ± 3% (95% confidence interval) as the temperature decreases from 25 to 5 °C for $[Cl^-] \leq 0.21$ M. The thermochemical data and experimental comparisons together imply that hydrolysis and chlorination generate products that are much more stable than the N_2O_5 reactant, and that the highly insoluble $ClNO_2$ rapidly evaporates from solution (with an estimated solubility of only ~0.04 M/atm at 25 ˚C[38]), leading to nearly irreversible reactions for which N_2O_5 reactivity is controlled by the forward rates of R3.1 and R3.2.

We therefore consider the $ClNO_2$ product yield to be governed by the relative forward rates of N_2O_5 chlorination and hydrolysis as elementary reactions. The rate expressions can be written as $R_{Chlorination} = k_{Cl^-}[Cl^-][N_2O_5]$ and $R_{Hydrolysis} = k_w[D_2O][N_2O_5]$, where k_{Cl^-} and

k_w are the bimolecular rate constants for chlorination and hydrolysis. We can then express the $ClNO_2$ product yield for the sample solution as a quotient of reaction rates:

$$\Phi = \frac{\Delta[ClNO_2]}{\Delta[ClNO_2]+\Delta[DNO_3]} = \frac{R_{Chlorination}}{R_{Chlorination}+R_{Hydrolysis}} = \frac{k_{Cl^-}[Cl^-][N_2O_5]}{k_{Cl^-}[Cl^-][N_2O_5] + k_w[D_2O][N_2O_5]} \quad \text{(E3.6)}$$

While we cannot independently determine k_{Cl^-} or k_w, we can compute their ratio by rearranging eq 6 to

$$\frac{k_{Cl^-}}{k_w} = \left(\frac{\Phi}{1-\Phi}\right)\frac{[D_2O]}{[Cl^-]} \quad \text{(E3.7)}$$

Calculated values of $\frac{k_{Cl^-}}{k_w}$ are listed in Table 3.1 at 5 and 25 °C and in Table 3S.2 at all temperatures. The ratio $\frac{k_{Cl^-}}{k_w}$ decreases on average by 9 ± 7 % (last column in Table 3.1) over the 20 °C range for NaCl concentrations spanning 0.0054 to 0.21 M. At 5 °C the average ratio $\frac{k_{Cl^-}}{k_w}$ is 1260 ± 80 but decreases to 1150 ± 90 at 25 °C, slightly higher than the room temperature value of 836 ± 32 reported by Behnke *et. al.*[8] and in accord with the range of 700 - 1020 reported by Gaston and Thornton.[15] However, our 1150 ± 90 value for $\frac{k_{Cl^-}}{k_w}$ (25 °C) is significantly larger than values of 480 ± 180, 450 ± 100, and 500 ± 190 reported of by Bertram and Thornton,[9] Roberts *et. al.,*[11] and Ryder *et. al.*[12] respectively. We note that these smaller values were obtained from solutions or particles containing nitrate, bisulfate, or simulated seawater, respectively, which have been shown to reduce the $ClNO_2$ product yield as compared with pure aqueous NaCl solutions.[13]

Table 3.1 also reveals that $\frac{k_{Cl^-}}{k_w}$ steadily declines beyond 0.099 M NaCl at both 5 and 25 °C, with similar behavior observed at intermediate temperatures (see Table 3.S2 and Figure 3.S1 for all data). This discrepancy is not improved by substituting NaCl and water activities for

concentrations, which alter $\frac{k_{Cl^-}}{k_w}$ by only a few percent in the opposite direction.[39] The decrease in $\frac{k_{Cl^-}}{k_w}$ at higher NaCl concentrations is analyzed further in Figure 3.S2, which confirms that statistically significant effects begin at 0.21 M NaCl. With this caveat, Table 3.1 includes this concentration in the average values. Table S4 lists average values in the absence of this 0.21 M data.

The decrease in $\frac{k_{Cl^-}}{k_w}$ at higher concentrations implies that the reaction mechanisms for chlorination and hydrolysis (R3.1 and R3.2) may be impacted by interactions between Cl^-, Na^+, D_2O, and N_2O_5 not taken into account in the rate expressions of eq E3.6. We anticipate that ongoing theoretical work will reveal how propensities for Cl^- and H_2O attack on N_2O_5 change in high salt concentration environments. If confirmed, these studies may necessitate the use of concentration-dependent rate constants for modeling $ClNO_2$ production over wide NaCl concentration ranges.

Table 3.1 $ClNO_2$ Product Yields Φ and Rate Constant Ratios $\frac{k_{Cl^-}}{k_w}$ at 5 and 25 °C.[a]

$[Cl^-]$ (M)	Φ (5°C)	Φ (25°C)	$\left(\frac{\Phi(5°C)}{\Phi(25°C)}\right)_{fit}^{b}$	$\frac{k_{Cl^-}}{k_w}(5°C)^{c}$	$\frac{k_{Cl^-}}{k_w}(25°C)^{c}$	$\left(\frac{\frac{k_{Cl^-}}{k_w}(5°C)}{\frac{k_{Cl^-}}{k_w}(25°C)}\right)_{fit}^{d}$
0.0054	0.12 ± 0.01	0.108 ± 0.007	1.10±0.10	1400 ± 130	1240 ± 90	1.11 ± 0.12
0.014	0.26 ± 0.02	0.244 ± 0.018	1.06±0.10	1390 ± 160	1280 ± 90	1.08 ± 0.14
0.026	0.39 ± 0.03	0.39 ± 0.02	1.02±0.07	1360 ± 140	1320 ± 110	1.03 ± 0.11
0.055	0.53 ± 0.04	0.51 ± 0.05	1.04±0.06	1120 ± 190	1030 ± 190	1.09 ± 0.14
0.099	0.70 ± 0.06	0.68 ± 0.07	1.02±0.09	1300 ± 400	1200 ± 400	1.1 ± 0.3
0.21	0.79 ± 0.03	0.76 ± 0.01	1.04±0.03	1000 ± 200	840 ± 50	1.18 ± 0.16
0.54	0.88 ± 0.03	0.83 ± 0.09	1.06±0.06	800 ± 200	500 ± 400	1.5 ± 0.7
2.4	0.90 ± 0.03	0.9 ± 0.1	0.99±0.08	210 ± 70	500 ± 600	0.4 ± 0.4
Average	---	---	$1.04_5 \pm 0.02_8$	1260 ± 80	1150 ± 90	1.09 ± 0.07

[a] Product yields Φ and $\frac{k_{Cl^-}}{k_w}$ ratios at all temperatures and concentrations are listed in Tables S1 and S2. The error bars in Φ and $\frac{k_{Cl^-}}{k_w}$ are equal to 95% confidence intervals for 3 trials at each temperature and concentration (4 trials for 2.4 M Cl^-). Due to their large experimental uncertainties, the data from the 0.54 and 2.4 M solutions are excluded from the calculation of the averages in the last row.

[b] The product yield ratios, $(\Phi(5°C)/\Phi(25°C))_{fit}$, at each concentration were computed from a linear regression of the 15 Φ values (3 trials for each of 5 temperatures in Table S1). The ratios are then calculated from the 5 and 25 °C values predicted by the linear fit. They are not equal to the arithmetic ratios of the second and third columns. The error bars are determined from the uncertainty in the linear regression slope at the 95% confidence level. The average ratio in the last row is determined from the average of the ratios at the six lowest concentrations. The error bar is equal to the 95% confidence interval computed from these six ratios.

[c] The average values of $\frac{k_{Cl^-}}{k_w}$ for the three intermediate temperatures are 1200 ± 70 (10 °C), 1170 ± 80 (15 °C), and 1180 ± 90 (20 °C). The error bars for these average quantities (and for 5 and 25 °C in the last row) are 95% confidence intervals computed from 18 measurements (3 trials × 6 concentrations). See Figure S3 for global fits to single $\frac{k_{Cl^-}}{k_w}$ ratios at each temperature, which are ~15% lower than the arithmetic averages in the last row.

[d] Following the same procedures as in b), we calculate the ratio of rate constant ratios by first fitting a least squares line to the data in Table S2 for each concentration and then predicting the rate constant ratios at 5 and 25 °C.

3.4.3 Impacts of Using D_2O.

Figure 3.4 compares the $ClNO_2$ product yields obtained in our study with values obtained by previous investigators at room temperature.[8,9,11,12] Notably, our measured product yields are larger than those previously reported. In addition to the added ion effect present in many of the previous experiments, such as the inclusion of sulfate and nitrate, we were curious if our use of D_2O solvent instead of H_2O impacted our measurements. This effect can be investigated by slightly modifying the experiment to measure the $ClNO_2$ product yield in H_2O. The sample solution holder was filled with a solution of 0.097 M NaCl in H_2O and the reference solution holder with a saturated NaCl solution in H_2O. Due to the interference in the mass spectrometer of $I(HNO_3 \cdot H_2O)^-$ detected at m/Q of 207.91 Th with $I(ClNO_2)^-$ detected at m/Q of 207.87 Th, we introduced supplemental D_2O vapor into the transfer line between the flow reactor and the mass spectrometer and cooled the flow reactor to 5 °C to reduce H_2O evaporation. This experiment could only be conducted at 5 °C where enough D_2O could be added to the ion molecule reaction region to suppress $I(H_2O)^-$ chemistry. At higher solution temperatures, and thus H_2O vapor

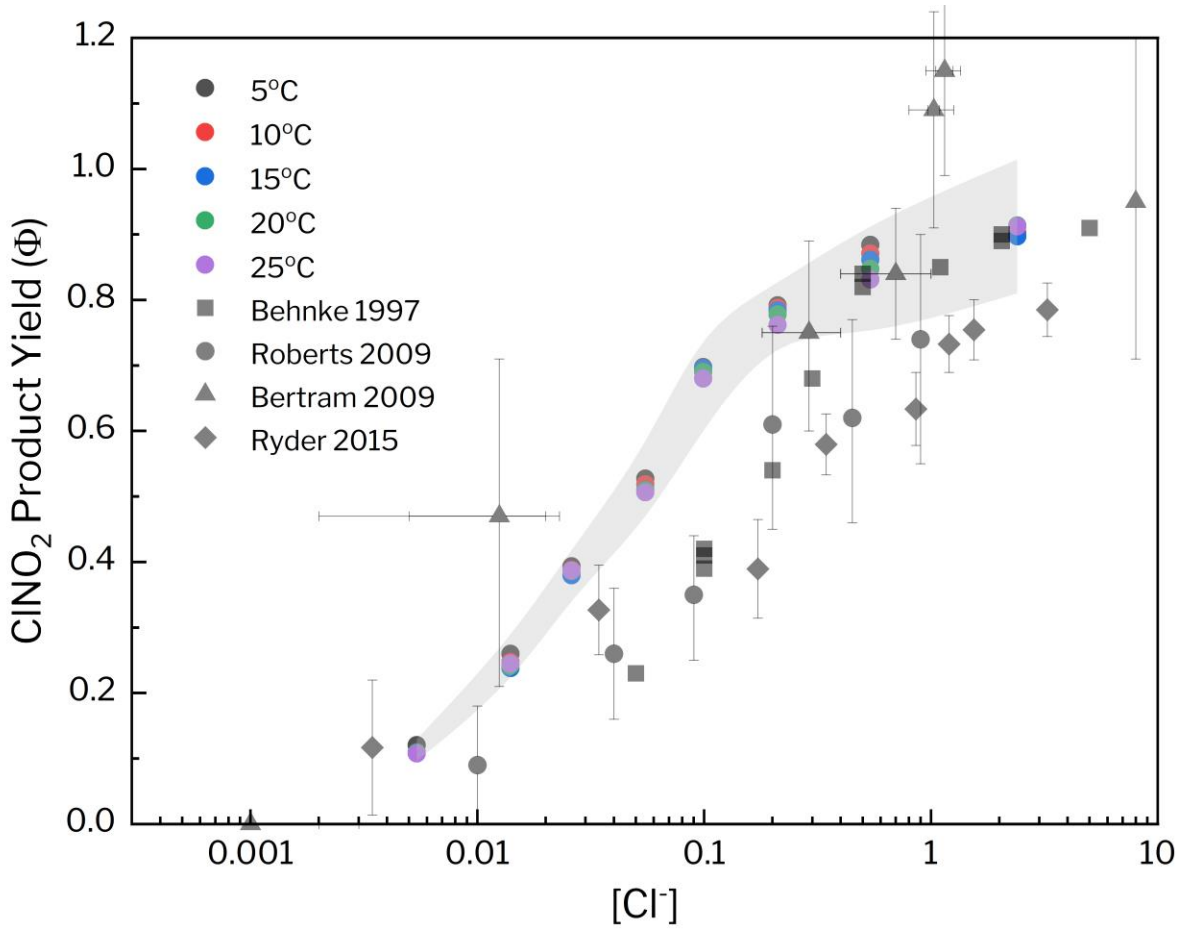

Figure 3-4 Values of the $ClNO_2$ Product Yield as a function of chloride concentration from this study superimposed onto data from previous laboratory experiments. At each concentration, the grey region indicates the 95% confidence interval as determined by the temperature measurement with the largest uncertainty. As indicated, data is from refs 8, 9, 11, 12, and this study.

pressures, $I(H_2O)^-$ remained the dominant reagent ion. We performed the H_2O experiments twice at 0.097 M NaCl in H_2O and obtained product yields of 0.63 and 0.62. These values are 11-12% lower than the product yields of 0.70 observed from our D_2O solution at a nearly identical concentration of 0.099 M NaCl. Using eq 7, we calculate $\frac{k_{Cl^-}}{k_w}$ to be approximately 1.4 times larger in H_2O than in D_2O, which is within the range of reported values for the kinetic isotope effect in the H_2O/D_2O system.[40] This isotope effect may arise in part from the slower motions of D_2O molecules and their weaker autoionization. When we correct our average value for this

effect, we find a value of $k_{\mathrm{Cl}^-}/k_{\mathrm{w}}$ ($\mathrm{H_2O}$, 5 °C) = 900 ± 60, slightly higher than but within the uncertainty of the value of 836 ± 32 reported by Behnke at room temperature.[8]

3.4.4 Arrhenius Analysis.

We next carry out an Arrhenius analysis of R3.1 and R3.2 to determine the difference in activation energies between chlorination and hydrolysis, along with the ratio of pre-exponential factors. The Arrhenius expressions for the rate constants in R3.1 and R3.2 are $k_{\mathrm{Cl}^-} = A_{\mathrm{Cl}^-}\mathrm{e}^{-E_{\mathrm{Cl}^-}/RT}$ and $k_w = A_{\mathrm{w}}\mathrm{e}^{-E_{\mathrm{w}}/RT}$, where $\mathrm{A_{Cl^-}}$ and $\mathrm{A_w}$ are the respective pre-exponential factors for chlorination and hydrolysis and E_{Cl^-} and E_{w} are the activation energies. These expressions enable us to rewrite the $ClNO_2$ product yield (eq 6) as

$$\Phi = \frac{1}{1+\frac{A_{\mathrm{Cl}^-}[\mathrm{Cl}^-]}{A_{\mathrm{w}}[\mathrm{D_2O}]}\mathrm{e}^{\frac{-\Delta E}{RT}}} \tag{E3.8}$$

where $\Delta E = E_{\mathrm{Cl}^-} - E_{\mathrm{w}}$ is the difference in activation energies between chlorination and hydrolysis. To determine ΔE and the ratio of pre-exponential factors from the data, we rearrange eq 8 into a linear form

$$\ln\left(\frac{\Phi}{1-\Phi}\right) = -\frac{\Delta E}{R}\,\frac{1}{T} + \ln\left(\frac{A_{\mathrm{Cl}^-}[\mathrm{Cl}^-]}{A_{\mathrm{w}}[\mathrm{D_2O}]}\right) \tag{E3.9}$$

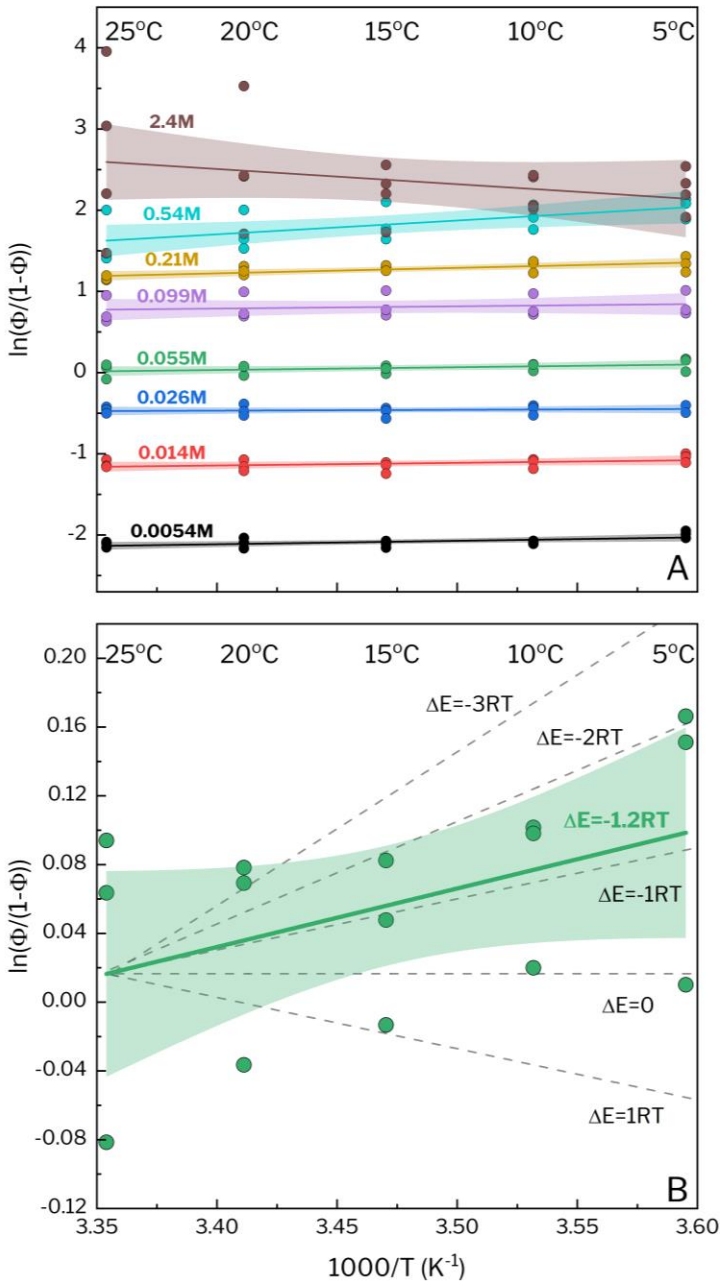

Figure 3-5 **A)** $ClNO_2$ product yield Φ plotted in the form of Eq 9. Note the similar slope of all solutions with $[Cl^-] \leq 0.21$ M. **B)** Expanded view of the data for 0.055 M NaCl showing the linear least squares fit. The shaded dashed lines have slopes corresponding to integer multiples of RT for comparison. In both panels, the shaded regions represent the 95% confidence bands for the lines of best fit. Figure S4 shows magnified plots at all concentrations.

A plot of the product yield data in the form of eq E3.9 is shown in Figure 3.5A, with a magnified view of the data for the 0.055 M solution shown in Figure 3.5B. The slopes of these lines are proportional to $-\Delta E/R$ for the competing reactions, while the y-intercept is equal to

$\ln\left(\frac{A_{Cl^-}[Cl^-]}{A_w[D_2O]}\right)$ based on a linear extrapolation. The data for each solution are offset due to the [Cl^-] dependance of the y-intercept. As seen in panel A, the plots of the low concentration data have very similar positive slopes, corresponding to small negative ΔE values. Panel B reflects the scatter in the data with respect to slopes in units of RT. The extracted ΔE values and A_{Cl^-}/A_w ratios are listed in Table 3.2. We note that the large spread in the $\ln\left(\frac{\Phi}{1-\Phi}\right)$ values obtained from the 0.54 and 2.4 M solutions results in large uncertainties when fitting the slope and intercept, and we have removed these data sets from the average values listed at the bottom of the table.

The resulting average ΔE value of -3.0 ± 1.7 kJ/mol (95% confidence level) indicates that the energetic barrier to chlorination is slightly less than to hydrolysis; at 25 °C this difference in activation energies corresponds to only 1.2 RT and a Boltzmann factor of $e^{-\Delta E/RT} = 3.4$. This surprisingly small factor is a key conclusion of our study: Cl^- and D_2O attack on N_2O_5 have similar energetic barriers despite the differences in charge and complexity of the Cl^- and D_2O reactants. As the measured rate constant for chlorination is approximately one thousand times larger than for hydrolysis, the difference in rate constants must be driven by the pre-exponential ratio, and indeed we extract an average A_{Cl^-}/A_w to be 300^{+400}_{-200} at 25 °C.

Table 3.2. Calculated Values of ΔE and A_{Cl^-}/A_w Using Eq E3.9

[Cl^-] (M)	Δ*E* (kJ/mol)	$\frac{A_{Cl^-}}{A_w}$
0.0054	-4 ± 3	300^{+600}_{-200}
0.014	-3 ± 3	400^{+1300}_{-300}
0.026	-1 ± 3	900^{+2300}_{-700}
0.055	-3 ± 3	300^{+1000}_{-200}
0.099	-2 ± 8	500^{+11000}_{-500}
0.211	-6 ± 3	90^{+260}_{-70}
0.54	-14 ± 11	2^{+189}_{-2}
2.4	+20 ± 30	$2\times10^{5}{}^{+1\times10^{10}}_{-2\times10^{5}}$
Average[a]	-3.0 ± 1.7	300^{+400}_{-200}

[a] Due to the large experimental uncertainties shown in Figure 3.5A, the 0.54 M and 2.4 M data are excluded from the averages. The error bars are 95% confidence intervals derived from the least square analysis of the fits to eq E3.9 in Figure 3.5A, while the error bars for the average values are 95% confidence intervals for six entries in the table. See the SI and Figures 3.S4, 3.S5, and 3.S6 for a statistical analysis of the uncertainty.

3.4.5 Theoretical Analysis.

There are currently no measurements of the individual activation energies for hydrolysis or chlorination and theoretical studies have been limited. Work by Gerber and coworkers locate a barrier of 50 kJ/mol for $N_2O_5(H_2O)_{20}$ for hydrolysis and 31 kJ/mol for chlorination in a $[ClN_2O_5(H_2O)_{12}]^-$ cluster.[10,23] These calculations qualitatively agree with our experimental finding that chlorination is more favorable than hydrolysis, though the calculated difference of 19 kJ/mol is larger than the 3 kJ/mol value we have obtained. Generally, such computational studies indicate that hydrolysis proceeds from a hydrophobically solvated N_2O_5 molecule with

weak hydrogen bonding but significant fluctuating ion-pair character, $NO_2^{\delta+}NO_3^{\delta-}$.[23–25] Hydrolysis can proceed by nucleophilic attack of $OH^{\delta-}$ on $NO_2^{\delta+}$ or electrophilic attack of $H^{\delta+}$ on $NO_3^{\delta-}$. In both cases, solvent water molecules may rearrange into more structured configurations to stabilize a transition state consisting of ion pair-like $NO_2^{\delta+}NO_3^{\delta-}$ and adjacent $H^{\delta+}OH^{\delta-}$. In contrast, attack of Cl^- on $NO_2^{\delta+}NO_3^{\delta-}$ may involve the transformation of tightly bound water molecules around the Cl^- ion into a looser structure around a larger and more charge diffuse $[ClN_2O_5]^-$ transition state. The enthalpic penalty incurred upon de-solvation of the Cl^- ion may be partially compensated by an entropic benefit resulting from the co-solvation of Cl^- and N_2O_5 within the same solvent pocket, while Cl^- itself may assist in inducing charge separation in N_2O_5 and thus facilitate chlorination.

To garner a better understanding of potential reaction mechanisms for chlorination and hydrolysis, we utilized molecular dynamics simulations. See the SI for a full description of these methods. Using the measured ratio of rate constants and solute and solvent standard states $c^o(Cl^-)$ = 1 M and $c^o(D_2O)$ = 55.1 M, we compute a difference in free energy barriers of $\Delta\Delta F^{\ddagger} = -RT\ln\left(\frac{k_{Cl^-}c^o(Cl^-)}{k_w c^o(D_2O)}\right) = -7 \pm 2$ kJ/mol, about twice the value measured from the change in activation energy. The remaining difference comes from the pre-exponential factor that in principle includes both dynamic and entropic contributions to the relative rates. Entropic contributions are fundamentally molecular and can be explored with simulation techniques. While a full understanding of the molecular underpinnings of the relative driving forces for hydrolysis and chlorination is beyond the scope of the current work, the results of molecular dynamics simulations employing optimized point charge models of N_2O_5 and Cl^- shown in Figure 3.6 illustrate a dramatic difference between their local solvation environments. Shown are

the radial distribution functions, $g(r)$, between the water and each solute, where the hydrophobic solvation of N_2O_5 is evident by its unstructured density profile, while the highly hydrophilic solvation of Cl^- is clear by the prominent first solvation shell structure. A potential entropic difference between hydrolysis and chlorination may thus arise from solvent water

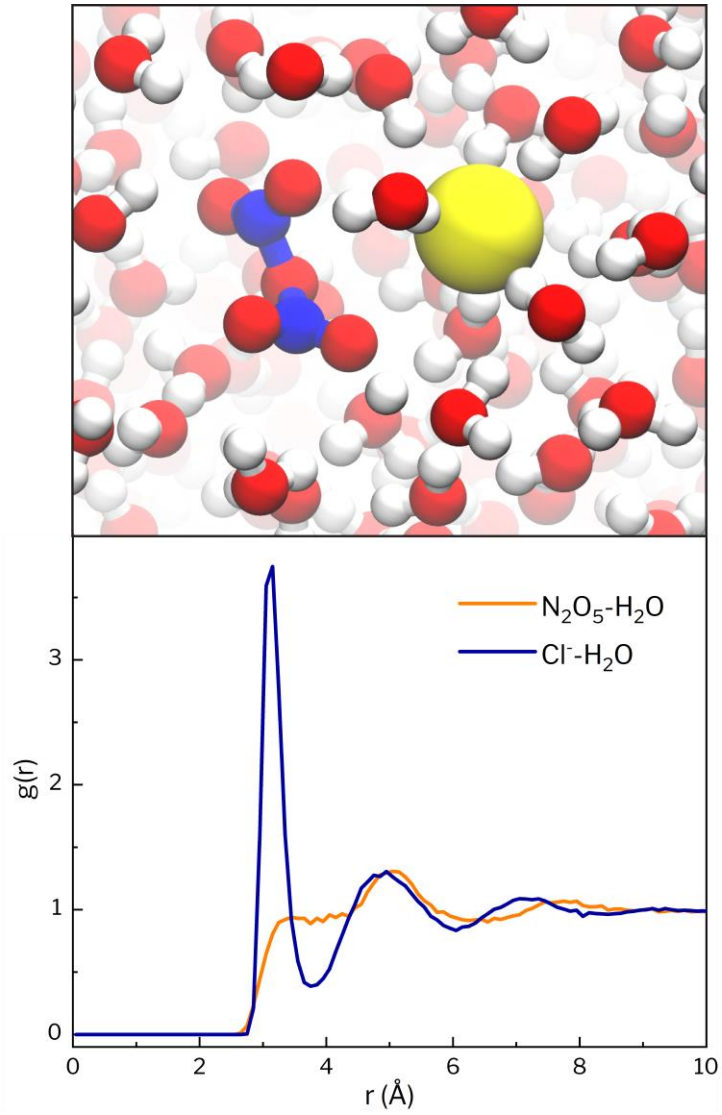

Figure 3-6 Characteristic snapshot of the solvated N_2O_5 and Cl^- complex (top) and the radial distribution functions between the solute centers and surround water (bottom). See the SI for a description of the theoretical methods.

rearrangements as reactants evolve into their transition states. Such studies are ongoing.

Apart from entropic contributions, the relative pre-exponential factors to the rates of chlorination and hydrolysis encode fundamentally dynamical information. The dynamic contribution to the rate ratio reflects differences in the flux of reactants over the relevant transition states, which consist of contributions from both diffusive fluxes for the two species to meet each other in space and attempt frequencies to overcome the reaction barriers. While there is not a direct measurement of either the absolute chlorination or hydrolysis rates, recent theoretical work combining molecular simulation and observed gaseous uptake measurements has narrowed a likely value of the hydrolysis rate constant in pure water to be $k_w = (7 \pm 5) \times 10^5/\mathrm{M/s}$.[25] Because this simulation neglects nuclear quantum effects, it should be more applicable to the D_2O solutions investigated here than to H_2O solutions. Taking the rate constant ratio of 1150 ± 90 from our 25 °C low concentration measurements (averaged between 0.0054 and 0.21 M), the chlorination rate constant is estimated to be $k_{\mathrm{Cl^-}} = (8 \pm 6) \times 10^8/\mathrm{M/s}$.

To understand potential dynamical effects, we can estimate the rate of chlorination assuming it proceeds in the diffusion limit. Under dilute solution conditions, the diffusion constants for N_2O_5 and Cl^- are approximately $D_{\mathrm{N_2O_5}} = 1.6{\times}10^{-5}\mathrm{cm^2/s}$ and $D_{\mathrm{Cl^-}} = 1.7{\times}10^{-5}\mathrm{cm^2/s}$ at 25 °C (scaled from their values in H_2O to D_2O by multiplying by 0.82.)[25,41] Assuming a capture radius of λ = 3.1 Å, taken from the peak in the first solvation shell of the two solutes in Figure 6, the diffusion-limited rate constant can be estimated as $k_{\mathrm{Cl^-}}^{\mathrm{diff}} = 4\pi(D_{\mathrm{N2O5}} + D_{\mathrm{Cl^-}})\lambda = (8 \pm 6){\times}10^9/\mathrm{M/s}$, roughly an order of magnitude faster than the estimated rate constant. This calculation is both temperature and concentration dependent: at 5 °C the Cl^- diffusion constant is 58% of the value at 25 °C, while in a 2.4 M NaCl solution the Cl^- diffusion constant is 77% of the infinite dilution value.[42] Together, these estimates suggest that the temperature and salt concentration dependence of the diffusion coefficients themselves may

explain part of the trends in Table 1. We are currently investigating the mechanism for chlorination in extended water simulations,[10,27,28] which when compared with the mechanism for hydrolysis,[21,22] will hopefully explain the small difference in activation energies and large difference in activation entropies between these ion-neutral solute-solute and neutral-neutral solute-solvent reactions.

3.5 Summary and Conclusions

We have measured the temperature dependence of the $ClNO_2$ product yield over 5 to 25 °C following N_2O_5 reactive uptake to 0.0054 to 2.4 M NaCl/D_2O solutions. The $ClNO_2$ yield decreases on average by less than 5% over this 20 °C range, with less reproducible results at 0.54 M and 2.4 M NaCl. An Arrhenius analysis reveals the difference in activation energies between chlorination and hydrolysis, $E_{Cl^-} - E_w$, to be only -3.0 ± 1.7 kJ/mol (on par with thermal energy at room temperature), despite a thousand-fold greater rate constant for chlorination than for hydrolysis. These two measurements in turn reflect a ratio of Arrhenius pre-exponential factors, $\left(\frac{A_{Cl^-}}{A_w}\right)$, equal on average to 300^{+400}_{-200}. This large ratio implies that the difference in rate constants is primarily driven by dynamic and entropic rather than enthalpic considerations, perhaps due to different solvent shell rearrangements required to stabilize the respective transition states. We are now exploring the mechanisms for chlorination and hydrolysis by machine learning reactive many body potentials to understand the origins of these entropic effects.[24]

The small change in $ClNO_2$ product yield over 5 to 25 °C suggests that its temperature dependence will not play a large role in atmospheric models in this temperature range. The data also provide hints that the rate constant ratio, $\frac{k_{Cl^-}}{k_w}$, decreases at high chloride concentrations (as detailed in the SI). These results have been obtained only for pure sodium chloride solutions. As shown previously, the addition of sulfate or acetate ions, the neutral surfactant phenol, or humic

acid each significantly reduces the production of $ClNO_2$ from N_2O_5 reactive uptake, in all cases by more than two fold.[12,13] These ions and organic surfactants are ubiquitous components of sea spray.[43] Recent ab initio molecular dynamics calculations further indicate that S_N2 reactions of sulfate and formate leading to hydrolysis of N_2O_5 proceed with barriers that are 17 and 13 kJ/mol lower, respectively, than reactions with chloride leading to $ClNO_2$.[10] These calculations imply that sulfate and carboxylate anions may compete even more favorably at lower temperatures, and thereby reduce the $ClNO_2$ yield beyond chloride alone, potentially leading atmospheric models to overestimate its abundance. Experiments testing this hypothesis will help unravel multiple competitive hydrolysis and halogenation reactions occurring in sea spray aerosols over a range of temperatures and compositions.

3.6 Acknowledgements

This work was funded by the National Science Foundation through the National Science Foundation Center for Aerosol Impacts on Chemistry of the Environment (NSF-CAICE) under Grant No. CHE 1801971. We thank R. Benny Gerber, Natalia Karimova, Andreas Götz, and Mark Johnson for many enlightening discussions. We also thank the reviewers for their incisive comments.

3.7 TOC Graphic

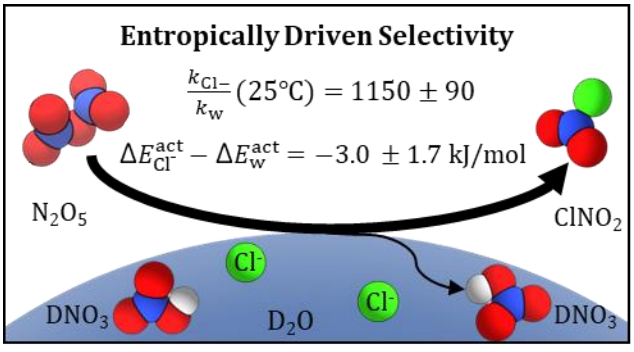

Figure 3-7 Graphic submitted for the journal's TOC.

3.8 References

(1) Chang, W. L.; Brown, S. S.; Stutz, J.; Middlebrook, A. M.; Bahreini, R.; Wagner, N. L.; Dubé, W. P.; Pollack, I. B.; Ryerson, T. B.; Riemer, N. Evaluating N_2O_5 Heterogeneous Hydrolysis Parameterizations for CalNex 2010. *J. Geophys. Res. Atmos.* **2016**, *121* (9), 5051–5070. https://doi.org/10.1002/2015JD024737.

(2) Brown, S. S.; Stutz, J. Nighttime Radical Observations and Chemistry. *Chem. Soc. Rev.* **2012**, *41* (19), 6405–6447. https://doi.org/10.1039/C2CS35181A.

(3) Simpson, W. R.; Brown, S. S.; Saiz-Lopez, A.; Thornton, J. A.; von Glasow, R. Tropospheric Halogen Chemistry: Sources, Cycling, and Impacts. *Chem. Rev.* **2015**, *115* (10), 4035–4062. https://doi.org/10.1021/cr5006638.

(4) Sarwar, G.; Simon, H.; Xing, J.; Mathur, R. Importance of Tropospheric $ClNO_2$ Chemistry across the Northern Hemisphere. *Geophys. Res. Lett.* **2014**, *41* (11), 4050–4058. https://doi.org/10.1002/2014GL059962.

(5) Macintyre, H. L.; Evans, M. J. Sensitivity of a Global Model to the Uptake of N_2O_5 by Tropospheric Aerosol. *Atmos. Chem. Phys.* **2010**, *10* (15), 7409–7414. https://doi.org/10.5194/acp-10-7409-2010.

(6) Riemer, N.; Vogel, H.; Vogel, B.; Schell, B.; Ackermann, I.; Kessler, C.; Hass, H. Impact of the Heterogeneous Hydrolysis of N_2O_5 on Chemistry and Nitrate Aerosol Formation in the Lower Troposphere under Photosmog Conditions. *J. Geophys. Res. Atmos.* **2003**, *108* (D4). https://doi.org/10.1029/2002JD002436.

(7) Pathak, R. K.; Wang, T.; Wu, W. S. Nighttime Enhancement of PM2.5 Nitrate in Ammonia-Poor Atmospheric Conditions in Beijing and Shanghai: Plausible Contributions of

Heterogeneous Hydrolysis of N_2O_5 and HNO_3 Partitioning. *Atmospheric Environ.* **2011**, *45* (5), 1183–1191. https://doi.org/10.1016/j.atmosenv.2010.09.003.

(8) Behnke, W.; George, C.; Scheer, V.; Zetzsch, C. Production and Decay of $ClNO_2$ from the Reaction of Gaseous N_2O_5 with NaCl Solution: Bulk and Aerosol Experiments. *J. Geophys. Res. Atmos.* **1997**, *102* (D3), 3795–3804. https://doi.org/10.1029/96JD03057.

(9) Bertram, T. H.; Thornton, J. A. Toward a General Parameterization of N_2O_5 Reactivity on Aqueous Particles: The Competing Effects of Particle Liquid Water, Nitrate and Chloride. *Atmospheric Chem. Phys.* **2009**, *9* (21), 8351–8363. https://doi.org/10.5194/acp-9-8351-2009.

(10) Karimova, N. V.; Chen, J.; Gord, J. R.; Staudt, S.; Bertram, T. H.; Nathanson, G. M.; Gerber, R. B. S_N2 Reactions of N_2O_5 with Ions in Water: Microscopic Mechanisms, Intermediates, and Products. *J. Phys. Chem. A* **2020**, *124* (4), 711–720. https://doi.org/10.1021/acs.jpca.9b09095.

(11) Roberts, J. M.; Osthoff, H. D.; Brown, S. S.; Ravishankara, A. R.; Coffman, D.; Quinn, P.; Bates, T. Laboratory Studies of Products of N_2O_5 Uptake on Cl^- Containing Substrates. *Geophys. Res. Lett.* **2009**, *36* (20). https://doi.org/10.1029/2009GL040448.

(12) Ryder, O. S.; Campbell, N. R.; Shaloski, M.; Al-Mashat, H.; Nathanson, G. M.; Bertram, T. H. Role of Organics in Regulating $ClNO_2$ Production at the Air–Sea Interface. *J. Phys. Chem. A* **2015**, *119* (31), 8519–8526. https://doi.org/10.1021/jp5129673.

(13) Staudt, S.; Gord, J. R.; Karimova, N. V.; McDuffie, E. E.; Brown, S. S.; Gerber, R. B.; Nathanson, G. M.; Bertram, T. H. Sulfate and Carboxylate Suppress the Formation of $ClNO_2$ at Atmospheric Interfaces. *ACS Earth Space Chem.* **2019**, *3* (9), 1987–1997. https://doi.org/10.1021/acsearthspacechem.9b00177.

(14) Schweitzer, F.; Mirabel, P.; George, C. Multiphase Chemistry of N_2O_5, $ClNO_2$, and $BrNO_2$. *J. Phys. Chem. A* **1998**, *102* (22), 3942–3952. https://doi.org/10.1021/jp980748s.

(15) Gaston, C. J.; Thornton, J. A. Reacto-Diffusive Length of N_2O_5 in Aqueous Sulfate- and Chloride-Containing Aerosol Particles. *J. Phys. Chem. A* **2016**, *120* (7), 1039–1045. https://doi.org/10.1021/acs.jpca.5b11914.

(16) Thornton, J. A.; Braban, C. F.; Abbatt, J. P. D. N_2O_5 Hydrolysis on Sub-Micron Organic Aerosols: The Effect of Relative Humidity, Particle Phase, and Particle Size. *Phys. Chem. Chem. Phys.* **2003**, *5* (20), 4593–4603. https://doi.org/10.1039/B307498F.

(17) McNeill, V. F.; Patterson, J.; Wolfe, G. M.; Thornton, J. A. The Effect of Varying Levels of Surfactant on the Reactive Uptake of N_2O_5 to Aqueous Aerosol. *Atmospheric Chem. Phys.* **2006**, *6* (6), 1635–1644. https://doi.org/10.5194/acp-6-1635-2006.

(18) Stewart, D. J.; Griffiths, P. T.; Cox, R. A. Reactive Uptake Coefficients for Heterogeneous Reaction of N_2O_5 with Submicron Aerosols of NaCl and Natural Sea Salt. *Atmospheric Chem. Phys.* **2004**, *4* (5), 1381–1388. https://doi.org/10.5194/acp-4-1381-2004.

(19) George, C.; Ponche, J. L.; Mirabel, P.; Behnke, W.; Scheer, V.; Zetzsch, C. Study of the Uptake of N_2O_5 by Water and NaCl Solutions. *J. Phys. Chem.* **1994**, *98* (35), 8780–8784. https://doi.org/10.1021/j100086a031.

(20) Mozurkewich, M.; Calvert, J. G. Reaction Probability of N_2O_5 on Aqueous Aerosols. *J. Geophys. Res. Atmos.* **1988**, *93* (D12), 15889–15896. https://doi.org/10.1029/JD093iD12p15889.

(21) Bianco, R.; Hynes, J. T. Theoretical Studies of Heterogeneous Reaction Mechanisms Relevant for Stratospheric Ozone Depletion. *Int. J. Quantum Chem.* **1999**, *75* (4–5), 683–692. https://doi.org/10.1002/(SICI)1097-461X(1999)75:4/5<683::AID-QUA35>3.0.CO;2-F.

(22) McNamara, J. P.; Hillier, I. H. Structure and Reactivity of Dinitrogen Pentoxide in Small Water Clusters Studied by Electronic Structure Calculations. *J. Phys. Chem. A* **2000**, *104* (22), 5307–5319. https://doi.org/10.1021/jp994279l.

(23) Rossich Molina, E.; Gerber, R. B. Microscopic Mechanisms of N_2O_5 Hydrolysis on the Surface of Water Droplets. *J. Phys. Chem. A* **2020**, *124* (1), 224–228. https://doi.org/10.1021/acs.jpca.9b08900.

(24) Galib Mirza; Limmer David T. Reactive Uptake of N2O5 by Atmospheric Aerosol Is Dominated by Interfacial Processes. *Science* **2021**, *371* (6532), 921–925. https://doi.org/10.1126/science.abd7716.

(25) Cruzeiro, V. W. D.; Galib, M.; Limmer, D. T.; Götz, A. W. Uptake of N_2O_5 by Aqueous Aerosol Unveiled Using Chemically Accurate Many-Body Potentials. *Nat. Commun.* **2022**, *13* (1), 1266. https://doi.org/10.1038/s41467-022-28697-8.

(26) Hirshberg, B.; Molina, E. R.; Götz, A. W.; Hammerich, A. D.; Nathanson, G. M.; Bertram, T. H.; Johnson, M. A.; Gerber, R. B. N_2O_5 at Water Surfaces: Binding Forces, Charge Separation, Energy Accommodation and Atmospheric Implications. *Phys. Chem. Chem. Phys.* **2018**, *20* (26), 17961–17976. https://doi.org/10.1039/C8CP03022G.

(27) McNamara, J. P.; Hillier, I. H. Exploration of the Atmospheric Reactivity of N_2O_5 and HCl in Small Water Clusters Using Electronic Structure Methods. *Phys. Chem. Chem. Phys.* **2000**, *2* (11), 2503–2509. https://doi.org/10.1039/B001497O.

(28) Hammerich, A. D.; Finlayson-Pitts, B. J.; Gerber, R. B. Mechanism for Formation of Atmospheric Cl Atom Precursors in the Reaction of Dinitrogen Oxides with HCl/Cl^- on Aqueous Films. *Phys. Chem. Chem. Phys.* **2015**, *17* (29), 19360–19370. https://doi.org/10.1039/C5CP02664D.

(29) Kercher, J. P.; Riedel, T. P.; Thornton, J. A. Chlorine Activation by N_2O_5: Simultaneous, in Situ Detection of $ClNO_2$ and N_2O_5 by Chemical Ionization Mass Spectrometry. *Atmos. Meas. Tech.* **2009**, *2* (1), 193–204. https://doi.org/10.5194/amt-2-193-2009.

(30) Lee, B. H.; Lopez-Hilfiker, F. D.; Mohr, C.; Kurtén, T.; Worsnop, D. R.; Thornton, J. A. An Iodide-Adduct High-Resolution Time-of-Flight Chemical-Ionization Mass Spectrometer: Application to Atmospheric Inorganic and Organic Compounds. *Environ. Sci. Technol.* **2014**, *48* (11), 6309–6317. https://doi.org/10.1021/es500362a.

(31) Pegram, L. M.; Record, M. T. Hofmeister Salt Effects on Surface Tension Arise from Partitioning of Anions and Cations between Bulk Water and the Air−Water Interface. *J. Phys. Chem. B* **2007**, *111* (19), 5411–5417. https://doi.org/10.1021/jp070245z.

(32) Bertram, T. H.; Thornton, J. A.; Riedel, T. P. An Experimental Technique for the Direct Measurement of N_2O_5 Reactivity on Ambient Particles. *Atmos. Meas. Tech.* **2009**, *2* (1), 231–242. https://doi.org/10.5194/amt-2-231-2009.

(33) Osthoff, H. D.; Roberts, J. M.; Ravishankara, A. R.; Williams, E. J.; Lerner, B. M.; Sommariva, R.; Bates, T. S.; Coffman, D.; Quinn, P. K.; Dibb, J. E.; Stark, H.; Burkholder, J. B.; Talukdar, R. K.; Meagher, J.; Fehsenfeld, F. C.; Brown, S. S. High Levels of Nitryl Chloride in the Polluted Subtropical Marine Boundary Layer. *Nature Geosci.* **2008**, *1* (5), 324–328. https://doi.org/10.1038/ngeo177.

(34) Burkholder, J. B.; Sander, J. P.; Abbatt, J. P. D.; Barker, J. R.; Cappa, C. D.; Crounse, J. D.; Dibble, T. S.; Huie, R. E.; Kolb, C. E.; Kurylo, M. J.; Orkin, V. L.; Percival, C. J.; Wilmouth, D. M.; Wine, P. H. *JPL Publication 19-5. Chemical Kinetics and Photochemical Data for Use in Atmospheric Studies*; p 1610.

(35) Royer, H. M.; Mitroo, D.; Hayes, S. M.; Haas, S. M.; Pratt, K. A.; Blackwelder, P. L.; Gill, T. E.; Gaston, C. J. The Role of Hydrates, Competing Chemical Constituents, and Surface Composition on $ClNO_2$ Formation. *Environ. Sci. Technol.* **2021**, *55* (5), 2869–2877. https://doi.org/10.1021/acs.est.0c06067.

(36) Dörich, R.; Eger, P.; Lelieveld, J.; Crowley, J. N. Iodide CIMS and *m/z* 62: The Detection of HNO_3 as NO_3^- in the Presence of PAN, Peroxyacetic Acid and Ozone. *Atmos. Meas. Tech.* **2021**, *14* (8), 5319–5332. https://doi.org/10.5194/amt-14-5319-2021.

(37) *CRC Handbook of Chemistry and Physics*; Rumble, J. R., Ed.; Taylor and Francis, 2021. Data from section on *CODATA Key Values for Thermodynamics*.

(38) Sander, R. Compilation of Henry's Law Constants (Version 4.0) for Water as Solvent. *Atmospheric Chem. Phys.* **2015**, *15* (8), 4399–4981. https://doi.org/10.5194/acp-15-4399-2015.

(39) Robinson, R. A.; Stokes, R. H. *Electrolyte Solutions, Second Revised Edition*; Dover Publications.

(40) Virtanen, N.; Polari, L.; Välilä, M.; Mikkola, S. Kinetic Solvent Deuterium Isotope Effect in Transesterification of RNA Models. *J. Phys. Org. Chem.* **2005**, *18* (5), 385–397. https://doi.org/10.1002/poc.883.

(41) Swain, C. G.; Evans, D. F. Conductance of Ions in Light and Heavy Water at 25°. *J. Am. Chem. Soc.* **1966**, *88* (3), 383–390. https://doi.org/10.1021/ja00955a001.

(42) Vitagliano, V.; Lyons, P. A. Diffusion Coefficients for Aqueous Solutions of Sodium Chloride and Barium Chloride. *J. Am. Chem. Soc.* **1956**, *78* (8), 1549–1552. https://doi.org/10.1021/ja01589a011.

(43) Bertram, T. H.; Cochran, R. E.; Grassian, V. H.; Stone, E. A. Sea Spray Aerosol Chemical Composition: Elemental and Molecular Mimics for Laboratory Studies of Heterogeneous and Multiphase Reactions. *Chem. Soc. Rev.* **2018**, *47* (7), 2374–2400. https://doi.org/10.1039/C7CS00008A.

3.9 Supporting Information

3.9.1 Experimental Data

Table 3.S1 lists the raw experimental values obtained from repeated measurements of the $ClNO_2$ product yield from NaCl solutions in D_2O measuring 0.0054, 0.014, 0.026, 0.055, 0.099, 0.21, 0.54, and 2.4 M at the temperatures of 5, 10, 15, 20, and 25 ˚C. The error bars for the averages are 95% confidence intervals for three measurements (four measurements for 2.4 M). These data are plotted in Figure 3 of the main text.

Table 3.S2 lists the k_{Cl^-}/k_w ratios obtained from the product yields in Table S1 using eq 7 in the main text. The error bars for the averages are 95% confidence intervals for the indicated number of measurements. The average k_{Cl^-}/k_w ratios for the 5 and 25 ˚C solutions are also presented in Table 1 of the main text.

Figure 3.S1 shows individual plots of the k_{Cl^-}/k_w ratios from Table 3.S2. The shaded

regions in Figures S1-S4 are 95% confidence bands, which reflect the uncertainty of the vertical deviations in each linear regression. They are smallest in the middle of a graph, where the x value (temperature) is surrounded by other x values, and largest at the end points. There is a 95% probability that the true line lies within the band. The shift in positions of each curve illustrate the measured dependence of k_{Cl^-}/k_w on the concentration of NaCl, particularly in panels F, G, and H See the following websites for more information on confidence bands: https://www.originlab.com/doc/Origin-Help/Fitted_Curve_Plot_Analysis and https://rstudio-pubs-static.s3.amazonaws.com/195401_20b3272a8bb04615ae7ee4c81d18ffb5.html.

Figure 3.S2 display plots of k_{Cl^-}/k_w versus NaCl concentration at each temperature in panels, along with slopes, 95% confidence intervals, and *p*-values from *t*-tests. They indicate that the rate constant ratio depends on NaCl concentration at the 95% confidence level ($p < 0.05$), largely because of the 0.21 M data. Without the 0.21 M data, the null hypothesis of no correlation prevails at all temperatures.

Figure S3 shows the global fit to a single k_{Cl^-}/k_w ratio obtained from a rearranged form of eq 7 in the main text, $\Phi/(1-\Phi) = (k_{Cl^-}/k_w)[Cl^-]/[D_2O]$, where Φ is the $ClNO_2$ product yield (Table 3.S1). The graph is a plot of $\Phi/(1-\Phi)$ versus $[Cl^-]/[D_2O]$ at 25 °C for solutions between 0.0054 and 0.21 M $[Cl^-]$ in Panel A and for all solutions in Panel B.

In Panel A of Figure 3.S3, the slope of the least-squares line yields a global fit for k_{Cl^-}/k_w of 840 ± 100 (95% confidence level). This value is smaller than the k_{Cl^-}/k_w value of 1150 ± 90 listed in Table 3.1 in the main text, which was calculated as an arithmetic average of the 18 values at 25 °C presented in Table 3.S2. This difference arises from the least squares fit of the lower 0.21 M value, which is weighted more by the linear regression than by an arithmetic

average. Plots at the four other temperatures reveal similar behavior. A comparison of the 18-point averages at all temperatures from Table 3.S2 and global least-squares fits are presented in Table 3.S3.

In Panel B of Figure 3.S3, we compare the global fits from six lowest concentrations (0.0054 – 0.21 M) in orange with the global fit using all 8 solution concentrations (0.54 M and 2.4 M values are presented as black points). The global fit using all 8 concentrations is the solid black line, which yields a $k_{\mathrm{Cl}^-}/k_{\mathrm{w}}$ ratio of 460 ± 200. Panels A and B further emphasize the reduction in $k_{\mathrm{Cl}^-}/k_{\mathrm{w}}$ at higher NaCl concentrations, calculated either calculated by global fits from this figure or from individual concentrations (Table 3.S2 and Figure 3.S1).

Table 3.S3 compares the arithmetic average $k_{\mathrm{Cl}^-}/k_{\mathrm{w}}$ values calculated from the individual $k_{\mathrm{Cl}^-}/k_{\mathrm{w}}$ presented in Table 3.S2 with the global fit $k_{\mathrm{Cl}^-}/k_{\mathrm{w}}$ values determined at each temperature for the solutions between 0.0054 and 0.21 M [Cl^-]. An example of a global fit is given in Figure S2. The error bars are 95% confidence intervals for the respective calculations.

Figure 3.S4 shows individual plots of the data from Table S1 in the form of eq E3.9 from the main text. These plots are used to determine ΔE and $A_{\mathrm{Cl}^-}/A_{\mathrm{w}}$ at each concentration. Each panel also includes a 95% confidence band.

Figure 3.S5 shows a plot of the activation energy difference between chlorination and hydrolysis ($\Delta E = \Delta E_{\mathrm{Cl}^-} - \Delta E_{\mathrm{w}}$) versus chloride concentration. The large 95% confidence band is reflected in a linear regression *t*-test at a 0.05 significance level. The resulting *p*-value of 0.12 exceeds 0.05 and implies that there is no statistically significant correlation between ΔE and chloride concentration over 0.0054 to 0.21 M NaCl at the 95% confidence level.

Figure 3.S6 shows a plot of the ratio of pre-exponential factors ($A_{\mathrm{Cl}^-}/A_{\mathrm{w}}$) from the Arrhenius fit

(eq E9 in the main text) versus chloride concentration. As above, the large 95% confidence band is reflected in a linear regression *t*-test at a 0.05 significance level. The resulting *p*-value of 0.28 exceeds 0.05 and implies that there is no statistically significant correlation between A_{Cl^-}/A_w and chloride concentration over 0.0054 to 0.21 M NaCl at the 95% confidence level.

We note that, although ΔE and A_{Cl^-}/A_w are found to be statistically independent of NaCl concentration when including 0.21 M NaCl, Figures S1–S3 provides hints that k_{Cl^-}/k_w varies over these (and higher) concentrations. Future simulations and experiments may help to tease out this dependence.

Table 3.S7 uses the reports average values of Φ(5 °C) /Φ(25 °C), k_{Cl^-}/k_w at all temperatures, k_{Cl^-}/k_w (5 °C) / k_{Cl^-}/k_w (25 °C), ΔE (kJ/mol), and A_{Cl^-}/A_w using the same procedures described in the main text, but we exclude the 0.21 M point along with the 0.54 and 2.4 M points. This table, covering 0.0054 to 0.099 M NaCl, provides kinetic information using solutions that result in $ClNO_2$ product yields from 0.1 to 0.7 (where 70% of the reacting N_2O_5 molecules are converted to $ClNO_2$). These values will be more relevant for low NaCl concentrations in comparison to the averages we present in the main text that include the 0.21 M data.

Table 3.S1 Individual $ClNO_2$ Product Yield Measurements

Experiment Number	5 ˚C	10 ˚C	15 ˚C	20˚C	25 ˚C
$[Cl^-]$ = 0.0054 M					
1	0.1206	0.1081	0.1037	0.1028	0.1039
2	0.1153	0.1118	0.1117	0.1155	0.1104
3	0.1247	0.1084	0.1080	0.1096	0.1084
Average	0.12 ± 0.01	0.109 ± 0.004	0.108 ± 0.008	0.109 ± 0.013	0.108 ± 0.007
$[Cl^-]$ = 0.014 M					
1	0.2693	0.2556	0.2483	0.2551	0.2540
2	0.2617	0.2516	0.2422	0.2390	0.2404
3	0.2480	0.2341	0.2237	0.2297	0.2383
Average	0.26 ± 0.02	0.25 ± 0.02	0.24 ± 0.03	0.24 ± 0.03	0.244 ± 0.018
$[Cl^-]$ = 0.026 M					
1	0.4005	0.3996	0.3923	0.4046	0.3959
2	0.4006	0.3929	0.3844	0.3829	0.3880
3	0.3789	0.3713	0.3621	0.3709	0.3769
Average	0.39 ± 0.03	0.39 ± 0.03	0.38 ± 0.03	0.39 ± 0.04	0.39 ± 0.02
$[Cl^-]$ = 0.055 M					
1	0.5025	0.5050	0.4967	0.4909	0.4796
2	0.5415	0.5254	0.5206	0.5173	0.5159
3	0.5377	0.5245	0.5119	0.5196	0.5235
Average	0.53 ± 0.04	0.52 ± 0.03	0.51 ± 0.03	0.51 ± 0.03	0.51 ± 0.05
$[Cl^-]$ = 0.099 M					
1	0.7334	0.7255	0.7327	0.7299	0.7213
2	0.6750	0.6722	0.6696	0.6669	0.6532
3	0.6838	0.6797	0.6841	0.6736	0.6656
Average	0.70 ± 0.06	0.69 ± 0.06	0.70 ± 0.07	0.69 ± 0.07	0.68 ± 0.07
$[Cl^-]$ = 0.21 M					
1	0.8071	0.7934	0.7853	0.7686	0.7578
2	0.7929	0.7973	0.7889	0.7874	0.7600
3	0.7749	0.7729	0.7780	0.7774	0.7674
Average	0.79 ± 0.03	0.79 ± 0.03	0.78 ± 0.01	0.78 ± 0.02	0.76 ± 0.01
$[Cl^-]$ = 0.54 M					
1	0.8942	0.8875	0.8911	0.8816	0.8810
2	0.8688	0.8533	0.8545	0.8387	0.8088
3	0.8892	0.8711	0.8379	0.8217	0.8034
Average	0.88 ± 0.03	0.87 ± 0.04	0.86 ± 0.06	0.85 ± 0.06	0.83 ± 0.09
$[Cl^-]$ = 2.4 M					
1	0.9113	0.9175	0.9280	0.9715	0.9812
2	0.8715	0.8824	0.9004	0.9180	0.9542
3	0.9268	0.9191	0.9110	0.9187	0.9006
4	0.8993	0.8859	0.8494	0.8468	0.8132
Average	0.90 ± 0.03	0.90 ± 0.03	0.89 ± 0.05	0.91 ± 0.07	0.9 ± 0.1

Table 3.S2 Individual k_{Cl^-}/k_w Ratios from Eq E3.7 using $ClNO_2$ Product Yields from Table 3.S1

Experiment Number	5 ˚C	10 ˚C	15 ˚C	20˚C	25 ˚C
[Cl⁻] = 0.0054 M					
1	1405	1242	1185	1174	1188
2	1335	1290	1288	1338	1271
3	1459	1245	1241	1261	1246
Average	1400 ± 130	1260 ± 50	1240 ± 100	1260 ± 170	1240 ± 90
[Cl⁻] = 0.014 M					
1	1456	1357	1305	1353	1352
2	1401	1328	1263	1241	1250
3	1303	1208	1138	1178	1236
Average	1390 ± 160	1300 ± 160	1240 ± 180	1260 ± 180	1280 ± 90
[Cl⁻] = 0.026 M					
1	1397	1392	1350	1421	1370
2	1398	1353	1306	1297	1326
3	1276	1235	1187	1233	1265
Average	1360 ± 140	1330 ± 170	1280 ± 170	1320 ± 180	1320 ± 110
[Cl⁻] = 0.055 M					
1	1009	1019	986	963	921
2	1180	1106	1085	1070	1065
3	1162	1102	1048	1080	1097
Average	1120 ± 190	1080 ± 100	1040 ± 100	1040 ± 130	1030 ± 190
[Cl⁻] = 0.099 M					
1	1534	1475	1529	1508	1444
2	1159	1144	1131	1117	1051
3	1206	1184	1208	1151	1111
Average	1300 ± 400	1300 ± 400	1300 ± 400	1300 ± 400	1200 ± 400
[Cl⁻] = 0.21 M					
1	1099	1008	960	872	821
2	1005	1032	981	972	831
3	904	894	920	917	866
Average	1000 ± 200	980 ± 150	950 ± 60	920 ± 100	840 ± 50
[Cl⁻] = 0.54 M					
1	857	800	830	751	751
2	672	590	596	527	429
3	814	686	524	468	415
Average	800 ± 200	700 ± 200	700 ± 300	600 ± 300	500 ± 400
[Cl⁻] = 2.4 M					
1	225	243	282	745	1141
2	148	164	198	245	455
3	277	248	224	247	198
4	195	170	123	121	95
Average	210 ± 70	210 ± 60	210 ± 90	300 ± 400	500 ± 600

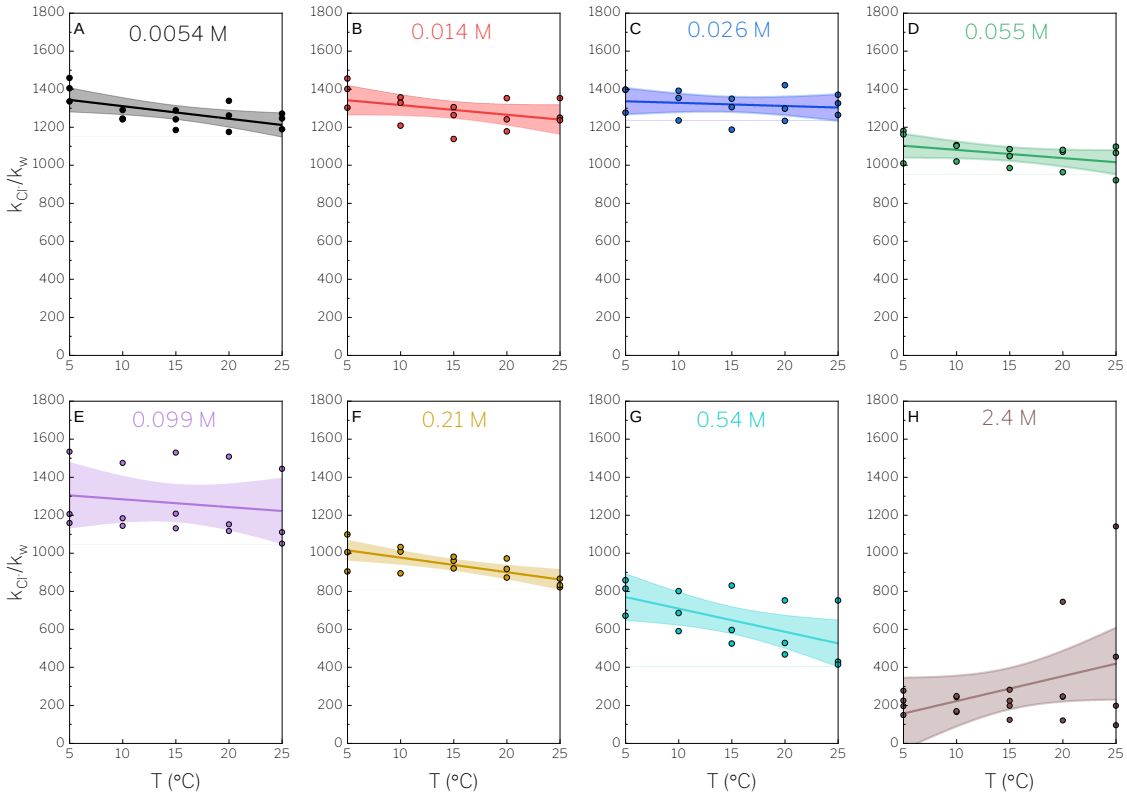

Figure 3-S1 k_{Cl^-}/k_w ratios (listed in Table 3.S2) plotted against temperature for each NaCl solution. The solid lines are linear least-squares fits used to highlight the small changes in k_{Cl^-}/k_w with temperature, listed in Table 3.S2. The shaded regions represent 95% confidence bands for each linear regression. All panels are plotted with the same range of rate constant ratios and temperatures. The vertical positions of each curve illustrate the measured dependence of k_{Cl^-}/k_w on the concentration of NaCl, particularly in panels F, G, and H.

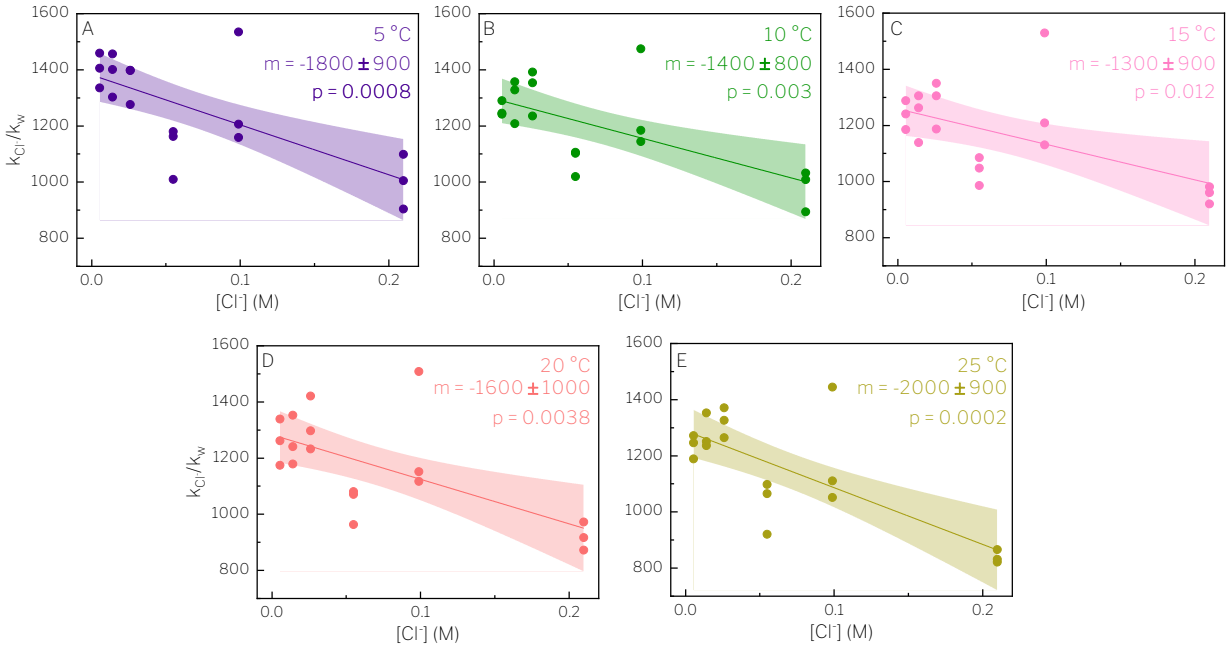

Figure 3-S2 Graphs of k_{Cl^-}/k_w versus NaCl concentration at each temperature for solutions of 0.0054 to 0.21 M [Cl^-]. Each panel lists the linear least squares slope m, the 95% confidence interval as an error bar, and the *p*-value from a *t*-test of the slope. These tests indicate that there is a potential salt dependence on k_{Cl^-}/k_w at the 95% confidence level of $p < 0.05$, largely imposed by the 0.21 M point. Removing the 0.21 M concentration results in *p*-values for the slopes of 0.15, 0.45, 0.94, 0.54, and 0.24 for temperatures 5 to 25 ˚C. They are greater than 0.05, indicating the five lowest concentrations of [Cl^-] do not show a statistically significant trend in k_{Cl^-}/k_w with concentration.

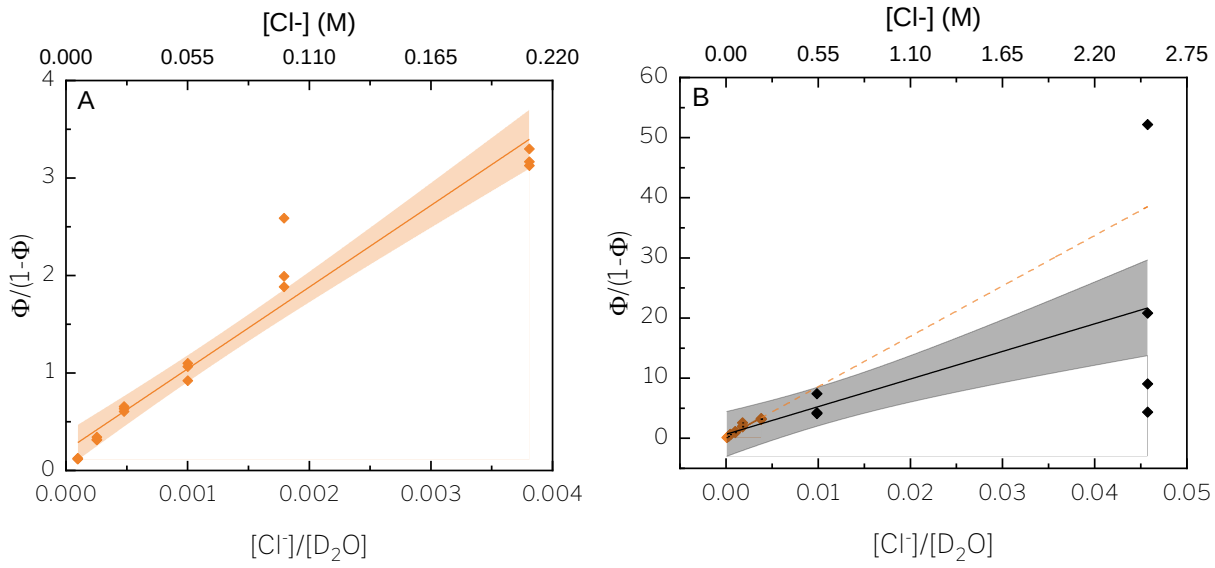

Figure 3-S3 The global fits of the $ClNO_2$ product yields Φ at 25 °C according to $\Phi/(1-\Phi) = (k_{Cl^-}/k_w)[Cl^-]/[D_2O]$ for lowest six NaCl concentrations (0.0054 – 0.21 M NaCl) in Panel A and all concentrations in Panel B. See eq E7 of the main text. The solid orange line is the least squares fit of the six lowest concentrations (orange points). The slope of the least squares line is a single value of k_{Cl^-}/k_w equal to 840 ± 100. The shaded region represents the 95% confidence band for the linear regression. The intercept was allowed to float in the regression. Constraining the intercept to be 0 increases the slope to 920 ± 80. In Panel B, the black points correspond to the two highest concentration solutions (0.54 and 2.4 M NaCl). The solid black line represents the least squares fit for all 8 concentrations (oranges points and black points). Without constraining the intercept, the slope of the fitted line is k_{Cl^-}/k_w equal to 460 ± 200. The dashed orange line is the least squares fit from Panel A extrapolated for higher concentrations.

Table 3.S3 Comparison of Arithmetic Averages and Global Least Squares Fits of k_{Cl^-}/k_w

Temperature (˚C)	**k_{Cl^-}/k_w (Table S2 Average)[a]**	**k_{Cl^-}/k_w (Global Least Squares Fits)[b]**
5	1260 ± 80	1000 ± 100
10	1200 ± 70	980 ± 90
15	1170 ± 80	960 ± 100
20	1180 ± 90	920 ± 100
25	1150 ± 90	840 ± 100

[a] Arithmetic average of 18 k_{Cl^-}/k_w entries from 0.0054 to 0.21 M NaCl in Table 3.S2 at each temperature. [b] k_{Cl^-}/k_w obtained from global fits of the 18 k_{Cl^-}/k_w entries, like that shown in Figure 3.S3. The intercepts were not set to 0. The error bars are 95% confidence intervals.

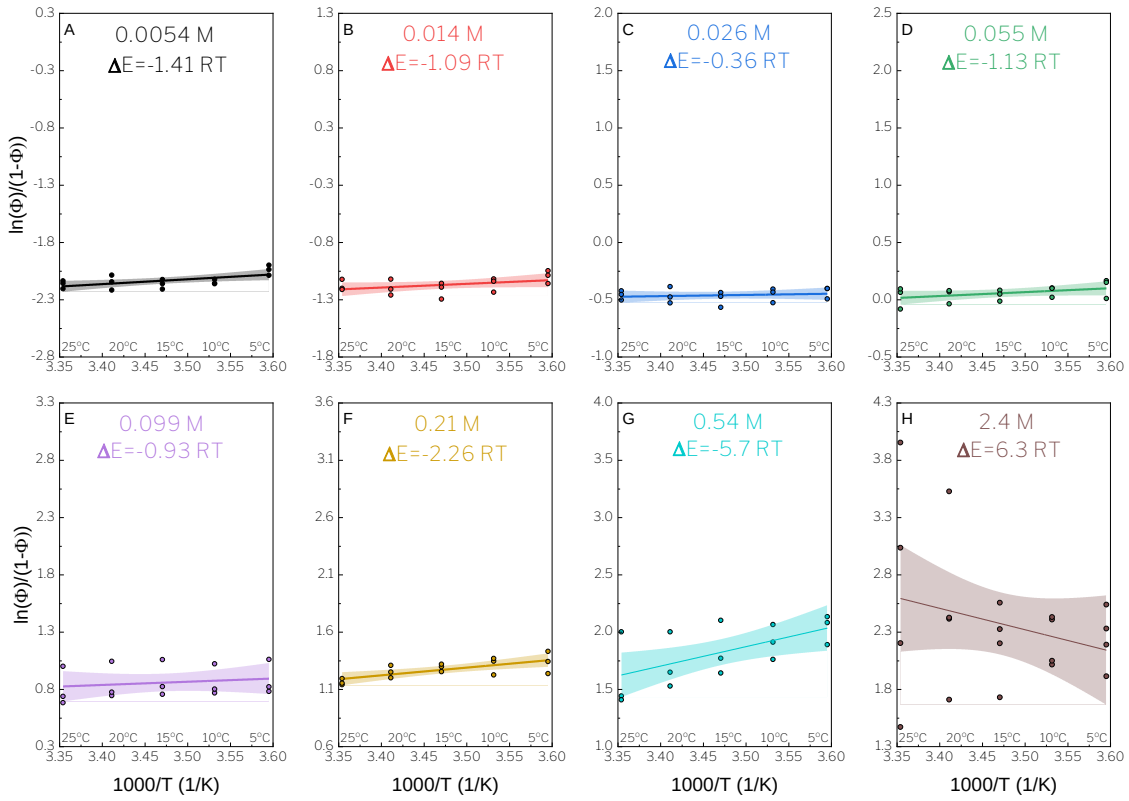

Figure 3-S4 $ClNO_2$ product yield (Φ) plotted in the form of eq E3.9 in the main text. The solid lines are the least-squares fits from which the Arrhenius ΔE and A_{Cl^-}/A_w parameters are obtained. The insets are values of ΔE in terms of RT at $T = 25$ °C. The shaded regions represent the 95% confidence bands for each linear regression. All panels are plotted with the same range of x- and y-values but are offset due to the chloride dependence, as seen in eq E3.9 in the main text.

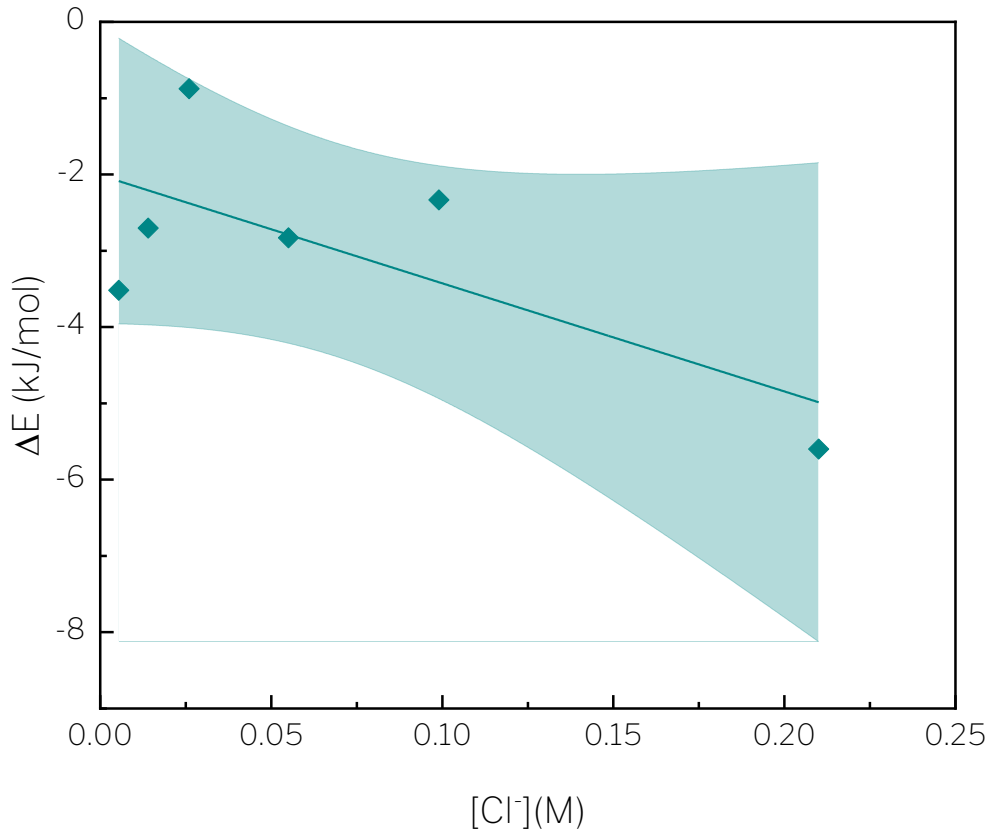

Figure 3-S5 ΔE values from the individual panels of Figure S3 plotted versus chloride concentration. The solid line is a linear least-squares fit used to determine whether a trend exists in ΔE across the NaCl concentration range of 0.0054 to 0.21 M. The 0.54 and 2.4 M solutions were excluded in this figure, as discussed in the main text. The shaded region represents the 95% confidence band for the linear fit. A linear regression t-test indicates that there is no statistically significant correlation between ΔE and chloride concentration at the 95% confidence level.

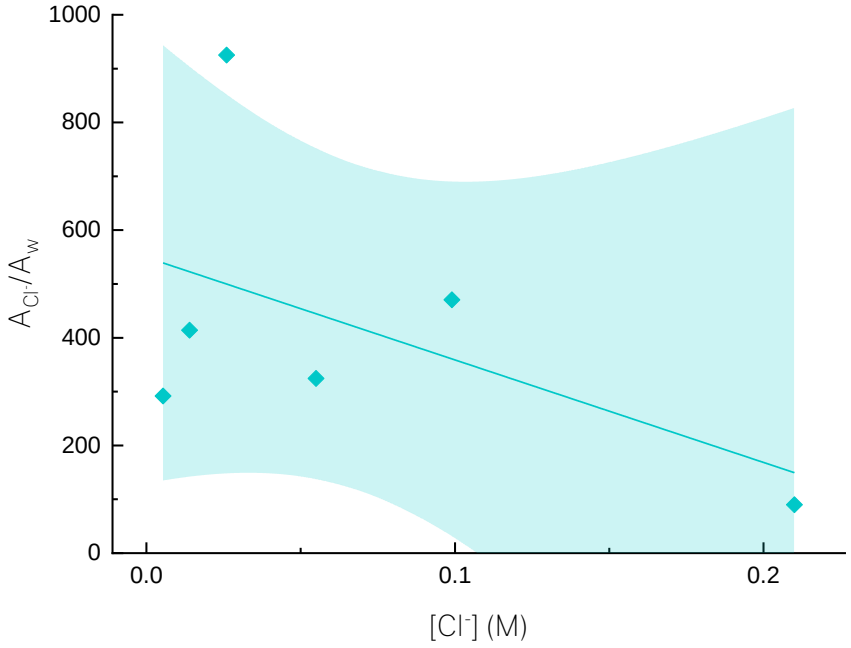

Figure 3-S6 A_{Cl^-}/A_w values determined from the intercepts of the individual panels in Figure 3.S3 plotted versus chloride concentration. The solid line is a linear least-squares fit used to determine whether a trend exists in A_{Cl^-}/A_w across the NaCl concentration range of 0.0054 to 0.21 M. The 0.54 and 2.4 M solutions were excluded in this figure, as discussed in the main text. The shaded region represents the 95% confidence band for the linear fit. A linear regression t-test indicates that there is no statistically significant correlation between A_{Cl^-}/A_w and chloride concentration at the 95% confidence level.

Table 3.S4 Averaged values from Table 3.1 and Table 3.2 in the main text excluding the 0.21 M data

Quantity	Value
$(\Phi\ (5\ °C) / \Phi\ (25\ °C))_{fit}$	1.05 ± 0.04
k_{Cl^-}/k_w (5 °C)	1310 ± 80
k_{Cl^-}/k_w (10 °C)	1250 ± 70
k_{Cl^-}/k_w (15 °C)	1220 ± 70
k_{Cl^-}/k_w (20 °C)	1230 ± 80
k_{Cl^-}/k_w (25 °C)	1210 ± 80
$(k_{Cl^-}/k_w\ (5\ °C) / k_{Cl^-}/k_w\ (25\ °C))_{fit}$	1.07 ± 0.03
ΔE	-2.4 ± 1.1
A_{Cl^-}/A_w	400^{+300}_{-200}

3.9.2 Flow Reactor Details – $ClNO_2$ Project

Figure 3.S7 shows schematic drawings of the Teflon solution holders utilized in this study. The N_2O_5 containing gas stream enters from one end at ~1 LPM (liter per minute) and is mixed as it passes over the internal barrier before passing over and reacting with the solution contained in the middle section of the solution holder. The gas mixing barrier also serves to contain the solution and prevent it from entering the gas flow tubing. These solution holders were contained within a temperature-controlled aluminum block regulated by a laboratory chiller.

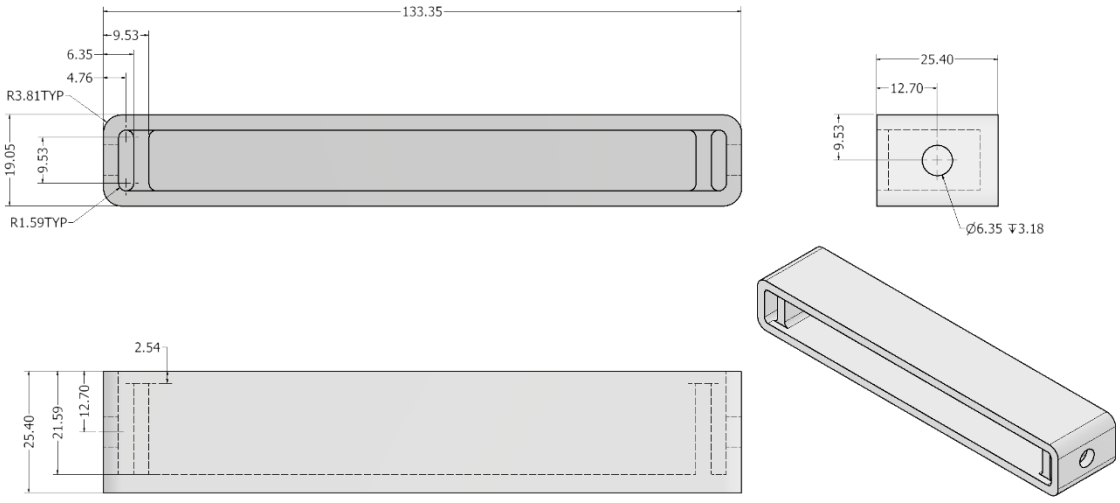

Figure 3-S7 Schematic drawings of the Teflon solution holders used in this study. All dimensions are given in mm.

3.9.3 Molecular Dynamics Methods

The local solvation structure of N_2O_5 and Cl^- were investigated by means of molecular dynamics simulation. We modeled the solvation environment with a cubic box of length 24.8 Å, which contained 1 N_2O_5 molecule and 1 Cl^- ion dissolved in 512 water molecules. Periodic boundary conditions were applied in all directions. The equation of motion was integrated by velocity-Verlet algorithm with time step of $0.5\ fs$, with the temperature fixed to $300\ K$ using a Langevin thermostat. Molecular dynamics simulation was performed for $1\ ns$ to equilibrate the system, and the radial distribution function was computed by additional $2\ ns$ of simulation starting from equilibrium state. All molecular dynamics simulations were performed in LAMMPS.[1]

The potential energy surface of the system was constructed by optimized point charge models of N_2O_5 and Cl^-. We modeled N_2O_5 by modifying the generalized AMBER force field which consisted of Lennard-Jones models of the dispersive interaction and point charges (GAFF).[2] The Lennard-Jones and short-ranged Coulomb interaction were cut off at 12 Å. Long-range Coulomb interaction was evaluated in K-space with a particle-particle particle-mesh (PPPM) solver.[3] We determined the stable geometry of N_2O_5 (C_2 symmetry) with a range-separated hybrid density function, the generalized gradient density functional ωB97X-V[4] and DEF2-TZVPD[5] basis set. The equilibrium bond distances and angles were altered to match these quantum calculations, and the dihedral potential was replaced by fitting a rigid scan of dihedral angles from the optimized geometry. Optimized restrained electrostatic potential (RESP) charges[6] were assigned at the center of each atom in N_2O_5 dissolved in an implicit solvent of water, which was modeled by conductor-like polarizable continuum models (C-PCM).[7] We employed the SPC/fw water model,[8] and Lennard-Jones parameters between the oxygen and hetero-atoms of N_2O_5 were determined using arithmetic mixing rule as indicated in **Table 3.S5**. The interaction between Cl^- and SPC-type water model was taken from Reference.[9] All quantum calculations were performed with QCHEM software.[10]

Table 3.S5 Atom-centered partial charges and Lennard-Jones parameter used for model N_2O_5 and Cl^-. Lennard-Jones parameters are mixed by arithmetic rule.

Atom	q(e)	ε(kcal/mol)	σ(Å)
N	+0.7111	0.1700	3.245
O(Center)	-0.2804	0.1700	3.000
O	-2.855	0.2100	2.960
Cl^-	-1.000	0.0066	5.029

3.9.4 Supporting Information References

(1) Thompson, A. P.; Aktulga, H. M.; Berger, R.; Bolintineanu, D. S.; Brown, W. M.; Crozier, P. S.; in 't Veld, P. J.; Kohlmeyer, A.; Moore, S. G.; Nguyen, T. D.; Shan, R.; Stevens, M. J.; Tranchida, J.; Trott, C.; Plimpton, S. J. LAMMPS - a Flexible Simulation Tool for Particle-Based Materials Modeling at the Atomic, Meso, and Continuum Scales. *Comput. Phys. Commun.* **2022**, *271*, 108171. https://doi.org/10.1016/j.cpc.2021.108171.

(2) Wang, J.; Wolf, R. M.; Caldwell, J. W.; Kollman, P. A.; Case, D. A. Development and Testing of a General Amber Force Field. *J. Comput. Chem.* **2004**, *25* (9), 1157–1174. https://doi.org/10.1002/jcc.20035.

(3) Hockney, R. W.; Eastwood, J. W. The Particle-Mesh Force Calculation. In *Computer Simulation Using Particles*; Bristol: Hilger, 1988; pp 120–165.

(4) Mardirossian, N.; Head-Gordon, M. ΩB97X-V: A 10-Parameter, Range-Separated Hybrid, Generalized Gradient Approximation Density Functional with Nonlocal Correlation, Designed by a Survival-of-the-Fittest Strategy. *Phys. Chem. Chem. Phys.* **2014**, *16* (21), 9904–9924. https://doi.org/10.1039/C3CP54374A.

(5) Weigend, F.; Ahlrichs, R. Balanced Basis Sets of Split Valence, Triple Zeta Valence and Quadruple Zeta Valence Quality for H to Rn: Design and Assessment of Accuracy. *Phys. Chem. Chem. Phys.* **2005**, *7* (18), 3297–3305. https://doi.org/10.1039/B508541A.

(6) Cornell, W. D.; Cieplak, P.; Bayly, C. I.; Kollman, P. A. Application of RESP Charges to Calculate Conformational Energies, Hydrogen Bond Energies, and Free Energies of Solvation. *J. Am. Chem. Soc.* **1993**, *115* (21), 9620–9631. https://doi.org/10.1021/ja00074a030.

(7) Barone, V.; Cossi, M. Quantum Calculation of Molecular Energies and Energy Gradients

in Solution by a Conductor Solvent Model. *J. Phys. Chem. A* **1998**, *102* (11), 1995–2001. https://doi.org/10.1021/jp9716997.

(8) Wu, Y.; Tepper, H. L.; Voth, G. A. Flexible Simple Point-Charge Water Model with Improved Liquid-State Properties. *J. Chem. Phys.* **2006**, *124* (2), 024503. https://doi.org/10.1063/1.2136877.

(9) Yagasaki, T.; Matsumoto, M.; Tanaka, H. Lennard-Jones Parameters Determined to Reproduce the Solubility of NaCl and KCl in SPC/E, TIP3P, and TIP4P/2005 Water. *J. Chem. Theory Comput.* **2020**, *16* (4), 2460–2473. https://doi.org/10.1021/acs.jctc.9b00941.

(10) Shao, Y.; Gan, Z.; Epifanovsky, E.; Gilbert, A. T. B.; Wormit, M.; Kussmann, J.; Lange, A. W.; Behn, A.; Deng, J.; Feng, X.; Ghosh, D.; Goldey, M.; Horn, P. R.; Jacobson, L. D.; Kaliman, I.; Khaliullin, R. Z.; Kuś, T.; Landau, A.; Liu, J.; Proynov, E. I.; Rhee, Y. M.; Richard, R. M.; Rohrdanz, M. A.; Steele, R. P.; Sundstrom, E. J.; Woodcock, H. L.; Zimmerman, P. M.; Zuev, D.; Albrecht, B.; Alguire, E.; Austin, B.; Beran, G. J. O.; Bernard, Y. A.; Berquist, E.; Brandhorst, K.; Bravaya, K. B.; Brown, S. T.; Casanova, D.; Chang, C.-M.; Chen, Y.; Chien, S. H.; Closser, K. D.; Crittenden, D. L.; Diedenhofen, M.; DiStasio, R. A.; Do, H.; Dutoi, A. D.; Edgar, R. G.; Fatehi, S.; Fusti-Molnar, L.; Ghysels, A.; Golubeva-Zadorozhnaya, A.; Gomes, J.; Hanson-Heine, M. W. D.; Harbach, P. H. P.; Hauser, A. W.; Hohenstein, E. G.; Holden, Z. C.; Jagau, T.-C.; Ji, H.; Kaduk, B.; Khistyaev, K.; Kim, J.; Kim, J.; King, R. A.; Klunzinger, P.; Kosenkov, D.; Kowalczyk, T.; Krauter, C. M.; Lao, K. U.; Laurent, A. D.; Lawler, K. V.; Levchenko, S. V.; Lin, C. Y.; Liu, F.; Livshits, E.; Lochan, R. C.; Luenser, A.; Manohar, P.; Manzer, S. F.; Mao, S.-P.; Mardirossian, N.; Marenich, A. V.; Maurer, S. A.; Mayhall, N. J.; Neuscamman, E.; Oana, C. M.; Olivares-Amaya, R.; O'Neill, D. P.; Parkhill, J. A.; Perrine, T. M.; Peverati, R.; Prociuk, A.; Rehn, D. R.; Rosta, E.; Russ, N. J.; Sharada, S. M.; Sharma, S.; Small, D. W.; Sodt, A.; Stein, T.; Stück, D.; Su, Y.-C.; Thom, A. J. W.; Tsuchimochi, T.; Vanovschi, V.; Vogt, L.; Vydrov, O.; Wang, T.; Watson, M. A.; Wenzel, J.; White, A.; Williams, C. F.; Yang, J.; Yeganeh, S.; Yost, S. R.; You, Z.-Q.; Zhang, I. Y.; Zhang, X.; Zhao, Y.; Brooks, B. R.; Chan, G. K. L.; Chipman, D. M.; Cramer, C. J.; Goddard, W. A.; Gordon, M. S.; Hehre, W. J.; Klamt, A.; Schaefer, H. F.; Schmidt, M. W.; Sherrill, C. D.; Truhlar, D. G.; Warshel, A.; Xu, X.; Aspuru-Guzik, A.; Baer, R.; Bell, A. T.; Besley, N. A.; Chai, J.-D.; Dreuw, A.; Dunietz, B. D.; Furlani, T. R.; Gwaltney, S. R.; Hsu, C.-P.; Jung, Y.; Kong, J.; Lambrecht, D. S.; Liang, W.;

Ochsenfeld, C.; Rassolov, V. A.; Slipchenko, L. V.; Subotnik, J. E.; Van Voorhis, T.; Herbert, J. M.; Krylov, A. I.; Gill, P. M. W.; Head-Gordon, M. Advances in Molecular Quantum Chemistry Contained in the Q-Chem 4 Program Package. *Mol. Phys.* **2015**, *113* (2), 184–215. https://doi.org/10.1080/00268976.2014.952696.

Chapter 4. Heterogeneous reaction of N_2O_5 with nitrate and chloride containing solutions: Isotopic evidence for the nitration of N_2O_5

This project will be submitted to the ACS Journal of Physical Chemistry A for publication. We have worked on this project with collaborators at University of California-Irvine: Manabu Shiraiwa and Pascale Lakey.

4.1 Abstract

Nitrate (NO_3^-) has been shown to suppress the reactive uptake of dinitrogen pentoxide (N_2O_5) to aqueous aerosol, yet a molecular mechanism that explains this effect has remained elusive. To verify a chemical reaction of N_2O_5 with NO_3^-, we used isotopically labeled $^{15}NO_3^-$ in the presence of Cl^- to mark N_2O_5 that reacted with $^{15}NO_3^-$. We determined the relative rates of exchange of isotopically labeled $^{15}NO_3^-$ with N_2O_5 in aqueous solutions containing $Na^{15}NO_3$ and NaCl through the production of $Cl^{14}NO_2$ and $Cl^{15}NO_2$. At three $Na^{15}NO_3$ concentrations (0.47, 1.35, and 3.7 M), the $Cl^{14}NO_2$ and $Cl^{15}NO_2$ products were measured as the NaCl concentration was increased from 0 to 3 M. Using a box model to compare the competition of chlorination and nitration reactions with N_2O_5, the rate constant ratio k_{Cl^-}/k_{NO3^-} was determined to be between 3.6 and 6.2 for the three $^{15}NO_3^-$ concentration regimes. Even at 3 M Cl^-, $Cl^{15}NO_2$ was detected at all $^{15}NO_3^-$ concentrations. This observation indicates that nitrate exchange still occurs even with high favorability towards chlorination. Model results further suggest the initial adsorption of a $^{14,14}N_2O_5$ molecule produces a majority of the measured $Cl^{15}NO_2$ from solution, rather than multiple events of adsorption and evaporation.

4.2 Introduction

Reactive uptake to aqueous aerosol is the primary loss process for dinitrogen pentoxide (N_2O_5) and a nocturnal sink for NO_x ($NO_x \equiv NO + NO_2$). This loss of NO_x lowers tropospheric

ozone (O_3) concentrations,[1] subsequently reducing the hydroxyl radical concentration and increasing the lifetime of organic species such as methane.[2] N_2O_5 can undergo several reaction pathways depending on the aerosol composition, such as hydrolysis to form nitric acid (HNO_3) and chlorination to form nitryl chloride ($ClNO_2$)[1,3]. The hydrolysis pathway leads to nitrification of aerosol and is a major component of aerosol formation and growth.[4,5] The chlorination pathway to form $ClNO_2$ has further implications for air quality as $ClNO_2$ evaporates from aerosol, and photolyzes into Cl radicals, which also impact tropospheric ozone and OH concentrations.[6,7] The probability that a N_2O_5 will collide and react with an aerosol to form either product is called the reactive uptake coefficient. Two major constituents that reduce the reactive uptake of N_2O_5 are organic films on aerosol particles[8] and high (>1 M) concentrations of nitrate (NO_3^-)[9].

The "nitrate effect" is the reduced reactive uptake of N_2O_5 at higher concentrations of NO_3^-.[9,10] This phenomenon is seen in laboratory experiments[9–11] and field measurements.[12,13] Bertram and Thornton found that NO_3^- did not appear to lower the uptake coefficient until concentrations reached 0.5 - 1 M, and at saturated concentrations (nearing 7 M) the uptake decreases to ~0.005, about a factor of 6 lower from pure water.[9] Wahner et al. found a more significant decrease in the uptake in very concentrated $NaNO_3$ aerosol, particles at 50% and 60% relative humidity and 17.5 and 27.5 molal of $NaNO_3$ had measured uptakes of 0.0018 and 0.0032 respectively.[11]

In previous studies, the more commonly presented mechanism for N_2O_5 involves a dissociation reaction of a solvated N_2O_5 molecule to form a nitrate NO_3^- anion and a nitronium cation NO_2^+ (R4.1, R4.2). NO_2^+ can react with H_2O to form another NO_3^- or react with other aqueous species, such as Cl^- to form $ClNO_2$ (R4.3, R4.4).

N_2O_5 (g) → N_2O_5 (aq) R4.1

N_2O_5 (aq) → $NO_2^+ + NO_3^-$ R4.2

$NO_2^+ + NO_3^-$ → N_2O_5 (aq) R4.-2

$NO_2^+ + H_2O$ → $2H^+ + NO_3^-$ R4.3

$NO_2^+ + Cl^-$ → $ClNO_2$ R4.4

This S_N1-type mechanism for N_2O_5 reactivity in water was first proposed by Mozurkewich and Calvert, based on prior research on N_2O_5 dissociating into ions in neat nitric acid.[14] The reaction pathways have been effective in explaining the measured kinetics from experiments. Here, the reactive uptake of N_2O_5 is controlled by the rate-limiting step R4.2 to form the reactive NO_2^+ ion. As a result, the uptake coefficient of N_2O_5 appears largely independent of the concentration of reactive partners, such as Cl^-. Several studies have measured the uptake of N_2O_5 to Cl^- containing aerosol or solutions and did not find a significant change in the uptake coefficient.[15–18] In this mechanism, the nitrate effect is explained by the recombination reaction of NO_3^- with a nitronium ion (NO_2^+) to reform N_2O_5 (R4.-2), leading to a reduction in the amount of N_2O_5 irreversibly lost to hydrolysis, chlorination, or other pathways. Interestingly, the addition of Cl^- to NO_3^- aerosol reverses the nitrate effect and returns the uptake coefficient back to ~0.03.[9]

However, recent computational studies have brought into question the presence of solvent-separated NO_2^+ and NO_3^- ions. In molecular dynamics simulations of N_2O_5 reacting with ions in water clusters, Karimova et al. did not find a solvent separated NO_2^+ species.[19] Rather, they find N_2O_5 existed as a contact ion pair, $NO_2^+NO_3^-$, with a nearby water molecule. Additional literature supports this species; Hirshberg et al. conducted MD-simulations, and found the $NO_2^+NO_3^-$ species had a fluctuating charge, with an average charge on each N group of

±0.21. Further, Galib and Limmer found an NO_2^+ species, in the form of $H_2ONO_2^+$ only existed transiently with an average lifetime of 4 picoseconds.[20] With a solvent separated NO_2^+ or $H_2ONO_2^+$ species unlikely to be the primary mechanism by which N_2O_5 reacts, an alternative mechanism is needed. One option would be to consider an S_N2 reaction. (R4.5 – 4.7).

$$N_2O_5\ (aq) + H_2O \rightarrow 2H^+ + 2\ NO_3^- \quad \text{R4.5}$$

$$N_2O_5\ (aq) + Cl^- \rightarrow ClNO_2 + NO_3^- \quad \text{R4.6}$$

$$N_2O_5\ (aq) + NO_3^- \rightarrow N_2O_5\ (aq) + NO_3^- \quad \text{R4.7}$$

However, in this mechanism, there is no apparent rate-limiting step of N_2O_5 reacting. As a result, increasing the concentration of Cl^- would increase the reactive uptake of N_2O_5. Previous studies have measured no effect of Cl^- on N_2O_5 uptake in the molar range.[16,17] Therefore, the reacting species of N_2O_5 would need to be at least partially intact and not fully separated, but requiring an activation step to form prior to reaction. The exact nature of this reactive species is difficult to verify experimentally, thus for the purposes of this study, we refer to the reactive N_2O_5 species as N_2O_5* (R4.8 – 4.10). This N_2O_5* species would still be a charge-fluctuating molecule or contact ion pair with a water molecule close by.

$$N_2O_5\ (aq) \rightarrow N_2O_5^*\ (aq) \quad \text{R4.8}$$

$$N_2O_5^*\ (aq) \rightarrow N_2O_5\ (aq) \quad \text{R4.-8}$$

$$N_2O_5^* + H_2O \rightarrow 2\ HNO_3 \quad \text{R4.9}$$

$$N_2O_5^* + Cl^- \rightarrow ClNO_2 + NO_3^- \quad \text{R4.10}$$

The N_2O_5* having an activation step and a deactivation step (R4.8 and 4.-8) could form a pre-equilibrium ratio, but for the purposes of a kinetic model, the two reactions create a steady state for N_2O_5*. A potential mechanism without a solvent-separated NO_2^+ reactive species for NO_3^- to recombine with, the role of nitrate in lowering N_2O_5 reactive uptake would need to be

understood. There are two possible explanations, a non-reactive interaction where the presence of NO_3^- reduces the ability of N_2O_5* to react or a chemical reaction of NO_3^- with the reactive $N_2O_5^*$ species. A reaction or interaction with nitrate would be a chemically null reaction but would "deactivate" the reactive N_2O_5* species into an inactivated N_2O_5 (aq) (R4.11):

$$N_2O_5^* + NO_3^- \rightarrow N_2O_5 + NO_3^- \quad \text{R4.11}$$

This deactivation would account for the nitrate effect on the uptake coefficient of N_2O_5. Verifying that R4.11 is a chemical exchange of a NO_3^- group would require separating the reactant and product N_2O_5 species.

Inspired by the work of Grzinic et al[21], we elected to use isotopically labeled $^{15}NO_3$ distinguish N_2O_5 molecules that did not exchange in solution and molecules that underwent a $^{15}NO_3$ exchange reaction to form $^{14,15}N_2O_5$ or $^{15,15}N_2O_5$ (R4.12 and 4.13).

$$^{14,14}N_2O_5^* + {}^{15}NO_3^- \rightarrow {}^{14,15}N_2O_5 + {}^{14}NO_3^- \quad \text{R4.12}$$

$$^{14,15}N_2O_5^* + {}^{15}NO_3^- \rightarrow {}^{15,15}N_2O_5 + {}^{14}NO_3^- \quad \text{R4.13}$$

Including the exchange of $^{15}NO_3^-$ results in three unique N_2O_5 species in solution: $^{14,14}N_2O_5$, $^{14,15}N_2O_5$, and $^{15,15}N_2O_5$. These species can undergo activation, R8, and further react with other solutes, such as Cl^- to form $Cl^{14}NO_2$ and $Cl^{15}NO_2$. (R4.14 – 4.16).

$$^{14,14}N_2O_5^* + Cl^- \rightarrow Cl^{14}NO_2 + {}^{14}NO_3^- \quad \text{R4.14}$$

$$^{14,15}N_2O_5^* + Cl^- \rightarrow \tfrac{1}{2}\, Cl^{14}NO_2 + \tfrac{1}{2}\, Cl^{15}NO_2 + \tfrac{1}{2}\, {}^{14}NO_3^- + \tfrac{1}{2}\, {}^{15}NO_3^- \quad \text{R4.15}$$

$$^{15,15}N_2O_5^* + Cl^- \rightarrow Cl^{15}NO_2 + {}^{15}NO_3^- \quad \text{R4.16}$$

This study aims to confirm the existence of an exchange reaction of $^{15}NO_3^-$ with the activated N_2O_5 species through the measurements of $Cl^{14}NO_2$ and $Cl^{15}NO_2$.

4.3 Experimental Procedure

The production of $^{14,15}N_2O_5$, $^{15,15}N_2O_5$, $Cl^{14}NO_2$ and $Cl^{15}NO_2$ was measured from the reaction of N_2O_5 with solutions of 0.47, 1.35, 3.7 M $Na^{15}NO_3$ containing variable concentrations

of additional NaCl (0 – 3 M). Our experiments were modeled on the procedures by Staudt et al 2019[22] and Kregel et al 2023[23]. N_2O_5 was produced *in situ* and the flow was alternated over mixed $Na^{15}NO_3$ / NaCl sample solutions and a saturated NaCl reference solution. This experiment was run at atmospheric pressure, resulting in a gas-phase diffusion limited regime. The calculation in Chapter 3 demonstrates the constraint from running experiments at atmospheric pressure. The frequency of reaction is controlled by the ability of an N_2O_5 molecule to diffuse to the surface rather than the uptake probability. Therefore, we measure and report the relative production of species from solution and not the reactive uptake of N_2O_5.

4.3.1 N_2O_5 Production

N_2O_5 was produced following a similar procedure to Bertram et al[24]. Ultra zero air (~20% O_2) (Airgas) and Ultra High purity N_2 (Airgas) flowed over potassium hydroxide pellets to ensure dry conditions before the gas mixture was illuminated with a mercury pen lamp (Jelight 95-2100-1) to produce O_3. The resulting $O_3/N_2/O_2$ gas mixture was combined with NO_2 balanced in N_2 (50 ppm, Airgas). The gas mixture was allowed to react in a darkened reaction vessel for approximately 100 seconds to produce N_2O_5. This gas mixture was then used for experiments in the flow reactor. The final concentrations of N_2O_5, O_3, NO_2, and NO_3 in the gas mixture when over the solutions are 6, 26, 241, 0.004 ppb. The O_3 concentration was measured using a Personal Ozone Monitor (2B Technologies). We calculated the concentration of N_2O_5 and NO_3 from known reaction kinetics and the measured initial concentrations of NO_2 and O_3.[25] Variations in the synthesis system, such as the temperature of the laboratory and minor changes in the flow rates of gas species, result in the actual N_2O_5 concentration having small fluctuations between days. Since the product yields involve the relative production of species, the absolute concentration of initial N_2O_5 did not affect the results.

4.3.2 Flow Reactor Setup

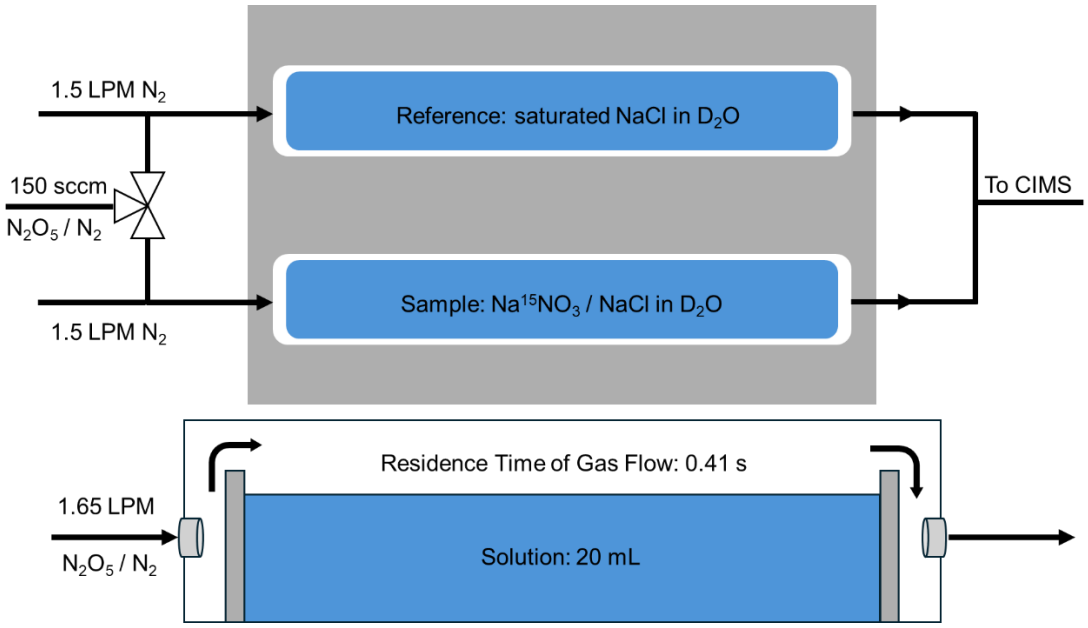

Figure 4-1 Depiction of the flow reactor setup and a sideview of one of the Teflon vessels containing solution (B). A flow of 150 cm^3/min (sccm) of N_2O_5 in N_2 was mixed with an additional 1.5 L/min (LPM) flow of N_2 carrier flow over the solutions. This gas flow was directed over 20 mL of a reference solution containing saturated NaCl in D_2O or a sample solution of variable $Na^{15}NO_3$ and NaCl in D_2O. The residence time of the gas over solution is 0.41 s. The resulting gas flow entered our chemical ionization mass spectrometer (CIMS). Details of the schematic are presented in Kregel et al and Chapter 2 of this thesis.

Experiments of N_2O_5 exchange with isotopically labeled $^{15}NO_3^-$ were performed in a lab-designed flow reactor system (Figure 4.1), detailed in Kregel et al.[23] A Teflon solution vessel contained solutions of 0.47, 1.35, and 3.7 M $Na^{15}NO_3$ (^{15}N 98%+, Cambridge Isotope Laboratories) with variable concentrations of 0 - 3M NaCl (EMD Milipore) in D_2O (99.9% D, Sigma-Aldrich). We used two solutions at the middle concentration range of $Na^{15}NO_3$ (1.33 M and 1.36 M). Due to their similar concentrations, we present their data together as 1.35 M $Na^{15}NO_3$. NaCl concentrations were achieved through serial addition of small aliquots of

concentrated NaCl solution to the solution vessel containing the $Na^{15}NO_3$ solution. A second Teflon solution vessel contained saturated NaCl in D_2O; this solution acted as a reference solution for complete conversion of N_2O_5 to $ClNO_2$ without the presence of $^{15}NO_3^-$. Both solutions were held at 20°C by a temperature-controlled chiller. The N_2O_5 gas flow was alternated between the two solution vessels by a computer-controlled switching valve, with the N_2O_5 flow active for 2 minutes for each pass over a solution. After 4 passes over each boat, the signals of each species of interest were averaged. It is important to note that D_2O from the boats evaporates during the course of an experiment. From previous tests, we estimate about 1 mL of D_2O is lost after several hours. However, as we are adding small aliquots of concentrated NaCl in D_2O, the net D_2O loss is likely mitigated.

4.3.3 Reactant and product detection

Species from the flow reactor were measured using a quadrupole mass spectrometer. We used chemical ionization with iodide-adduct (I^-) chemistry to detect the N_2O_5 and $ClNO_2$ species. The primary peaks of interest are $I(^{14,14}N_2O_5)^-$ (m/Q = 234.89), $I(^{14,15}N_2O_5)^-$ (m/Q = 235.88), $I(^{15,15}N_2O_5)^-$ (m/Q = 236.88), $I(^{35}Cl^{14}NO_2)^-$ (m/Q = 207.87), and $I(^{35}Cl^{15}NO_2)^-$ (m/Q = 208.86). Nitric acid is also detected in the mass spectrometer due to hydrolysis of N_2O_5 on wet tubing. Due to the mass peak overlap of $I(HNO3*H_2O)^-$ (m/Q = 207.91) with $I(^{35}Cl^{14}NO_2)^-$, all experiments were run in D_2O, which would push the nitric acid peak to $I(DNO_3*D_2O)^-$ (m/Q = 210.93). However, this peak would now overlap with $I(^{37}Cl^{15}NO_2)$ (m/Q = 210.86). As a result, our analysis focused only on the ^{35}Cl isotopes of $ClNO_2$ species, $^{35}Cl^{14}NO_2$ and $^{35}Cl^{15}NO_2$.

4.3.4 Kinetic Model

The model for determining the relative kinetic rates of reaction for N_2O_5 has been used in previous studies.[26,27] Briefly, the model consists of a 1-dimensional box with diffusion of species through a gas phase, liquid bulk phase, and surface accommodation, adsorption, and desorption

at the interface. The gas and bulk phases are separated into multiple layers to determine the diffusion of species towards and away from the surface. Further details on the specific parameters, including reaction rate constants, for the model are presented in the supporting information (Figure 4.S1, Table 4.S1, Table 4.S2). Additionally, we share an interrogation of the model to determine is certain physical aspects of our experimental setup, such as the boundary layer thickness in our reactor cell, could have impacted the production of isotopically labeled species. (Figure 4.S2 and Figure 4.S3).

4.4 Results

Initial experiments intended to measure the production of $^{14,15}N_2O_5$ and $^{15,15}N_2O_5$ from reaction of $^{14,14}N_2O_5$ with a near-saturated 6.9 M $Na^{15}NO_3$ solution were conducted. The size of the $I(^{14,15}N_2O_5)^-$ peak does increase when sampling gas flow from the $Na^{15}NO_3$ solution, about double the signal counts relative to N_2O_5 flow over NaCl solution with no $^{15}NO_3^-$ (Figure 4.2A). However, the signals of $^{14,15}N_2O_5$ and $^{15,15}N_2O_5$ shown in Figure 2A are miniscule relative to the size of the $^{14,14}N_2O_5$ peak, with $^{15,15}N_2O_5$ being nearly equal to the reference solution of 4.6 M NaCl. The small peaks at $I(^{14,15}N_2O_5)^-$ and $I(^{15,15}N_2O_5)^-$ over the NaCl solution may be due to the natural abundance of isotopes in our N_2O_5 gas flow. The natural abundance of ^{15}N (0.4%), ^{17}O (0.04%), and ^{18}O (0.2%) in our N_2O_5 source would have about 1% of the initial signal at m/Q + 1 and 1% of the initial signal at m/Q + 2. The peaks at $I(^{14,15}N_2O_5)^-$ and $I(^{15,15}N_2O_5)^-$ over the NaCl solution appear to match this 1% signal count relative to the $I(^{14,14}N_2O_5)$ signal, thus the natural abundance of isotopes in our initial N_2O_5 flow can explain the peaks.

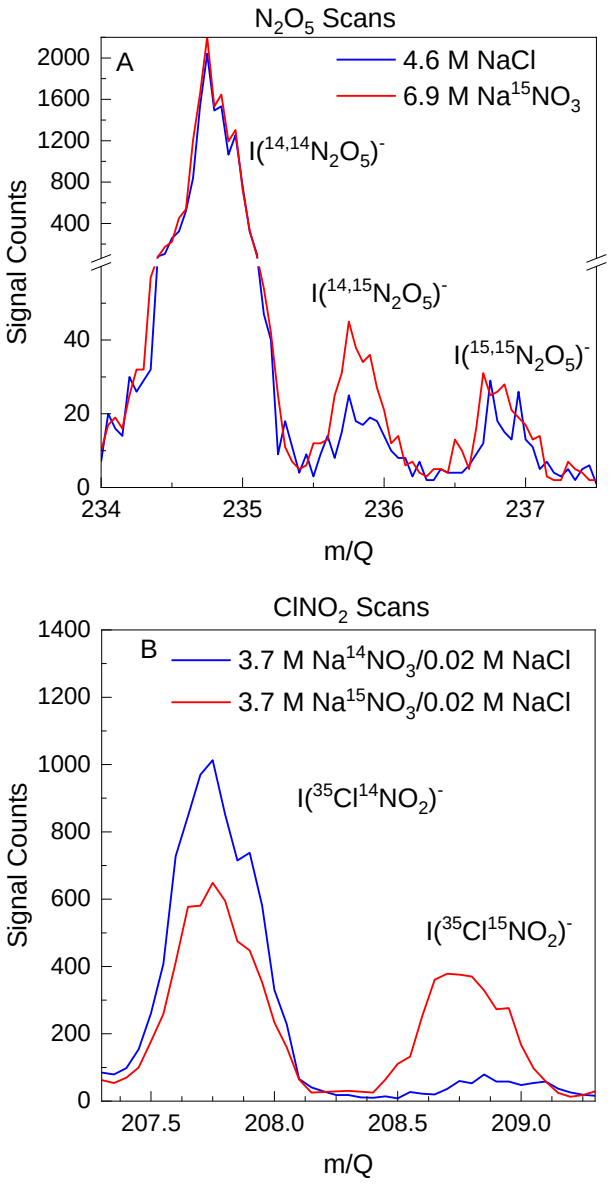

Figure 4-2 Mass scan of the N_2O_5 species from flowing N_2O_5 over 6.9 M $Na^{15}NO_3$ in D_2O (red) and 4.6 M NaCl in D_2O (blue) (Panel A). Panel B displays a mass scan of the $ClNO_2$ species from flowing N_2O_5 over mixed 3.7 M $Na^{14}NO_3$ / 0.02 M NaCl in D_2O (blue) and mixed 3.7 M $Na^{15}NO_3$ / 0.02 M NaCl in D_2O (red)

As the $^{14,15}N_2O_5$ and $^{15,15}N_2O_5$ signals were low from the near-saturation 6.9 M $Na^{15}NO_3$ solution, we anticipated experiments at lower $Na^{15}NO_3$ concentrations to not be viable. We chose instead to add NaCl to solutions containing $Na^{15}NO_3$ to produce $Cl^{14}NO_2$ and $Cl^{15}NO_2$. $ClNO_2$ is a fairly inert species ($k_{ClNO2 + H2O}$ = 270 s^{-1}) and has low solubility in aqueous solution (H = 0.024

M atm^{-1})[17], making this molecule a "sink" for reacted N_2O_5 in solution. Addition of NaCl to 3.7 M $Na^{15}NO_3$ solutions containing labeled $Na^{15}NO_3$ results in the production of both $Cl^{14}NO_2$ and $Cl^{15}NO_2$, whereas the solution of NaCl and $Na^{14}NO_3$ only generated significant amounts of $Cl^{14}NO_2$ (Figure 4.2B). The presence of $Cl^{15}NO_2$ confirms that N_2O_5 undergoes a chemical exchange with a $^{15}NO_3^-$ ion in solution. The observation of $Cl^{15}NO_2$ is common to all solutions investigated here and is a key conclusion of our studies.

4.4.1 Time Series of Signals

In our experiments, we measured the signals of $I(^{14,15}N_2O_5)^-$, $I(^{15,15}N_2O_5)^-$, $I(Cl^{14}NO_2)^-$, and $I(Cl^{15}NO_2)^-$. The signal of $I(^{14,15}N_2O_5)^-$ species from the 3.7 M $Na^{15}NO_3$ / 0.02 M NaCl solution appeared distinguishable from the reference solution signal of the natural abundance of $^{14,15}N_2O_5$ (Panel 4.3A). Performing a Two-Sample Student's T Test on this plot, we calculate a T statistic of 28.3, which is larger than the t value for significance for 240 degrees of freedom at 95% confidence (t = 1.97), verifying the signals of $I(^{14,15}N_2O_5)^-$ from the different solutions are statistically different. The signal for $I(^{15,15}N_2O_5)^-$ from the same solution has a smaller visual difference (Panel 4.3B). Performing the same statistics test results in a T statistic of 10.5, which also indicates the signal is statistically different between the two solutions. Panels 4.3D and 4.3E show the $I(^{14,15}N_2O_5)^-$ and $I(^{15,15}N_2O_5)^-$ signals from flow over the solution of 0.47 M $Na^{15}NO_3$ / 0.1 M NaCl and the reference solution, with a smaller magnitude in the signals as well as a smaller difference between the solutions. However, performing the statistics test on $I(^{15,15}N_2O_5)^-$ on Panel 4.3E results in a T statistic of 5.6, which is still greater than the t value for 95% confidence (t = 1.97), indicating there is a statistically significant difference in the signal of

I($^{15,15}N_2O_5$)$^-$ between the two solutions. We believe this is largely due to the sample size of 120 data point of signals for both solutions.

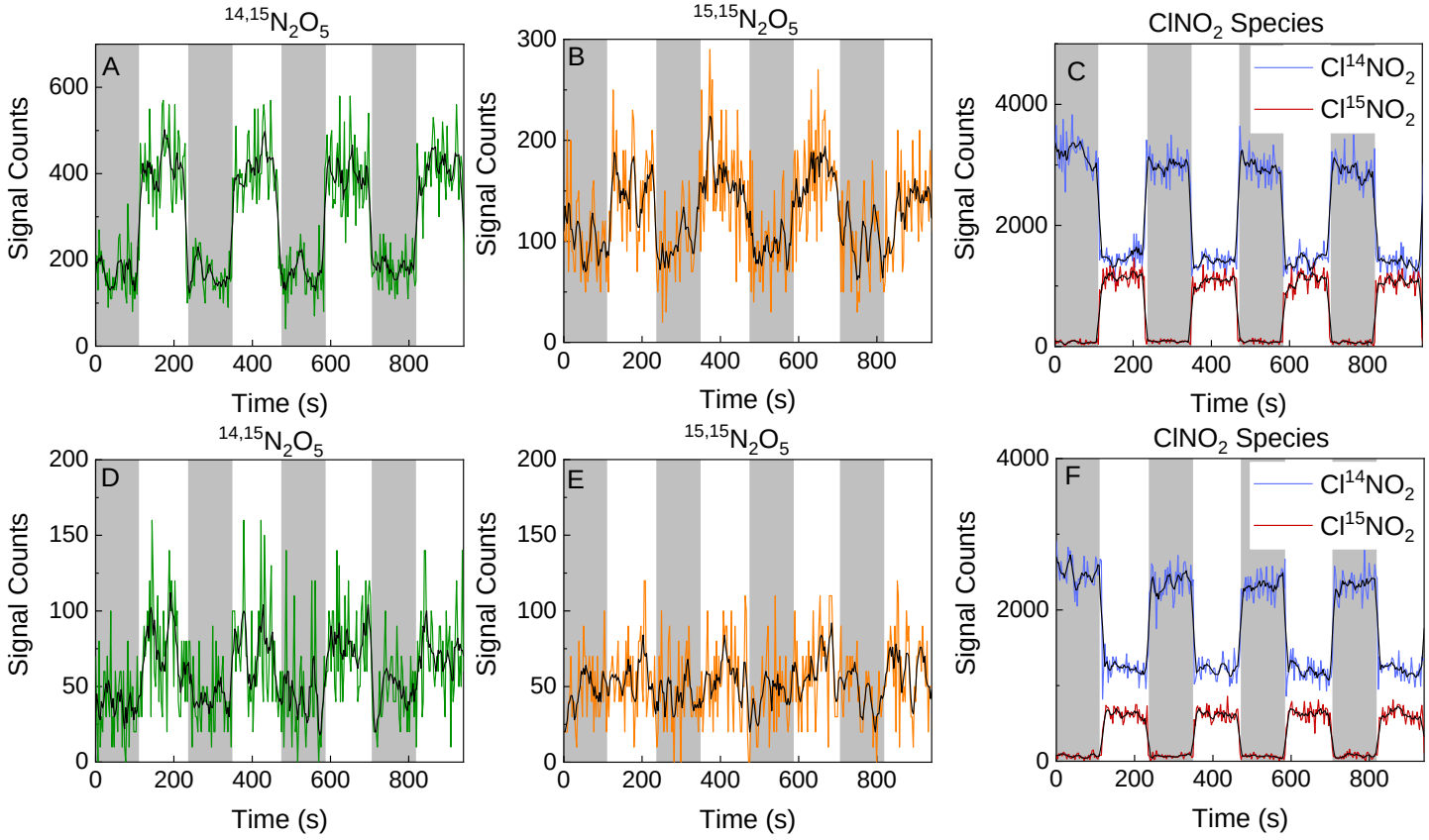

Figure 4-3 Top row shows the time series of the signal counts of $^{14,15}N_2O_5$ (A), $^{15,15}N_2O_5$ (B), and $Cl^{14}NO_2$ and $Cl^{15}NO_2$ (C) when N_2O_5 gas flow is alternated over saturated NaCl in D_2O (gray area) and 3.7 M $Na^{15}NO_3$ / 0.02 M NaCl in D_2O (white area). Bottom row shows the time series of the signal counts of $^{14,15}N_2O_5$ (D), $^{15,15}N_2O_5$ (E), and $Cl^{14}NO_2$ and $Cl^{15}NO_2$ (F) when N_2O_5 gas flow is alternated over saturated NaCl in D_2O (gray area) and 0.47 M $Na^{15}NO_3$ / 0.1 M NaCl in D_2O (white area). The solid black line is the 5 point moving average for each species.

Figures 4.3C and 4.3F show a time series of the $Cl^{14}NO_2$ and $Cl^{15}NO_2$ signals when N_2O_5 is alternated over the saturated NaCl reference solution and the mixed NaCl / $Na^{15}NO_3$ solutions. The sharp changes in the signal intensity reflect the fast response time of the system to switching the N_2O_5 flow between the solutions. The larger magnitude of signal from the $ClNO_2$ species

compared to the $^{14,15}N_2O_5$ and $^{15,15}N_2O_5$ species reinforces our decision to reinforces our decision to measure the production of $Cl^{14}NO_2$ and $Cl^{15}NO_2$ to determine the nitrate exchange rate, despite the statistically significant production of $^{14,15}N_2O_5$ and $^{15,15}N_2O_5$.

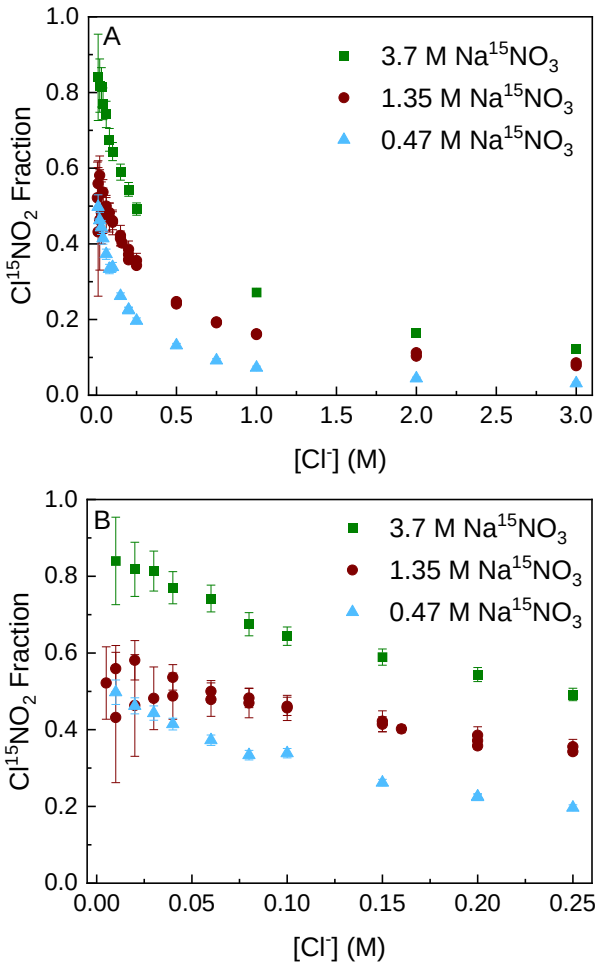

Figure 4-4 The $Cl^{15}NO_2$ fraction plotted against $[Cl^-]$ (A) and zoomed in on the low Cl^- concentrations (B) for different $^{15}NO_3^-$ concentrations (3.7, 1.35, 0.47 M). The $Cl^{15}NO_2$ fraction is defined as $Cl^{15}NO_2$ / ($Cl^{14}NO_2$ + $Cl^{15}NO_2$). The 1.35 M $Na^{15}NO_3$ data contain two separate runs of solutions of near equal concentration (1.33 M and 1.36 M). They are presented together, and the overlap indicates good reproducibility in our experiment. The error bars presented are the 95% confidence intervals, calculated from the propagated standard error of 120 data points for $Cl^{14}NO_2$ and $Cl^{15}NO_2$.

Figure 4.4 shows the change in the $Cl^{15}NO_2$ fraction as the concentration of Cl^- increases at 4 different $^{15}NO_3^-$ concentrations. We define the $Cl^{15}NO_2$ fraction as the proportion of total $ClNO_2$ produced that is $Cl^{15}NO_2$, $Cl^{15}NO_2$ / ($Cl^{14}NO_2$ + $Cl^{15}NO_2$). The close overlap of the 1.36 and 1.33 M $^{15}NO_3^-$ results indicates effective reproducibility in our experiment. Increasing the $^{15}NO_3^-$ concentration results in a higher fraction of $Cl^{15}NO_2$ in the system, which would come from more N_2O_5 exchanging with $^{15}NO_3^-$ in solution to form $^{14,15}N_2O_5$ and $^{15,15}N_2O_5$ before the species undergo chlorination to form $Cl^{14}NO_2$ and $Cl^{15}NO_2$. While we were unable to measure significant $^{15,15}N_2O_5$ signals in the CIMS, we argue the large $Cl^{15}NO_2$ fraction confirms the presence of $^{15,15}N_2O_5$ formed in solution. If no $^{15,15}N_2O_5$ was present in our system, then $Cl^{15}NO_2$ could only be formed from R7, $^{14,15}N_2O_5^* + Cl^- \rightarrow$ ½ $Cl^{14}NO_2$ + ½ $Cl^{15}NO_2$ + ½ $^{14}NO_3^-$ + ½ $^{15}NO_3^-$. If we assume every initial $^{14,14}N_2O_5$ undergoes exchange to form $^{14,15}N_2O_5$, then the maximum $Cl^{15}NO_2$ fraction possible would be 0.5. However, the experimental $Cl^{15}NO_2$ fraction measured goes above 0.5 for the 1.35, and 3.7 M $^{15}NO_3^-$ solutions, even reaching 0.8 ± 0.1 in the 3.7 M $^{15}NO_3^-$ solution. Considering we expect Cl^- to react at equivalent rates with $^{14,14}N_2O_5$, $^{14,15}N_2O_5$, and $^{15,15}N_2O_5$, the high $Cl^{15}NO_2$ fraction suggests a significant amount of $^{15}NO_3$ exchange with N_2O_5, even multiple $^{15}NO_3$ exchanges with the same initial N_2O_5 occurring in solution.

When increasing [Cl^-], the $Cl^{15}NO_2$ fraction decreases. The presence of more Cl^- results in more reactions of Cl^- with N_2O_5 and $^{14,15}N_2O_5$ before the species can undergo further $^{15}NO_3^-$ exchange. All solutions were tested at high Cl^- concentrations up to or near saturation, about [Cl^-] = 3 M. The $Cl^{15}NO_2$ fraction at [Cl^-] = 3 M and [$^{15}NO_3^-$] = 3.7 M reached 0.121 ± 0.005, indicating that even at near equal concentrations of Cl^- and $^{15}NO_3^-$, a significant amount of N_2O_5 still exchanged with $^{15}NO_3^-$ to form $^{14,15}N_2O_5$ and $^{15,15}N_2O_5$. The $Cl^{15}NO_2$ fraction at [Cl^-] = 3 M

and [$^{15}NO_3^-$] = 0.47 M reached 0.02 ± 0.003, revealing isotopically labelled N_2O_5 still is created in solution despite the high [Cl^-]/[$^{15}NO_3^-$] ratio of 6:1.

4.4.2 Modeled Experimental Results

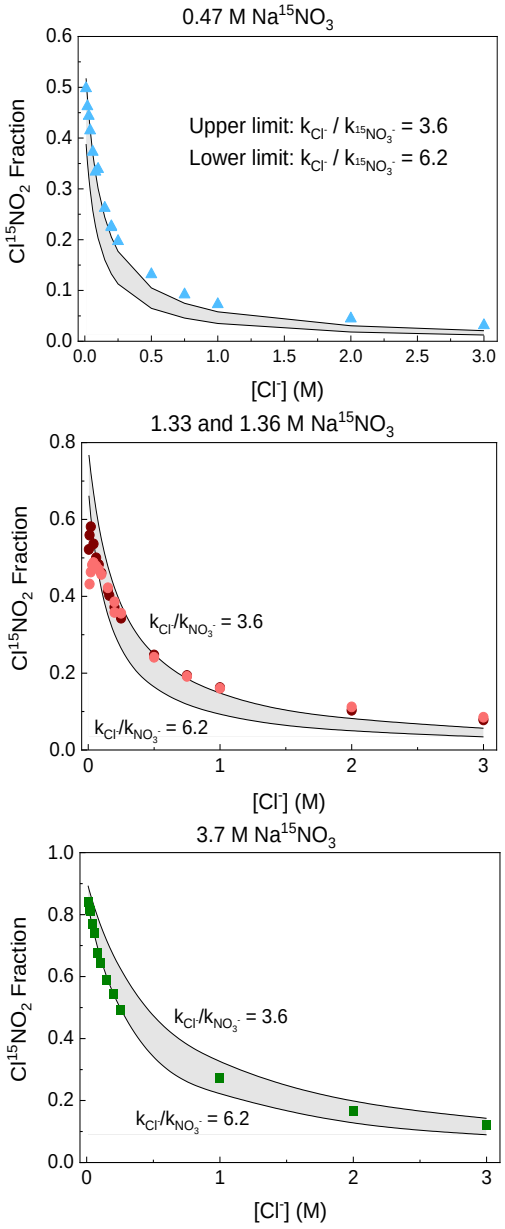

Figure 4-5 The modeled $Cl^{15}NO_2$ fraction with $k_{Cl^-}/k_{NO_3^-}$ = 3.6 (upper limit) and 6.2 (lower limit). Experimental $Cl^{15}NO_2$ fractions are overlayed on the modeled $Cl^{15}NO_2$, separated by $Na^{15}NO_3$ concentration.

Fitting the measured $Cl^{15}NO_2$ fraction to our kinetic diffusion model in Figure 4.5 predicts a k_{Cl^-}/k_{NO3^-} between 3.6 and 6.2 for the three nitrate concentration regimes with the k_{Cl^-} rate constant set at 8 x 10^8 $M^{-1}s^{-1}$, a rate constant derived in previous studies.[23,28] The 0.47 M $Na^{15}NO_3$ data fits to the higher end of the k_{Cl^-}/k_{NO3^-} range, whereas the higher 3.7 M $Na^{15}NO_3$ data has a lower k_{Cl^-}/k_{NO3^-} fit. This observation of the rate constant ratio decreasing at higher Cl^- concentration was also seen in Kregel et al, which found the k_{Cl^-}/k_{water} ratio decreased from 1240 ± 90 to 840 ± 50 between $[Cl^-]$ = 0.0054 M and 0.21 M, respectively. This behavior of the rate constant ratio decreasing at higher concentration of reactants was also measured in Kregel et al which found a decreasing k_{Cl^-}/k_{water} ratio as $[Cl^-]$ increased.[23] Interestingly, the model results fit the experimental data better at lower $[Cl^-]$ but at higher $[Cl^-]$ the model slightly underpredicts the $Cl^{15}NO_2$ fraction. One potential reason could be due to an increase in the interfacial concentration of NO_3^- at increasing Cl^-. Wingen et al presents MD simulation density profiles of ions in concentrated NaCl and $NaNO_3$, which suggest Cl^- pulls NO_3^- to the aqueous surface through the formation of a double layer with Na^+ ions.[29] Enhanced interfacial concentrations of $^{15}NO_3^-$ could lead to increased exchange to form $^{14,15}N_2O_5$ and $^{15,15}N_2O_5$ not accounted for in our kinetic model. Interestingly, MD simulations of concentrated $NaNO_3$ with no halide solutions found little interfacial apportionment of NO_3^-[29,30], suggesting Cl^- can potentially increase the amount of NO_3^- exchange with N_2O_5. This may explain the lack of $^{15}NO_3^-$ exchange detected in the mass scan 6.9 M $Na^{15}NO_3$ solution tested, where only a small peak of $^{14,15}N_2O_5$ was present with no noticeable $^{15,15}N_2O_5$. (Figure 4.2A). Interestingly, Li and Wang present a simulation of pure NaCl in water in which no double layer is visible.[31] It is possible the presence of multiple ions creates a double layer near the surface. If so, and Cl^- is slightly enhanced at the interface, we may be able to detect a greater production of $ClNO_2$ species.

4.4.3 Effect of adsorption of $^{14,15}N_2O_5$ and $^{15,15}N_2O_5$

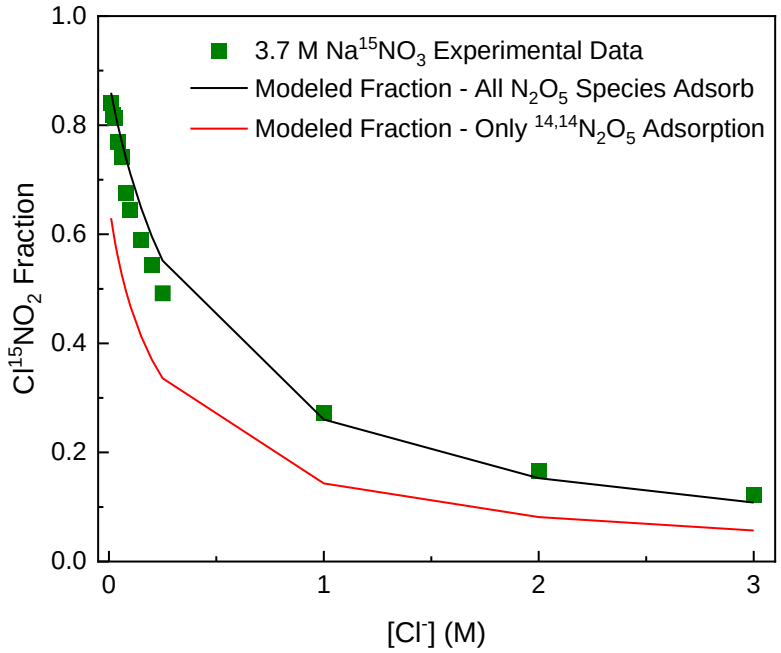

Figure 4-6. Plot of the $Cl^{15}NO_2$ fraction with 3.7 M $Na^{15}NO_3$, comparing the experimental data (green squares) with modeled results of all species allowed to adsorb to the solution (black line) and the modeled results when only the $^{14,14}N_2O_5$ species is allowed to adsorb and $^{14,15}N_2O_5$ and $^{15,15}N_2O_5$ cannot re-adsorb after leaving solution (red line).

To determine if an N_2O_5 molecule collides multiple times with the surface or if most reactivity occurs on the first collision, we modeled the effect of removing readsorption of labeled N_2O_5 produced in solution. Without readsorption, product species could only be formed from an incoming $^{14,14}N_2O_5$ molecule undergoing one or several reactions. The modeled $Cl^{15}NO_2$ fraction decreases between 18% at low Cl^- and 45% at high Cl^- when the adsorption of $^{14,15}N_2O_5$ and $^{15,15}N_2O_5$ is turned off (Figure 4.6). This indicates a majority of $Cl^{15}NO_2$ formed does not come from a $^{14,15}N_2O_5$ or $^{15,15}N_2O_5$ molecule leaving solution and then reentering to react with Cl^-, but rather a $^{14,14}N_2O_5$ molecule undergoing single or double exchange with $^{15}NO_3^-$ then chlorination in a single collision event without leaving solution.

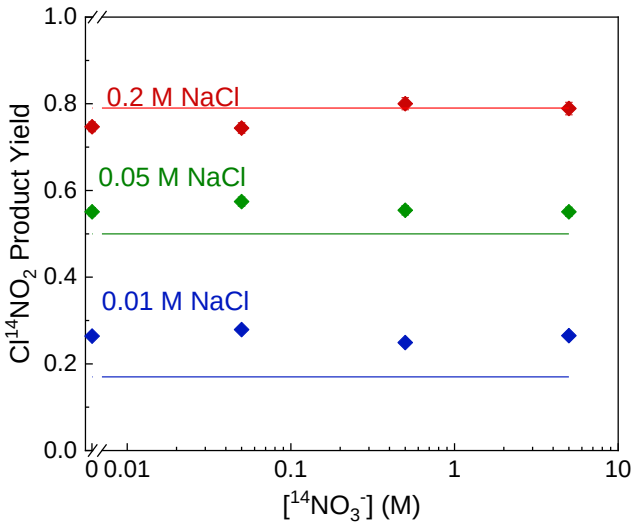

Figure 4-7 The $Cl^{14}NO_2$ product yield plotted against [$^{14}NO_3^-$] (0, 0.05, 0.5, and 5 M) at three different Cl^- concentrations (0.01, 0.05, 0.02 M). The solid lines are the $ClNO_2$ product yields predicted from our model for these 3 Cl^- concentrations.

Bertram and Thornton showed that the addition of Cl^- to NO_3^- reverses the nitrate effect and increases the uptake back to ~0.03.[24] To verify the potential competition between NO_3^- and Cl^-, as well as potential enhancement of Cl^- with NO_3^- present, we measured the product yield of $Cl^{14}NO_2$ at three different Cl^- concentrations (Figure 4.6). We use the same definition for product yield as Kregel et al:

$$ClNO2\ Product\ Yield = \frac{Signal\ ClNO_{2\,Sample}}{Signal\ ClNO_{2\,Reference}} \qquad \text{E4.1}$$

The reference solution, saturated NaCl in D_2O, corresponds to complete conversion of N_2O_5 to $ClNO_2$, thus the product yield is a measure of the competition between the chlorination pathway and hydrolysis pathway for N_2O_5. The $Cl^{14}NO_2$ product yield in Figure 4.7 does not change with the addition of NO_3^-, even at 5 M NO_3^-, indicating that the presence and exchange of nitrate with N_2O_5 does not affect the competition between chlorination and hydrolysis. NO_3^- could have no effect on either process or it could affect both processes equally. This contrasts with the effect of other ions on $ClNO_2$ production; the presence of acetate and sulfate has been shown to decrease

the fraction of $ClNO_2$ produced, suggesting those ions do compete with Cl^- for the reactive N_2O_5 species. However, the lack of an effect of the $ClNO_2$ production from NO_3^- suggests this ion behaves differently from sulfate or acetate.

4.4.4 Additional test for $ClNO_2$ Production

An additional experiment was conducted to verify that $Cl^{15}NO_2$ could not be formed through another pathway: $Cl^{14}NO_2 + {}^{15}NO_3^- \rightarrow Cl^{15}NO_2 + {}^{14}NO_3^-$. In this test, we bubbled N_2O_5 through a 5 M NaCl solution; the resulting gas flow from the bubbler had $ClNO_2$ present but no N_2O_5 detected, indicating that all N_2O_5 reacted in solution. The resulting $ClNO_2$ gas flow alternated over a concentrated $Na^{15}NO_3$ solution and a D_2O solution. We detected no difference in the $Cl^{15}NO_2$ signal between the two solutions, measuring average signals with standard deviations of 30 ± 20 over D_2O and 27 ± 19 over concentrated $Na^{15}NO_3$. This indicates that the reaction $Cl^{14}NO_2 + {}^{15}NO_3^- \rightarrow Cl^{15}NO_2 + {}^{14}NO_3^-$ does not occur at a significant enough rate to influence our results.

4.5 Discussion

Our detection of isotopically labeled ${}^{14,15}N_2O_5$, ${}^{15,15}N_2O_5$, and $Cl^{15}NO_2$ confirms a chemical exchange reaction occurs between N_2O_5 and aqueous ${}^{15}NO_3^-$. However, the exact mechanism by which this reaction occurs still remains unknown. The key aspects of N_2O_5 reactivity are the constant uptake coefficient independent of Cl^- concentration[15–17,32] and the product yield of $ClNO_2$ in competition with hydrolysis.[9,17,23] The studies that found lack of N_2O_5 uptake from Cl^- measured primarily in the 1 M to saturation range of solutions and aerosol. It is possible there is weak dependence on the uptake from Cl^-, perhaps at lower concentrations, but even so, the high favorability for chlorination, k_{Cl^-}/k_{water} would still indicate the chlorination reaction is held back by a rate-limiting activation step. As N_2O_5 uptake is impacted by the

relative humidity and the temperature of aerosol,[15] these factors would affect the rate-limiting activation step. This would support the argument of the contact ion pair species with the nearby water molecule, H_2O--$NO_2^{\delta+}NO_3^{\delta-}$.

Table 4.1. Summary of rate constant ratios of chlorination, hydrolysis, and nitration of N_2O_5, from this study and Kregel et al.[23]

Rate Constant Ratio	Value
k_{Cl^-}/k_w	1150 ± 90 (25°C)[23a]
k_{Cl^-}/k_{NO3^-}	3.6 – 6.2
k_{NO3^-}/k_w	190 - 320

a. k_{Cl^-}/kw value of 1150 ± 90 comes from the average of k_{Cl^-}/kw of solutions between 0.0054 and 0.21 M NaCl. This value drops to half as much at 0.54 M NaCl.

Table 4.1 compiles the reaction rate constants ratios of N_2O_5 with chlorination, nitration, and hydrolysis. The value for k_{NO3^-}/k_w was determined by using our modeled k_{Cl^-}/k_{NO3^-} value with the previously reported k_{Cl^-}/k_w by Kregel et al. Bertram and Thornton reported a larger k_{Cl^-}/k_{NO3^-} ratio of 29 ± 6,[24] however their result was derived from measuring the increase in $\gamma(N_2O_5)$ back to 0.03 as $[Cl^-]/[NO_3^-]$ increased. This is a different mechanism than our determination from products of a $^{15}NO_3^- + N_2O_5$ reaction instead of uptake. This difference may suggest the rate of reactive exchange between NO_3^- and N_2O_5 could have a different rate constant than the deactivation step (R4.11).

Finding the absolute rate constants for the reactions listed is difficult due to a rate-limiting activation step for N_2O_5 to form a reactive species prior to reaction with Cl^- and other ions. Many studies determined rate constant ratios through the suppression of $ClNO_2$ from the presence other ions.[22,23,33] The lower production of $ClNO_2$ found with SO_4^{2-} and acetate in solution contrasts with the lack of an effect from NO_3^-. This difference may arise from different

N_2O_5 reaction mechanisms. Sulfate and acetate are postulated to form the transient reaction intermediates $[NO_2SO_4]^-$ and CH_3COONO_2, which are then immediately attacked by water to lead to the hydrolysis products. In the case of NO_3^-, the reaction intermediate would simply be N_2O_5 itself before hydrolysis occurs and therefore this process constitutes a null reaction.

While Staudt et al claimed $k_{Cl-} = k_{SO4\ 2-} = k_{CH3COO-}$ due to all reactions being diffusion limited in the liquid phase, the product yields indicate they may have different reaction rates.[22] At equal molar bulk concentrations of Cl^- and SO_4^{2-}, and Cl^- and CH_3COO^-, the product yield of $ClNO_2$ is decreased to from 0.80 to 0.47 and 0.18 respectively, and these ions compete with Cl^- for the reactive N_2O_5 species. Starting from an initial product yield of 0.80 at 0.5 M NaCl prior to addition of SO_4^{2-} and CH_3COO^-, we can estimate the $k_{Cl-}/k_{SO4\ 2-} = \sim 1.5$, as 60% of the $ClNO_2$ yield remains. Conversely, the competition of Cl^- with CH_3COO^- appears to favor the organic anion, $k_{Cl-}/k_{CH3COO-} = \sim 0.3$, which could be due to more surface partitioning of the acetate ion. Based on surface tension values, Pegram and Record argue SO_4^{2-} is deeply in the bulk, Cl^- slightly disfavors the surface but is near neutral, and CH_3COO^- slightly favors surface accumulation.[34] Connecting the new rate constant ratios to k_{NO3-}, we get $k_{SO4\ 2-}/k_{NO3-} = 2.4 – 4.1$ and $k_{CH3COO-}/k_{NO3-} = 12 – 21$.

It is intriguing to think what the competition, if any, between NO_3^- and these two ions would appear as. If NO_3^- forms some transition state, such as $[NO_3NO_2NO_3]^-$, which could lengthen the lifetime of the reactive N_2O_5 species as it reduces uptake, then NO_3^- could compete with SO_4^{2-} and CH_3COO^-. Alternatively, NO_3^- can deactivate or react with the reactive N_2O_5* species, and simply reform N_2O_5, in which case NO_3^- may not affect the competition between Cl^- and SO_4^{2-} and acetate. However, there could be a depth dependence to the nitration reaction. Moon and Limmer determined a depth dependence in the chlorination reaction using molecular

dynamics simulations of an S_N2 mechanism, with k_{Cl^-} highest near the interface.[35] A similar behavior in k_{NO3^-} could impact the role of NO_3^- in the reactive exchange and reducing the reactive uptake coefficient of N_2O_5.

4.6 Conclusions

We have measured the production of isotopically labeled $^{14,15}N_2O_5$, $^{15,15}N_2O_5$, and $Cl^{15}NO_2$ from flowing N_2O_5 over solutions containing $Na^{15}NO_3$ and NaCl. Using the relative production of $Cl^{15}NO_2$ and $Cl^{14}NO_2$, we determined the rate constant ratio between N_2O_5 + $^{15}NO_3^-$ and N_2O_5 + Cl^- is k_{Cl^-}/k_{NO3^-} = 3.6 – 6.2 for solutions of 3.7 – 0.47 M $Na^{15}NO_3$ with [Cl^-] increasing from 0 to 3 M. With this confirmation of a chemical reaction, we attempt to bring together the various mechanisms people have predicted N_2O_5 reacts by. However, the presence of a chemical reaction of NO_3^- with N_2O_5 does not preclude other effects from anion reducing uptake. Measuring the uptake of N_2O_5 onto $^{15}NO_3^-$ solution or aerosol may provide deeper insights into the full behavior of NO_3^- and N_2O_5. If N_2O_5 uptake still decreases with high $^{15}NO_3^-$ concentrations, then that would confirm another process along with the direct chemical exchange is occurring.

4.7 References

(1) Brown, S. S.; Stutz, J. Nighttime Radical Observations and Chemistry. *Chem. Soc. Rev.* **2012**, *41* (19), 6405. https://doi.org/10.1039/c2cs35181a.

(2) MacIntyre, H. L.; Evans, M. J. Sensitivity of a Global Model to the Uptake of N2O5 by Tropospheric Aerosol. *Atmospheric Chem. Phys.* **2010**, *10* (15), 7409–7414. https://doi.org/10.5194/acp-10-7409-2010.

(3) Rossi, M. J. Heterogeneous Reactions on Salts. *Chem. Rev.* **2003**, *103* (12), 4823–4882. https://doi.org/10.1021/cr020507n.

(4) Yan, C.; Tham, Y. J.; Nie, W.; Xia, M.; Wang, H.; Guo, Y.; Ma, W.; Zhan, J.; Hua, C.; Li, Y.; Deng, C.; Li, Y.; Zheng, F.; Chen, X.; Li, Q.; Zhang, G.; Mahajan, A. S.; Cuevas, C. A.; Huang, D. D.; Wang, Z.; Sun, Y.; Saiz-Lopez, A.; Bianchi, F.; Kerminen, V.-M.; Worsnop, D. R.; Donahue, N. M.; Jiang, J.; Liu, Y.; Ding, A.; Kulmala, M. Increasing Contribution of Nighttime Nitrogen Chemistry to Wintertime Haze Formation in Beijing Observed during COVID-19 Lockdowns. *Nat. Geosci.* **2023**, *16* (11), 975–981. https://doi.org/10.1038/s41561-023-01285-1.

(5) Riemer, N.; Vogel, H.; Vogel, B.; Schell, B.; Ackermann, I.; Kessler, C.; Hass, H. Impact of the Heterogeneous Hydrolysis of N_2O_5 on Chemistry and Nitrate Aerosol Formation in the Lower Troposphere under Photosmog Conditions. *J. Geophys. Res. Atmospheres* **2003**, *108* (D4), 2002JD002436. https://doi.org/10.1029/2002JD002436.

(6) Simpson, W. R.; Brown, S. S.; Saiz-Lopez, A.; Thornton, J. A.; Von Glasow, R. Tropospheric Halogen Chemistry: Sources, Cycling, and Impacts. *Chem. Rev.* **2015**, *115* (10), 4035–4062. https://doi.org/10.1021/cr5006638.

(7) Sarwar, G.; Gantt, B.; Schwede, D.; Foley, K.; Mathur, R.; Saiz-Lopez, A. Impact of Enhanced Ozone Deposition and Halogen Chemistry on Tropospheric Ozone over the Northern Hemisphere. *Environ. Sci. Technol.* **2015**, *49* (15), 9203–9211. https://doi.org/10.1021/acs.est.5b01657.

(8) Thornton, J. A.; Abbatt, J. P. D. N_2O_5 Reaction on Submicron Sea Salt Aerosol: Kinetics, Products, and the Effect of Surface Active Organics. *J. Phys. Chem. A* **2005**, *109* (44), 10004–10012. https://doi.org/10.1021/jp054183t.

(9) Bertram, T. H.; Thornton, J. A. Toward a General Parameterization of N2O5 Reactivity on Aqueous Particles: The Competing Effects of Particle Liquid Water, Nitrate and Chloride. *Atmos Chem Phys* **2009**.

(10) Mentel, T. F.; Sohn, M.; Wahner, A. Nitrate Effect in the Heterogeneous Hydrolysis of Dinitrogen Pentoxide on Aqueous Aerosols.

(11) Wahner, A.; Mentel, T. F.; Sohn, M.; Stier, J. Heterogeneous Reaction of N_2O_5 on Sodium Nitrate Aerosol. *J. Geophys. Res. Atmospheres* **1998**, *103* (D23), 31103–31112. https://doi.org/10.1029/1998JD100022.

(12) Wang, Z.; Wang, W.; Tham, Y. J.; Li, Q.; Wang, H.; Wen, L.; Wang, X.; Wang, T. Fast Heterogeneous N2O5 Uptake and ClNO2 Production in Power Plant and Industrial Plumes Observed in the Nocturnal Residual Layer over the North China Plain. *Atmospheric Chem. Phys.* **2017**, *17* (20), 12361–12378. https://doi.org/10.5194/acp-17-12361-2017.

(13) McDuffie, E. E.; Fibiger, D. L.; Dubé, W. P.; Lopez-Hilfiker, F.; Lee, B. H.; Thornton, J. A.; Shah, V.; Jaeglé, L.; Guo, H.; Weber, R. J.; Michael Reeves, J.; Weinheimer, A. J.; Schroder, J. C.; Campuzano-Jost, P.; Jimenez, J. L.; Dibb, J. E.; Veres, P.; Ebben, C.; Sparks, T. L.; Wooldridge, P. J.; Cohen, R. C.; Hornbrook, R. S.; Apel, E. C.; Campos, T.; Hall, S. R.; Ullmann, K.; Brown, S. S. Heterogeneous N2O5 Uptake During Winter: Aircraft Measurements During the 2015 WINTER Campaign and Critical Evaluation of Current Parameterizations. *J. Geophys. Res. Atmospheres* **2018**, *123* (8), 4345–4372. https://doi.org/10.1002/2018JD028336.

(14) Mozurkewich, M.; Calvert, J. G. Reaction Probability of N_2O_5 on Aqueous Aerosols. *J. Geophys. Res. Atmospheres* **1988**, *93* (D12), 15889–15896. https://doi.org/10.1029/JD093iD12p15889.

(15) Van Doren, J. M.; Watson, L. R.; Davidovits, Paul.; Worsnop, D. R.; Zahniser, M. S.; Kolb, C. E. Temperature Dependence of the Uptake Coefficients of Nitric Acid, Hydrochloric Acid and Nitrogen Oxide (N2O5) by Water Droplets. *J. Phys. Chem.* **1990**, *94* (8), 3265–3269. https://doi.org/10.1021/j100371a009.

(16) Stewart, D. J.; Griffiths, P. T.; Cox, R. A. Reactive Uptake Coefficients for Heterogeneous Reaction of N2O5 with Submicron Aerosols of NaCl and Natural Sea Salt. *Atmospheric Chem. Phys.* **2004**, *4* (5), 1381–1388. https://doi.org/10.5194/acp-4-1381-2004.

(17) Behnke, W.; George, C.; Scheer, V.; Zetzsch, C. Production and Decay of ClNO2 from the Reaction of Gaseous N2O5 with NaCl Solution: Bulk and Aerosol Experiments. *J. Geophys. Res. Atmospheres* **1997**, *102* (3), 3795–3804. https://doi.org/10.1029/96jd03057.

(18) George, C.; Ponche, J. L.; Mirabel, P.; Behnke, W.; Scheer, V.; Zetzsch, C. Study of the Uptake of N2O5 by Water and NaCl Solutions. *J. Phys. Chem.* **1994**, *98* (35), 8780–8784. https://doi.org/10.1021/j100086a031.

(19) Karimova, N. V.; Chen, J.; Gord, J. R.; Staudt, S.; Bertram, T. H.; Nathanson, G. M.; Gerber, R. B. SN2 Reactions of N2O5 with Ions in Water: Microscopic Mechanisms, Intermediates, and Products. *J. Phys. Chem. A* **2020**, *124* (4), 711–720. https://doi.org/10.1021/acs.jpca.9b09095.

(20) Galib, M.; Limmer, D. T. Reactive Uptake of N2O5 by Atmospheric Aerosol Is Dominated by Interfacial Processes. *Science* **2021**, *371* (6532), 921–925. https://doi.org/10.1126/science.abd7716.

(21) Gržinić, G.; Bartels-Rausch, T.; Türler, A.; Ammann, M. Efficient Bulk Mass Accommodation and Dissociation of N2O5 in Neutral Aqueous Aerosol. *Atmospheric Chem. Phys.* **2017**, *17* (10), 6493–6502. https://doi.org/10.5194/acp-17-6493-2017.

(22) Staudt, S.; Gord, J. R.; Karimova, N. V.; McDuffie, E. E.; Brown, S. S.; Gerber, R. B.; Nathanson, G. M.; Bertram, T. H. Sulfate and Carboxylate Suppress the Formation of ClNO2 at Atmospheric Interfaces. *ACS Earth Space Chem.* **2019**, *3* (9), 1987–1997. https://doi.org/10.1021/acsearthspacechem.9b00177.

(23) Kregel, S. J.; Derrah, T. F.; Moon, S.; Limmer, D. T.; Nathanson, G. M.; Bertram, T. H. Weak Temperature Dependence of the Relative Rates of Chlorination and Hydrolysis of N_2O_5 in NaCl–Water Solutions. *J. Phys. Chem. A* **2023**, *127* (7), 1675–1685. https://doi.org/10.1021/acs.jpca.2c06543.

(24) Bertram, T. H.; Thornton, J. A. *Toward a General Parameterization of N 2 O 5 Reactivity on Aqueous Particles: The Competing Effects of Particle Liquid Water, Nitrate and Chloride*; 2009; Vol. 9, pp 8351–8363. www.atmos-chem-phys.net/9/8351/2009/.

(25) Burkholder, J. B.; Sander, S. P.; Abbatt, J. P. D.; Barker, J. R.; Cappa, C.; Crounse, J. D.; Dibble, T. S.; Huie, R. E.; Kolb, C. E.; Kurylo, M. J.; Orkin, V. L.; Percival, C. J.; Wilmouth, D. M.; Wine, P. H. *Chemical Kinetics and Photochemical Data for Use in Atmospheric Studies Evaluation Number 19 NASA Panel for Data Evaluation*; 2020.

(26) Morrison, G.; Lakey, P. S. J.; Abbatt, J.; Shiraiwa, M. Indoor Boundary Layer Chemistry Modeling. *Indoor Air* **2019**, *29* (6), 956–967. https://doi.org/10.1111/ina.12601.

(27) Shiraiwa, M.; Pfrang, C.; Poschl, U. Kinetic Multi-Layer Model of Aerosol Surface and Bulk Chemistry (KM-SUB): The Influence of Interfacial Transport and Bulk Diffusion on the Oxidation of Oleic Acid by Ozone. *Atmos Chem Phys* **2010**.

(28) Cruzeiro, V. W. D.; Galib, M.; Limmer, D. T.; Götz, A. W. Uptake of N2O5 by Aqueous Aerosol Unveiled Using Chemically Accurate Many-Body Potentials. *Nat. Commun.* **2022**, *13* (1). https://doi.org/10.1038/s41467-022-28697-8.

(29) Wingen, L. M.; Moskun, A. C.; Johnson, S. N.; Thomas, J. L.; Roeselová, M.; Tobias, D. J.; Kleinman, M. T.; Finlayson-Pitts, B. J. Enhanced Surface Photochemistry in Chloride–Nitrate Ion Mixtures. *Phys. Chem. Chem. Phys.* **2008**, *10* (37), 5668. https://doi.org/10.1039/b806613b.

(30) Thomas, J. L.; Roeselová, M.; Dang, L. X.; Tobias, D. J. Molecular Dynamics Simulations of the Solution−Air Interface of Aqueous Sodium Nitrate. *J. Phys. Chem. A* **2007**, *111* (16), 3091–3098. https://doi.org/10.1021/jp0683972.

(31) Li, J.; Wang, F. Surface Penetration without Enrichment: Simulations Show Ion Surface Propensities Consistent with Both Elevated Surface Tension and Surface Sensitive Spectroscopy. *J. Phys. Chem. B* **2019**, *123* (33), 7197–7203. https://doi.org/10.1021/acs.jpcb.9b04424.

(32) Gaston, C. J.; Thornton, J. A. Reacto-Diffusive Length of N2O5 in Aqueous Sulfate- and Chloride-Containing Aerosol Particles. *J. Phys. Chem. A* **2016**, *120* (7), 1039–1045. https://doi.org/10.1021/acs.jpca.5b11914.

(33) Ryder, O. S.; Campbell, N. R.; Shaloski, M.; Al-Mashat, H.; Nathanson, G. M.; Bertram, T. H. Role of Organics in Regulating ClNO2 Production at the Air-Sea Interface. *J. Phys. Chem. A* **2015**, *119* (31), 8519–8526. https://doi.org/10.1021/jp5129673.

(34) Pegram, L. M.; Record, M. T. Hofmeister Salt Effects on Surface Tension Arise from Partitioning of Anions and Cations between Bulk Water and the Air−Water Interface. *J. Phys. Chem. B* **2007**, *111* (19), 5411–5417. https://doi.org/10.1021/jp070245z.

35) Moon, S.; Limmer, D. T. Enhanced ClNO2 Formation at the Interface of Sea-Salt Aerosol. arXiv March 13, 2024. http://arxiv.org/abs/2403.09052.

4.8 Supporting Information

4.8.1 Kinetic modeling methods

Figure 4.S1 shows a schematic of the kinetic model used in this work. The model includes flows into and out of the three regions of the flow reactor. The boundary layer above the solution and the bulk solution are treated using a multilayer approach. The model parameters and rate equations are described in detail in two previous publications.[1, 2] We assume that the gas phase is well-mixed. Fickian diffusion is assumed to occur in the boundary layer and the solution bulk. Due to short reacto-diffusive lengths, the layers in the bulk close to the surface are significantly thinner so that concentration gradients can be accounted for, and the model has been tested with varying layer numbers to check for convergence. The model includes reversible adsorption to the surface of the solution and reversible partitioning into the solution bulk. Nineteen reactions are included in the solution bulk and at the surface and are listed in Table 4.S1 alongside their rate coefficients. These include the reaction of N_2O_5 with water forming an ionic intermediate ($H_2ONO_2^+/NO_3^-$) which can subsequently react with NO_3^-, H_2O and Cl^- forming a variety of products. The reactions allow for the ^{14}N and ^{15}N isotopes to be tracked in different compounds over time. Additional parameters included in the model are listed in Table 4.S2 and include Henry's law coefficients, bulk and gas-phase diffusion coefficients, initial surface accommodation coefficients, desorption lifetimes, the volumes in the flow reactor, the thickness and surface area of the solution, the volumetric flow

rate, the boundary layer length and the concentration of N_2O_5 in the flow entering the reactor. A set of ordinary differential equations are used to describe the mass balance of each molecule in the gas phase, in the boundary layer as well as for the surface and each bulk layers, which is solved numerically using the Matlab software.

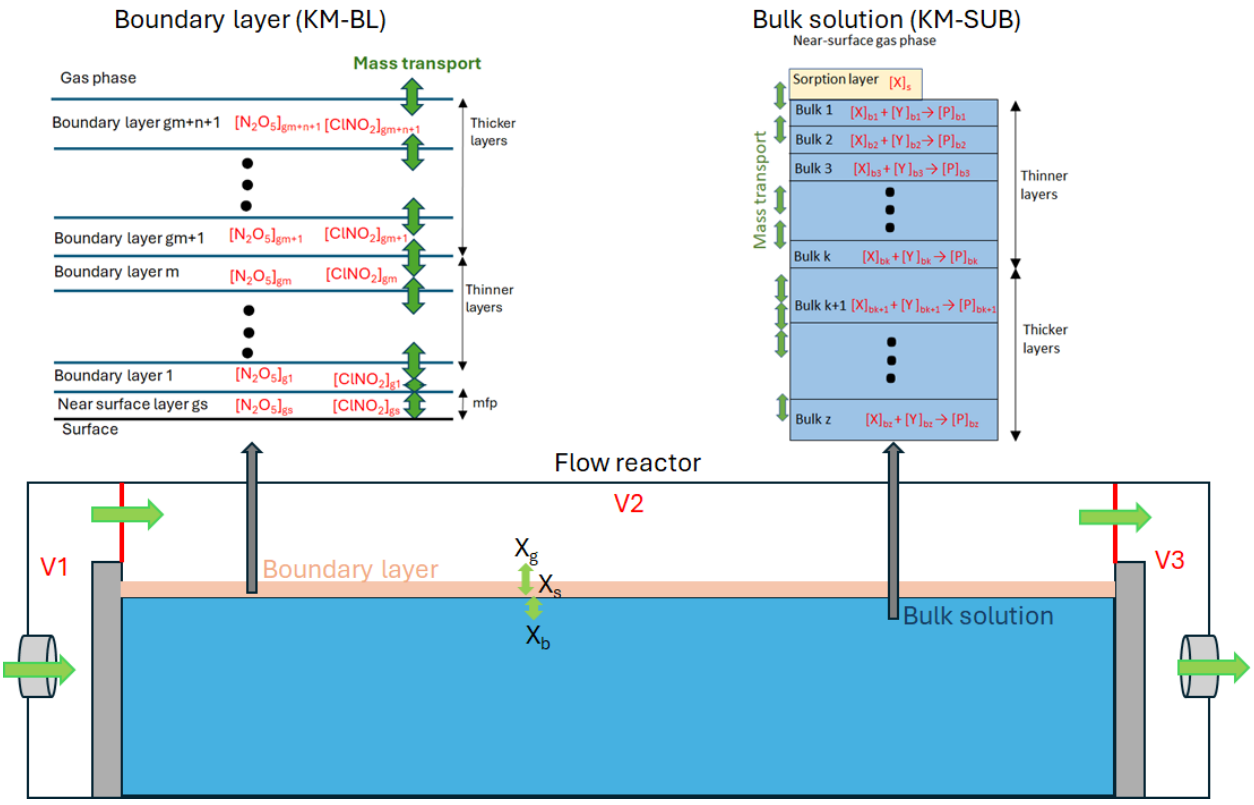

Figure 4-S1 A schematic of the kinetic model used in this work. The model consists of flows through a flow reactor, gas-phase diffusion which is treated using the kinetic multi-layer model of the boundary layer (KM-BL) and surface and bulk mass transport and reactions which are treated using the kinetic multi-layer model of aerosol surface and bulk chemistry (KM-SUB).[1, 2]

Table 4.S1 Reactions and rate coefficients included in the kinetic multi-layer model.

Reaction number	Reaction	Bulk reaction rate coefficient*	Reference or explanation
1	$14,14N_2O_{5(aq)} + H_2O_{(l)} \rightarrow H_2O14NO_2^+/14NO_3^-{}_{(aq)}$	4.0×10^5 s^{-1}	Required to obtain an uptake coefficient of ~0.03. This value is within the error bars of Bertram and Thornton (2009)[3].
2	$14,15N_2O_{5(aq)} + H_2O_{(l)} \rightarrow 0.5(H_2O15NO_2^+/14NO_3^-{}_{(aq)} + H_2O14NO_2^+/15NO_3^-{}_{(aq)})$	4.0×10^5 s^{-1}	
3	$15,15N_2O_{5(aq)} + H_2O_{(l)} \rightarrow H_2O15NO_2^+/15NO_3^-{}_{(aq)}$	4.0×10^5 s^{-1}	
4	$H_2O14NO_2^+/14NO_3^-{}_{(aq)} + 15NO_3^-{}_{(aq)} \rightarrow 14,15N_2O_{5(aq)} + 14NO_3^-{}_{(aq)} + H_2O_{(l)}$	$(1.3 – 2.2) \times 10^8$ M^{-1} s^{-1}	Unknown, determined by fitting to the measurements.
5	$H_2O15NO_2^+/14NO_3^-{}_{(aq)} + 15NO_3^-{}_{(aq)} \rightarrow 15,15N_2O_{5(aq)} + 14NO_3^-{}_{(aq)} + H_2O_{(l)}$	$(1.3 – 2.2) \times 10^8$ M^{-1} s^{-1}	
6	$H_2O14NO_2^+/15NO_3^-{}_{(aq)} + 15NO_3^-{}_{(aq)} \rightarrow 14,15N_2O_{5(aq)} + 15NO_3^-{}_{(aq)} + H_2O_{(l)}$	$(1.3 – 2.2) \times 10^8$ M^{-1} s^{-1}	
7	$H_2O15NO_2^+/15NO_3^-{}_{(aq)} + 15NO_3^-{}_{(aq)} \rightarrow 15,15N_2O_{5(aq)} + 15NO_3^-{}_{(aq)} + H_2O_{(l)}$	$(1.3 – 2.2) \times 10^8$ M^{-1} s^{-1}	
8	$H_2O14NO_2^+/14NO_3^-{}_{(aq)} + H_2O_{(l)} \rightarrow 2H_3O^+_{(aq)} + 2\ 14NO_3^-{}_{(aq)}$	4×10^7 s^{-1}	Chosen as 100 times larger than k(R1-R3) to ensure R1-R3 are the rate-limiting steps in the model.
9	$H_2O14NO_2^+/15NO_3^-{}_{(aq)} + H_2O_{(l)} \rightarrow 2H_3O^+_{(aq)} + 14NO_3^-{}_{(aq)} + 15NO_3^-{}_{(aq)}$	4×10^7 s^{-1}	
10	$H_2O15NO_2^+/14NO_3^-{}_{(aq)} + H_2O_{(l)} \rightarrow 2H_3O^+_{(aq)} + 14NO_3^-{}_{(aq)} + 15NO_3^-{}_{(aq)}$	4×10^7 s^{-1}	
11	$H_2O15NO_2^+/15NO_3^-{}_{(aq)} + H_2O_{(l)} \rightarrow 2H_3O^+_{(aq)} + 2\ 15NO_3^-{}_{(aq)}$	4×10^7 s^{-1}	
12	$H_2O14NO_2^+/14NO_3^-{}_{(aq)} + Cl^-_{(aq)} \rightarrow Cl14NO_{2(aq)} + 14NO3\text{-}(aq) + H_2O_{(l)}$	8×10^8 M^{-1} s^{-1}	Determined from k_{Cl^-}/k_{water} from Kregel et al (2023)[5]
13	$H_2O15NO_2^+/14NO_3^-{}_{(aq)} + Cl^-_{(aq)} \rightarrow Cl15NO_{2(aq)} + 14NO3\text{-}(aq) + H_2O_{(l)}$	8×10^8 M^{-1} s^{-1}	
14	$H_2O14NO_2^+/15NO_3^-{}_{(aq)} + Cl^-_{(aq)} \rightarrow Cl14NO_{2(aq)} + 15NO_3^-{}_{(aq)} + H_2O_{(l)}$	8×10^8 M^{-1} s^{-1}	
15	$H_2O15NO_2^+/15NO_3^-{}_{(aq)} + Cl^-_{(aq)} \rightarrow Cl15NO_{2(aq)} + 15NO_3^-{}_{(aq)} + H_2O_{(l)}$	8×10^8 M^{-1} s^{-1}	
16	$H_2O14NO_2^+/14NO_3^-{}_{(aq)} + 14NO_3^-{}_{(aq)} \rightarrow 14,14N_2O_{5(aq)} + 14NO_3^-{}_{(aq)} + H_2O_{(l)}$	$(1.3 – 2.2) \times 10^8$ M^{-1} s^{-1}	Assumed to be the same as for reactions 4 – 7.
17	$H_2O15NO_2^+/14NO_3^-{}_{(aq)} + 14NO_3^-{}_{(aq)} \rightarrow 14,15N_2O_{5(aq)} + 14NO_3^-{}_{(aq)} + H_2O_{(l)}$	$(1.3 – 2.2) \times 10^8$ M^{-1} s^{-1}	
18	$H_2O14NO_2^+/15NO_3^-{}_{(aq)} + 14NO_3^-{}_{(aq)} \rightarrow 14,14N_2O_{5(aq)} + 15NO_3^-{}_{(aq)} + H_2O_{(l)}$	$(1.3 – 2.2) \times 10^8$ M^{-1} s^{-1}	
19	$H_2O15NO_2^+/15NO_3^-{}_{(aq)} + 14NO_3^-{}_{(aq)}$ --> $14,15N_2O_{5(aq)} + 15NO_3^-{}_{(aq)} + H_2O_{(l)}$	$(1.3 – 2.2) \times 10^8$ M^{-1} s^{-1}	

*Surface reaction rate coefficients for adsorbed molecules were in units of cm^2 s^{-1} or s^{-1}. Rate coefficients at the surface were assumed to occur at the same rate and were estimated by dividing the value in cm^3 s^{-1} by the diameter of 1 molecule of $H_2O14NO_2^+/14NO_3^-$.

Table 4.S2 Parameters included in the kinetic multi-layer model.

Parameter	**Description**	**Value**	**Reference or explanation**
H_{N2O5}	Henry's law coefficient of N_2O_5	3.0 M atm^{-1}	Cruzeiro et al. (2022)[4]
H_{ClNO2}	Henry's law coefficient of $ClNO_2$	0.024 M atm^{-1}	Behnke et al. (1997)[6]
$D_{g,N2O5}$	Gas-phase diffusion coefficient of N_2O_5	0.11 cm^2 s^{-1}	Tang et al. (2014)[7]
D_{gClNO2}	Gas-phase diffusion coefficient of $ClNO_2$	0.12 cm^2 s^{-1}	Tang et al. (2014)[7]
$D_{b,N2O5}$	Bulk diffusion coefficient of N_2O_5	1.89×10^{-5} cm^2 s^{-1}	Cruzeiro et al. (2022)[4]
$D_{b,ClNO2}$	Bulk diffusion coefficient of $ClNO_2$	1.90×10^{-5} cm^2 s^{-1}	Estimated from the value for N_2O_5
$D_{b,NO3-}$	Bulk diffusion coefficient of NO_3^-	1.8×10^{-5} cm^2 s^{-1}	Estimated using the EPA online diffusion coefficient calculator (Note that small changes in these values do not impact the results)
$D_{b,Cl-}$	Bulk diffusion coefficient of Cl^-	2.3×10^{-5} cm^2 s^{-1}	
$D_{b,\ H2ONO2+/NO3-}$	Bulk diffusion coefficient of $H_2ONO_2^+/NO_3^-$	1×10^{-5} cm^2 s^{-1}	
$\alpha_{s,0,all}$	Initial surface accommodation coefficient of N_2O_5 and $ClNO_2$	0.96	Cruzeiro et al. (2022)[4]. Assumed to be the same for $ClNO_2$
$\tau_{d,all}$	Desorption lifetime of N_2O_5 and $ClNO_2$	1 ns	Estimated value
V_1 and V_3	Volume 1 and Volume 3 as depicted in Figure S1	0.97 cm^3	Experimental value
V_2	Volume 2 as depicted in Figure S1	11.34 cm^3	Experimental value (includes the boundary layer)
δ_{sol}	Total thickness of the solution	1.38 cm	Experimental value
A_{sol}	Total surface area of the solution	14.5 cm^2	Experimental value
φ	Volumetric flow rate	25 cm^3 s^{-1}	Experimental value
δ_{BL}	Total thickness of the boundary layer	0.1 cm	Determined by the approximate decrease in N_2O_5 exiting the reactor.
$[N_2O_5]_{g,in}$	Concentration of N_2O_5 in the flow entering the reactor	20 ppb	Experimental value

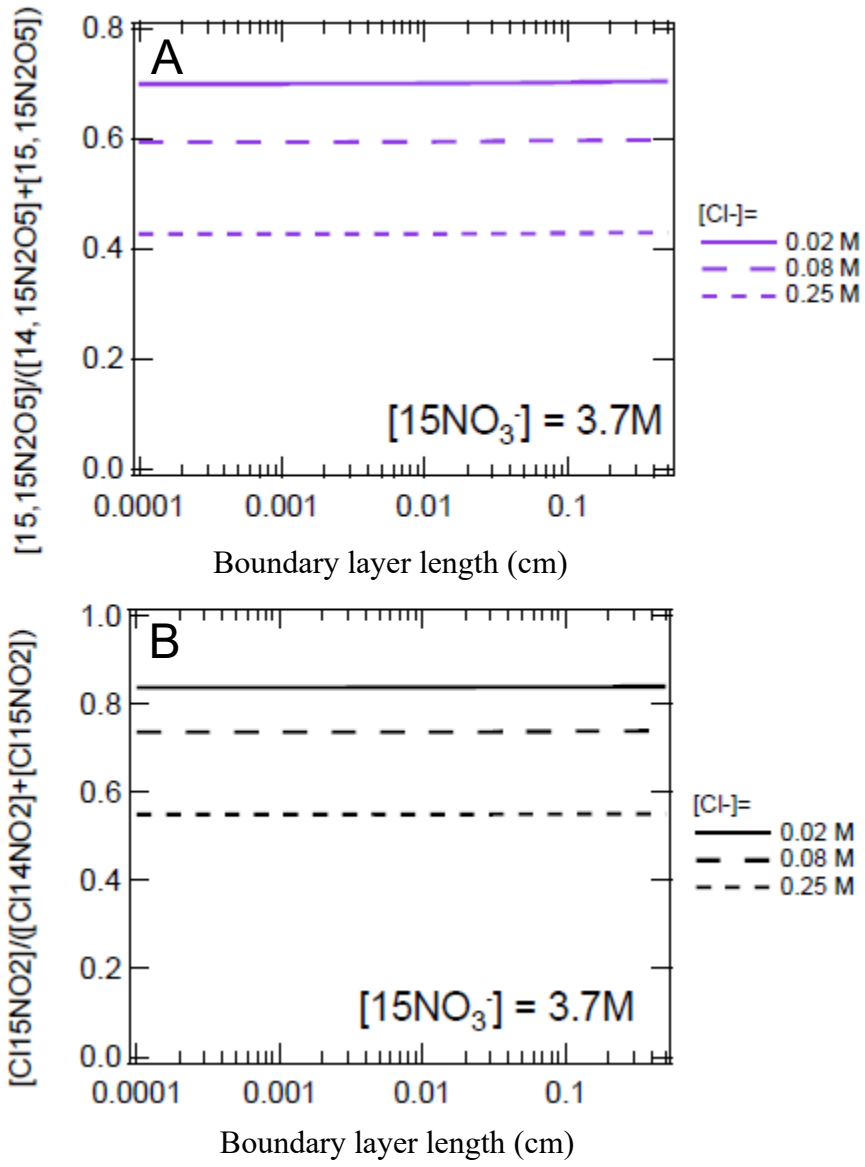

Figure 4-S2 Plots of the fraction of labeled N_2O_5 that is $^{15,15}N_2O_5$ (A) and the heavy $Cl^{15}NO_2$ fraction (B) as we varied the boundary layer length. Model results were collected at 0.02, 0.08, and 0.25 M Cl^- with 3.7 M $^{15}NO_3^-$

Figure 4.S2 shows the effect of the boundary layer thickness on the relative production of isotopically labeled species. Panel A shows the fraction of labeled N_2O_5 that is doubley-labeled $^{15,15}N_2O_5$. The fraction of $^{15,15}N_2O_5$ is constant across the range in boundary layer thicknesses tested. Panel B shows the same trend for the $Cl^{15}NO_2$ fraction, constant over the boundary layer

thicknesses. This indicates that the depth of the boundary layer does not impact the relative reaction rates.

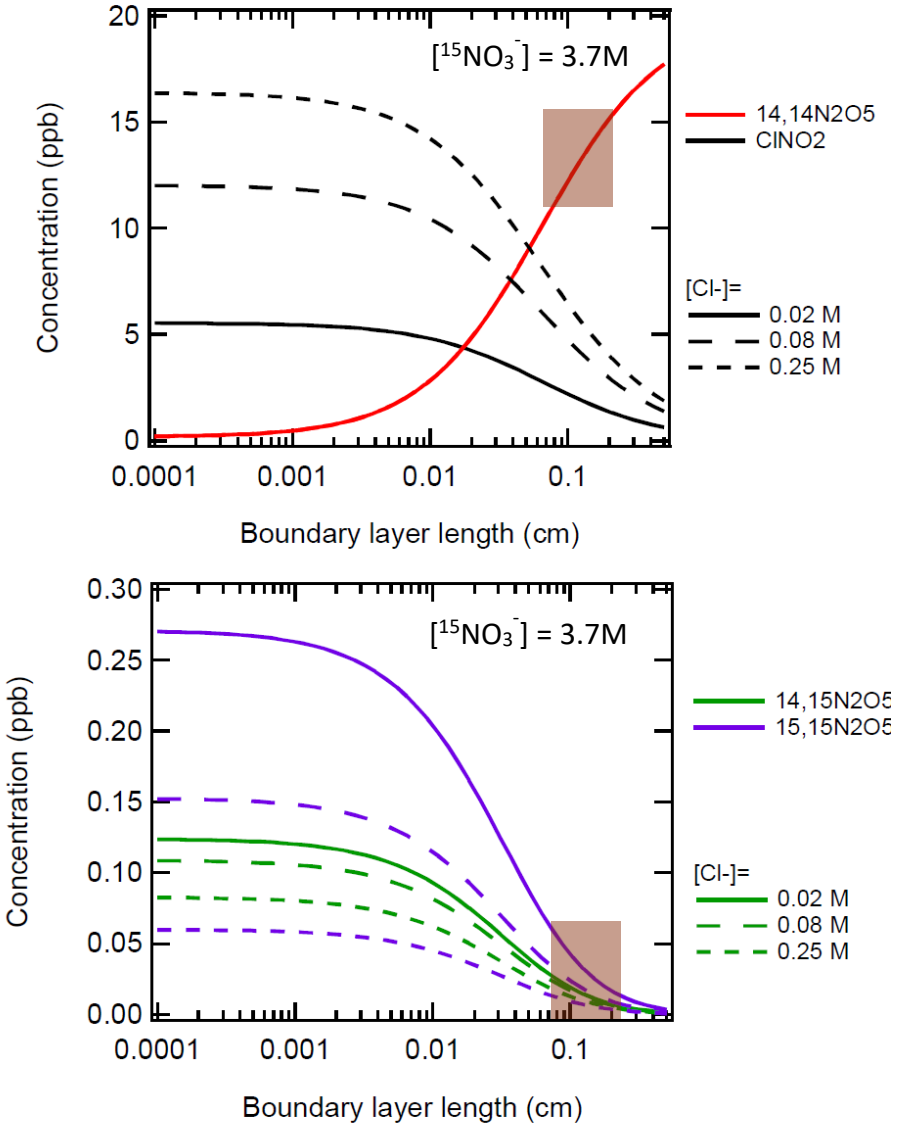

Figure 4-S3. Plots of the concentrations (in ppb) of $^{14,14}N_2O_5$ and total $ClNO_2$ (top) and $^{14,15}N_2O_5$ and $^{15,15}N_2O_5$ (bottom) species determined from the model as the boundary layer length was varied. The concentrations of gaseous species are given at 3 different Cl^- concentrations. Initial $^{14,14}N_2O_5$ concentration was 20 ppb. The transparent orange box indicates the expected boundary layer regime the experiment was conducted in based on experiments measuring a 20-40% decrease in N_2O_5.

Figure 4-S3 shows the model results for the concentrations of $^{14,14}N_2O_5$, total $ClNO_2$, $^{14,15}N_2O_5$, and $^{15,15}N_2O_5$ as the size of the boundary layer was varied. Previous experiments predicted a N_2O_5 loss of 20 - 40% to solution (orange box in top panel of Figure 4-S3). Using this and the model results in Figure 4-S3, we predict the boundary layer thickness in the dual channel flow reactor to be about 0.1 cm, potentially ranging from 0.06 – 0.3 cm. At this thickness, the model predicts a low concentration of $^{14,15}N_2O_5$ and $^{15,15}N_2O_5$ in the gas phase, in the tens of parts per trillion concentrations. Further, the model predicts a significantly lower concentration of $^{14,15}N_2O_5$ and $^{15,15}N_2O_5$ relative to the amount of N_2O_5 lost or $ClNO_2$ produced by a factor of 100.

4.8.2 References

1. Morrison, G.; Lakey, P. S.; Abbatt, J.; Shiraiwa, M., Indoor boundary layer chemistry modeling. *Indoor Air* **2019,** *29* (6), 956-967.

2. Shiraiwa, M.; Pfrang, C.; Pöschl, U., Kinetic multi-layer model of aerosol surface and bulk chemistry (KM-SUB): the influence of interfacial transport and bulk diffusion on the oxidation of oleic acid by ozone. *Atmos. Chem. Phys.* **2010,** *10* (8), 3673-3691.

3. Bertram, T.; Thornton, J., Toward a general parameterization of N_2O_5 reactivity on aqueous particles: the competing effects of particle liquid water, nitrate and chloride. *Atmos. Chem. Phys.* **2009,** *9* (21), 8351-8363.

4. Cruzeiro, V. W. D.; Galib, M.; Limmer, D. T.; Götz, A. W., Uptake of N_2O_5 by aqueous aerosol unveiled using chemically accurate many-body potentials. *Nat. Commun.* **2022,** *13* (1), 1266.

5. Kregel, S. J.; Derrah, T. F.; Moon, S.; Limmer, D. T.; Nathanson, G. M.; Bertram, T. H., Weak Temperature Dependence of the Relative Rates of Chlorination and Hydrolysis of N2O5 in NaCl–Water Solutions. *J. Phys. Chem. A* **2023,** *127* (7), 1675-1685.

6. Behnke, W.; George, C.; Scheer, V.; Zetzsch, C., Production and decay of ClNO2 from the reaction of gaseous N2O5 with NaCl solution: Bulk and aerosol experiments. *J. Geophys. Res. - Atmos.* **1997,** *102* (D3), 3795-3804.

7. Tang, M.; Cox, R.; Kalberer, M., Compilation and evaluation of gas phase diffusion coefficients of reactive trace gases in the atmosphere: volume 1. Inorganic compounds. *Atmos. Chem. Phys.* **2014,** *14* (17), 9233-9247.